Title: Exhumation of the Coyote Mountains metamorphic core complex (Arizona): implications for orogenic collapse of the southern North American Cordillera.

Authors: Raphaël Gottardi (a), Ryan McAleer (b), Gabriele Casale (c), Megan Borel (a,d), Alexander Iriondo (e,f), Gilby Jepson (f)

(a) University of Louisiana at Lafayette, School of Geosciences, Hamilton Hall, 611 McKinley Street, Lafayette, LA 70504

(b) U.S. Geological Survey, Florence Bascom Geoscience Center, 12201 Sunrise Valley Dr, Reston, VA 20192

(c) Appalachian State University, Department of Geological and Environmental Sciences, 033 Rankin Science West, ASU Box 32067, Boone, NC 28608-2067

(d) University of Florida, Department of Geological Sciences, 241 Williamson Hall, 1843 Stadium Road, Gainesville, FL 32611

(e) Universidad Nacional Autónoma de México, Centro de Geociencias, Blvd. Juriquilla No. 3001, Querétaro, Querétaro 76230, México

(f) Department of Geosciences, University of Arizona, Tucson, Arizona 85721

Corresponding Author: Raphaël Gottardi

Email: gottardi@louisiana.edu

Office phone: 337-482-6177

Cell phone: 651-329-6059

Fax: 337-482-5395

ABSTRACT

A microstructural and thermochronometric analysis of the Coyote Mountains detachment shear zone provides new insight into the collapse of the southern North American Cordillera. The Coyote Mountains is a metamorphic core complex that makes up the northern end of the Baboquivari Mountains in southern Arizona. The Baboquivari Mountains records several episodes of crustal shortening and thickening, and regional metamorphism, including the Late Cretaceous-early Paleogene Laramide orogeny which is locally expressed by the Baboquivari thrust fault. Thrusting and shortening were accompanied by magmatic activity recorded by intrusion of Paleocene muscovite-biotite-garnet peraluminous granites such as the ~58 Ma Pan Tak Granite, interpreted as anatectic melts representing the culmination of the Laramide orogeny. Following Laramide crustal shortening, the northern end of the Baboquivari Mountains was exhumed along a top-to-the-north detachment shear zone, which resulted in the formation of the Coyote Mountains metamorphic core complex. Structural and microstructural analysis show that the detachment shear zone evolved under a strong component of non-coaxial (simple shear) deformation, at deformation conditions of ~450 ± 50°C, under a differential stress of ~60 MPa, and a strain rate of 1.5×10^{-11} s^{-1} to 5.0×10^{-13} s^{-1} at depth of ~11–14 km. Detailed $^{40}Ar/^{39}Ar$ geochronology of biotite and muscovite, in the context of the deformation conditions determined by quartz microstructures, suggests that the mylonitization associated with the formation of the Coyote Mountains metamorphic core complex started at ~29 Ma (early Oligocene). Apatite fission track ages indicate that the footwall of the Coyote Mountains metamorphic core complex experienced rapid exhumation to the upper crust by ~24 Ma. The fact that mylonitization and rapid extensional exhumation post-dates Laramide thickening by ~30 Myr indicates that crustal thickness alone was insufficient to initiate extensional tectonic and required an additional driving force. The timing of mylonitization and rapid exhumation documented here and in other MCCs are consistent with the hypothesis that slab rollback and the effect of a slab window trailing the Mendocino Triple Junction have been critical in driving the development of the MCCs of the southwest.

Our results are consistent with models for orogenic collapse following previous crustal thickening and anatexis.

Keywords

Metamorphic core complex, geochronology and thermochronology, microstructural analysis, orogenic collapse, exhumation, Arizona

1. INTRODUCTION

The prevalence and distribution of metamorphic core complexes (MCCs) in mountain belts suggests that they are fundamental tectonic features critical for the redistribution of mass during orogenic collapse following crustal thickening (e.g., Coney and Harms, 1984; Lister and Davis, 1989; Rey et al., 2001; Whitney et al., 2013). Additionally, MCCs commonly exhume extensive zones of footwall fault rocks. These rocks provide an opportunity to study variations in deformation mechanisms across strain and temperature gradients and commonly across the brittle-ductile transition in quartzofeldspathic rocks. (e.g., Platt et al., 2015). Triggering mechanisms for post-orogenic collapse, as well as strain localization and inception of mylonitization and subsequent exhumation requires further examination.

MCCs form a discontinuous belt from British Columbia to Mexico (Figure 1; Coney, 1974, 1980; Crittenden et al., 1980; Armstrong, 1982; Coney and Harms, 1984; Lister and Davis, 1989). Based on differences in shallow to deep crust interaction, as well as thermogeochronological datasets, Cordilleran MCCs can be divided into three groups: (1) circa Eocene northern MCCs, (2) Eocene, Oligocene, and Miocene central MCCs, (3) and Oligocene to Miocene southern MCCs associated with possible Laramide extension (Figure 1; Whitney et al., 2013). One of the differences between northern and southern MCCs is the magnitude of Cenozoic exhumation, which is more significant in the northern MCCs (tens of km) than in the south (e.g., Whitney et al., 2013). One explanation for this difference comes from the nature of the lithosphere: unlike the northern MCCs, southern MCCs are formed entirely within the cratonic North-America (Coney, 1980; Sloss, 1988). The core of most of the southern MCC exposes Proterozoic igneous rocks, metaluminous granitoids interpreted as Laramide magmatism (continental arc), or Late Cretaceous to early Paleogene peraluminous granitoids, which have been interpreted as the result of Laramide anatexis (Haxel et al., 1984; Dickinson, 1989, 1991; Sylvester, 1998). This magmatism predates MCC formation and is not the product of partial melting of the lower crust during extension, although syn- and post-tectonic intrusions exist in many southern MCCs. Protracted magmatism associated with partial melting, plutonism, and the release of volatiles has been demonstrated to cause significant weakening of the crust, which may trigger strain localization and orogenic collapse (Gans et al., 1989; Armstrong and

Ward, 1991; Lister and Baldwin, 1993; Spencer et al., 1995; Foster et al., 2001; Teyssier and Whitney, 2002; Whitney et al., 2013). While little is known about the precise age and origin of the intrusive rocks composing the cores of many of the southern MCCs, some of these intrusions are extensive and are likely to have deep roots (e.g., Anderson et al., 1988), which may have played an important role in localizing strain. In southern Arizona, these Late Cretaceous and early Paleogene plutons are widespread and well exposed in the core of MCCs, presenting an opportunity to investigate this relationship between magmatism and extension. They provide a window to study lower crustal processes that control the geodynamic evolution of the North American lithosphere following the Laramide crustal thickening, especially in an area where Laramide structures have been overprinted.

The plutonic rocks exposed in the Coyote Mountains MCC consist of Late Cretaceous and early Paleogene plutonic leucocratic, hornblende-free, garnet-two-mica granites, with a distinctly younger tectonic overprint recording middle Paleogene extensional tectonics (Haxel et al., 1980a,b; Wright and Haxel, 1982; Haxel et al., 1984; Goodwin and Haxel, 1990) (Figures 1 and 2). The goal of this study is to resolve the timing of uplift and exhumation, and deformation style of the detachment shear zone associated with the formation of the Coyote Mountains MCC using microstructural kinematic relationships, new U/Pb geochronology and $^{40}Ar/^{39}Ar$ and apatite fission track thermochronology. Our analysis confirms a Late Cretaceous age for the plutonic Pan Tak Granite in the footwall of the Coyote Mountains detachment shear zone, and demonstrates that the footwall cooled rapidly from greenschist facies to less than ~120ºC in the Oligocene. We interpret these results as evidence for Late Cretaceous thrusting, thickening, and plutonic activity that was followed ~30 Ma later by extension associated with post-orogenic collapse responsible for the formation of the Coyote Mountains MCC and associated detachment shear zone. Our findings have important implications regarding the tectonic evolution of the southwestern US and more generally for the variables that may affect the timing and localities of orogenic collapse

2. REGIONAL GEOLOGY

2.1. Metamorphic Core Complexes

The southern belt of MCCs that extends from southeastern California to the Sonoran Desert of Mexico (Figures 1 & 2) is composed of rocks that range in age from Proterozoic to Miocene (e.g., Keith et al., 1980; Haxel et al., 1980a,b; Wright and Haxel, 1982; Haxel et al., 1984; Reynolds, 1985; Anderson et al., 1988; Richard et al., 1990; Bryant and Wooden, 2008; Singleton and Mosher, 2012; Spencer et al., 2019). The onset of early Miocene mylonitization associated with detachment shear zones in the "Colorado River extensional corridor" (CREC) is well determined by thermochronometric studies of synkinematic minerals, and is coeval across multiple MCCs (see Figure 2): ~24 – 22 Ma Sacramento-Chemehuevi (Foster et al., 1990), ~20 – 18 Ma in the Whipple (Hacker et al., 1992 and references therein), ~24 – 21 Ma in the Buckskin-Harcuvar (Scott et al., 1998; Singleton and Wong, 2016), ~22 – 20 Ma in the Harquahala (Richard et al., 1990) Mountains. Similar mylonitization ages recording exhumation are reported in the South Mountains (21–20 Ma, Fitzgerald et al., 1993), and Picacho Mountains (22 – 18 Ma, Gottardi et al., 2018) (Figure 2). In contrast, the onset of detachment faulting in both the Catalina-Rincon and Pinaleño MCCs in southeastern Arizona occurred earlier, and the cooling history is more protracted (29.5 – 23.5 Ma, Davy et al., 1989; Fayon et al., 2000; and 32.8 – 18.5 Ma, Long et al., 1995, respectively) (Figure 2). Geochronological datasets in MCCs located in Mexico report ages for the onset of mylonitization ranging from 35 to 21 Ma, intermediate to overlapping with the times of onset recorded in the CREC and SE Arizona (Wong and Gans, 2008, Wong et al. 2010). However, regardless of the time of onset and locality, nearly all studies demonstrate that detachment systems record rapid cooling, i.e. major slip, in the early Miocene (primarily ~25 – 16 Ma) (Figure 2).

The record of deep-seated late Mesozoic and early Paleogene compression and metamorphism, and subsequent middle-Paleogene extensional deformation is well exposed in the Papago terrane (Haxel et al., 1980a,b), situated along the United States – Mexico border near Tucson, AZ (Figure 3). The Papago terrane is characterized by Jurassic volcanic and granitoid rocks that are juxtaposed across synmetamorphic thrust faults and/or intruded by synmetamorphic to postmetamorphic garnet-two-mica peraluminous granites (Figure 3, Haxel et al., 1980a, b, 1984; Goodwin and Haxel, 1990). Geochronological data indicates that metamorphism, thrust-faulting, and plutonism were closely related to the Late Cretaceous to early Paleogene Laramide orogeny (e.g. Haxel et al., 1984) (Figure 3). Most of the Papago terrane was subsequently affected by middle to late Paleogene extension associated with the formation of MCCs, although the precise timing and tectonic affinity of this latter deformation event is poorly constrained.

2.2. Coyote Mountains

The Coyote Mountains MCC (Davis et al., 1987) makes up the northern end of the 80 km long Baboquivari Mountains, located in the western part of the southern Papago terrane (Figure 3, Haxel et al., 1980a, b, 1984). The Baboquivari Mountains are composed of Early Jurassic sedimentary, volcanic, and plutonic rocks as well as minor Middle Jurassic diorite. These rocks were metamorphosed in the Late Cretaceous to early Paleogene and metamorphism was coeval with the intrusion of Late Cretaceous to early Paleogene muscovite-biotite-garnet peraluminous granite and associated pegmatite (Figure 3; Haxel et al., 1980a,b, 1984; Wright et al., 1981; Wright and Haxel, 1982). The Baboquivari Mountains experienced crustal shortening and thickening and regional metamorphism during the Late Cretaceous Laramide orogeny (Haxel et al., 1980a,b; Wright and Haxel, 1982; Haxel et al., 1984; Goodwin and Haxel, 1990). In southern Arizona and northern Mexico the Laramide orogeny is characterized by high-angle reverse faults, some of which have reactivated Late Jurassic-Early Cretaceous rift structures (Davis, 1980; Krantz et al., 1989; Fitz-Díaz et al., 2018). In the Baboquivari Mountains, erosion has exposed a major regional thrust fault, the Baboquivari thrust fault (Figure 3), which is accompanied by isoclinal folding and regional metamorphism (Wright and Haxel, 1982; Haxel and Wright, 1984) in contrast to the higher angle contractional structures observed elsewhere. The Baboquivari fault thrusts Cretaceous sedimentary and Middle to Late Jurassic volcanic and plutonic rocks, over Early Jurassic granitoids and metamorphic rocks (Haxel and Wright, 1984). The fabric associated with this Late Cretaceous deformation is characterized by a north-south striking foliation and a lineation plunging gently to the southwest. This fabric is associated with kink, crenulation, and isoclinal folds with fold axes that strike west-northwest (Wright and Haxel, 1982; Haxel and Wright, 1984). Altogether, these fabric elements suggest an east-northeast transport direction. Peak metamorphism is interpreted to be contemporaneous with thrusting along the Baboquivari (Wright and Haxel, 1982; Haxel and Wright, 1984). Following deformation these metamorphic rocks were intruded by muscovite-biotite-garnet peraluminous granites and associated pegmatite, such as the ~58 Ma Pan Tak Granite (Figure 3), which have been interpreted as anatectic melts representing the culmination of the Laramide orogeny (Wright and Haxel, 1982; Haxel and Wright, 1984; Goodwin and Haxel, 1990).

Exhumation of the Baboquivari Mountains throughout the Paleogene led to the exposure of the footwall rocks of the Baboquivari thrust. In this study area tectonic exhumation was accommodated by the Coyote Mountains detachment shear zone to the north (Figure 3), resulting in the formation of the Coyote Mountains MCC. A second detachment fault along the southern margin of the Baboquivari Mountains, the Pozo Verde Mountains detachment—is outside the field area, but likely also accommodated exhumation (Davis, 1980; Goodwin and Haxel, 1990).

The footwall of the Coyote Mountains detachment shear zone is principally composed of Late Cretaceous/early Paleogene Pan Tak Granite and pegmatite, which are injected lit-par-lit into the Cambrian Bolsa Quartzite, Cambrian to Devonian Abrigo and Martin Formations, and Jurassic diorite. Quartzite mylonite is locally interlayered with mylonitized pegmatite sills; such pendants are particularly abundant in the eastern part of the detachment shear zone (Gardulski, 1980; Davis et al., 1987). The mylonitic fabric of the Coyote Mountains detachment shear zone is characterized by a gently north-dipping foliation and north plunging lineation, and top-to-the-north kinematic shear sense indicators are common (Figure 3) (Goodwin and Haxel, 1990; Davis et al., 1987). The Ajo road décollement separates the footwall mylonites from the hanging wall which is composed of unmetamorphosed sedimentary and volcanic rocks of the Cretaceous Roadside and Sand Wells Formations (Gradulski, 1980; Davis et al., 1987). Kinematic analysis indicates that brittle deformation along the Ajo Road décollement was achieved by normal faulting in a direction similar to the lineation in footwall mylonite (Gardulski, 1980; Davis et al., 1987). Along the décollement, footwall rocks are intensively brecciated and shattered and displacement on the décollement imparted a brittle foliation that locally over prints the mylonitic foliation (Gardulski, 1980). These field relationships suggest that the development of the mylonitic foliation was completed before displacement on the Ajo Road décollement.

Scattered lamprophyric dikes, generally near vertical and trending north-south, intrude the Pan Tak Granite throughout the Coyote Mountains, and crosscut the mylonitic foliation (Gardulski, 1980; Haxel and others, 1980b; Haxel and Wright, 1982). Haxel and Wright (1982) infer a minimum age for the lamprophyric dikes in the Coyote Mountains of 24 Ma.

3. MICROSTRUCTURAL ANALYSIS

Modal assemblages for the Pan Tak Granite range from 33–26% alkali feldspar, 31–24% plagioclase feldspar, 34–27% quartz, 8–18% mica (muscovite and biotite) with trace amounts of garnet, magnetite, apatite, chlorite, zircon and titanite. The youngest phase of the Pan Tak Granite is an equigranular, coarse-grained peraluminous leucocratic monzogranite, which is generally typical of melts derived by partial melting of the crystalline basement (e.g., Clarke, 1981; Sylvester, 1998; Turpin et al., 1990; Barbarin, 1996). Multi-grain U/Pb TIMS analysis of multiple aliquots of zircon from the Pan Tak Granite yielded a lower intercept age of 58 ± 2 Ma consistent with emplacement during the Laramide orogeny (Wright and Haxel, 1982).

The Pan Tak Granite consists of a granitic and pegmatitic phase, both of which are overprinted by a mylonitic fabric, forming both a granite and a pegmatite mylonite. The fabric ranges from protomylonitic, weakly foliated, with limited recrystallization, and few porphyroclasts (Figure 4A), to mylonitic, strongly foliated, with extensive recrystallization (up to 90% grain size reduction) and a strong preferred grain orientation (Figure 4B, C, D). The mylonites with the strongest fabric are also generally characterized by a higher modal content of muscovite (Figure 4D) perhaps suggesting strain partitioning into locally more micaceous granite or new growth (neoformation).

3.1. Quartz microstructures and deformation mechanisms

In the mylonites quartz occurs either as elongated, stretched ribbons, or forms domains of finely recrystallized grains, mixed with recrystallized feldspar (Figures 4 and 5). Quartz domains show grains with straight boundaries and of uniform sizes (~20 – 50 μm), characteristic of recrystallization by subgrain rotation (Figure 5A-B, regime II of dislocation creep, Hirth and Tullis, 1992). In these bands, the long axis of recrystallized quartz grains typically form an oblique secondary foliation inclined ~15–30° to the mylonitic shear plane, consistent with a top-to-the-north shear sense. Large quartz ribbons exhibit both small subgrains (Figure 5C) and larger grains with serrated boundaries (Figure 5D), suggesting recrystallization by both subgrain rotation and limited grain boundary migration, respectively (regime II & III of dislocation creep of Hirth and Tullis, 1992). In the protomylonite and mylonitized pegmatite, quartz grains have serrated grain boundaries and variable sizes, consistent with recrystallization by grain boundary migration (Figure 5D, regime III of dislocation creep, Hirth and Tullis, 1992). These relatively low strain microstructures are only found in the samples collected farthest from the detachment shear zone.

Quartz ribbons (up to 4 mm in length) are present in all the mylonite samples. The elongate quartz ribbons impart a strong foliation to the mylonite (Figure 4D for example). Stretched and deformed ribbons are commonly wrapped around rigid feldspar porphyroclasts (Figure 5A, B). Larger quartz grains and ribbons display undulose extinction (Figure 5E) as well as intracrystalline dislocation glide quartz microstructures, such as deformation lamellae, patchy extinction, and chessboard textures, indicating that quartz deformed under high flow stress conditions (Hirth and Tullis, 1992).

Evidence for pressure solution in quartz is also infrequently observed in Pan Tak Granite samples as dissolution creep along the edges of large quartz grains forming digitated margins. Finally, fluid inclusion bands, oriented at 15° to 40° to the foliation plane are present in quartz grains and these bands are commonly continuous across several grains (Figure 5F).

For mylonites that have undergone recrystallization at average strain rates typical of most shear zones (10^{-14} to 10^{-12} s^{-1}), the different regimes of dynamic recrystallization of quartz have been correlated to temperatures of deformation by Stipp et al. (2002a, 2002b). Bulging recrystallization is dominant from ~280 to 400°C; subgrain rotation recrystallization takes over between 400 and 500°C, and the transition to grain boundary migration occurs at ~500°C and above. The microstructures of the Pan Tak Granite mylonite show that quartz recrystallized dominantly by subgrain rotation suggesting that the quartz deformation temperature was ≤ 500°C.

3.2. Feldspar microstructures and deformation mechanisms

Much of the alkali feldspar grains in the Pan Tak Granite samples have been deformed, fractured with associated rotation, and mildly altered (Figure 6A, B, E). Alkali feldspar often form augen-porphyroclasts, and record top-to-the-north kinematic shear sense (Figure 4, 6B). Alkali feldspar grains commonly exhibit shear fractures (Figure 6A) or extension fractures along cleavage planes at high angle to foliation (Fig. 6B). Alkali feldspar porphyroclasts are also locally embayed by myrmekite (Fig. 6G) that most commonly occurs along margins oriented perpendicular to the maximum shortening direction. This arrangement of myrmekite is consistent with a deformation-induced origin, and typical for upper greenschist- to lower amphibolite-facies deformation conditions (Simpson and Wintsch, 1989; Pryer, 1993; Ceccato et al., 2018). Flame perthite is also present in the mylonite, and appears as sublinear (wavy), bifurcated features (Fig. 6C, D). Flame perthite, is oriented subparallel with the mylonitic foliation, suggesting it is deformation-induced and formed under locally concentrated high differential stress (Vernon, 1999). About 20% of all alkali feldspar has undergone sericitic alteration, most commonly present within the cores of the alkali feldspar porphyroclasts.

Plagioclase typically forms tabular, subhedral laths (~150–1000 μm), and displays polysynthetic (albite) twinning (Figure 6A, D), and patchy zoning microstructures. Locally plagioclase laths also show bent twinning (Figure 6E) and extension and shear microfractures (Figure 6A, B).

Recrystallization of feldspar is apparent, particularly along the margins of quartz ribbons in the mylonite. Feldspars also display undulatory extinction, indicating dislocation glide with no recovery (Vernon, 1999; Passchier and Trouw, 2005).

In naturally deformed rocks, at low metamorphic grade (< 400ºC), feldspar deforms mainly by brittle fracturing and cataclastic flow, while at low to medium metamorphic grade (400-500ºC), internal microfracturing is assisted by minor dislocation glide (Passchier and Trouw, 2005). At medium grade temperatures (450-550ºC), dislocation climb becomes possible in feldspars and recrystallization by bulging and subgrain rotation becomes important (Fitz Gerald and Stünitz, 1993, Pryer, 1993; Stünitz and Fitz Gerald, 1993; Passchier and Trouw, 2005). The microstructures observed in the Pan Tak Granite mylonite indicate that feldspar predominantly deformed by fracture with subordinate subgrain rotation recrystallization (Figure 6H), recording deformation temperatures between ~400 and 500°C, and consistent with the deformation textures observed in quartz.

3.3. Mica Microstructures

Micas form a moderate modal constituent of the Pan Tak Granite. Minor chlorite is present as alteration of biotite along biotite grain boundaries, sericitization of feldspar contributes to the modal abundance of muscovite, and locally in some high strain samples fine micas form contiguous folia. However, coarse-grained muscovite and biotite constitute the majority of the modal mica content (4 to 18%, and up to 4%, respectively). The presence of coarse muscovite and biotite in the undeformed Pan Tak Granite suggest these micas are igneous in origin (Wright and Haxel, 1982).

Evidence for deformation of these coarse-grained micas, as well as neocrystallization of fine-grained mica, is limited in the protomylonite samples. In these samples muscovite and biotite remain relatively euhedral (tabular shape) forming rhomb-shaped grains (Figure 7A-C). Bird's eye extinction is visible in micas in most samples where grains are large and deformed. Biotite grains exhibit minor chloritization along grain rims. Neocrystallized fine-grained muscovite occurs as local sericitization of feldspars (Figure 5B, 6B, 7A), in microfractures in quartz and feldspar (Figure 6B), and locally along grain boundaries (Figure 6C).

In the mylonite samples, evidence for deformation and neocrystallization of micas is more abundant. Biotite still remains relatively tabular and shows minimal evidence of replacement by chlorite. However, coarse-grained muscovite shows evidence for intense intracrystalline deformation such as bent folia or deformation bands, kink folding, and micro-boudinage. Bent folia are the result of internal lattice slip (Figure 7C-F) (Vernon, 2018). Similarly, kink folding along the (001) crystallographic plane resembles twinning but differs in that kink folding is not restricted to crystallographic planes (Figure 7F). Muscovite grains exhibit micro-boudinage sub-parallel to foliation and in the lineation direction (Figure 7D). Microtextural evidence of shear is also recorded in the external shape of muscovite as it commonly occurs in a fish geometry. These fish are typically ~150 – 400 μm in length and form parallel to the main foliation along with other (feldspar) porphyroclasts. Muscovite fish in the Coyote Mountains detachment shear zone mylonites typically form fish from groups 1, 2, and rarely 5 according to the ten Grotenhuis et al. (2003) classification (Fig. 7C-F). The fish geometry shows a consistent top-to-the-north sense of motion, consistent with other kinematic indicators. Locally the muscovite fish themselves are also folded. Neocrystallized fine-grained muscovite again occurs as local sericitization of feldspars, in microfractures in quartz and feldspar (Fig. 7B, D) and is more abundant in the matrix than in protomylonite samples (Figure 7D-F). Additionally, fine-grained micas form tails on coarse muscovite porphyroclasts (Figure 7D) and locally form contiguous folia that extend for millimeters (Figure 6F, 7D).

4. QUARTZ CRYSTALLOGRAPHIC PREFERRED ORIENTATION AND GRAIN SIZE ANALYSIS

4.1. Methodology

The crystallographic preferred orientation (CPO) of quartz was investigated on thin sections cut perpendicular to foliation and parallel to lineation, using the Electron Backscattered Diffraction (EBSD) method. Measurements we acquired on a JEOL IT300 SEM equipped with a LaB_6 filament and an Oxford Instruments EBSD detector on uncoated samples in low vacuum (30Pa) at 25 kV excitation potential and 60 μA probe current.

In order to investigate the CPO of a large population of grains and cover a large area of a thin section, a 50 μm step size was used and the results were plotted by one measure per grain over at least 800 grains, using a 10° misorientation to define grain boundaries. For grain size analysis, smaller areas (~6 mm^2) were surveyed with a 2 μm step size, and a minimum of 3 measurements per grain and a 10° misorientation to define grain boundaries (Figure 8 and Supplementary Figure S1). Recrystallized grains were extracted from the total grain population based on internal misorientation, following the methodology described in Cross et al. (2017). Quartz c- and a-axis (lower hemisphere) pole figures were generated using MTEX MATLAB toolbox.

4.2. Quartz Crystallographic Preferred Orientation Results

Quartz deformation is dominated by dislocation creep processes, and recrystallized quartz grains display a strong crystallographic preferred orientation (CPO). Quartz c-axis fabrics show a typical Type-I cross-girdle (Figure 8, Lister, 1977). Analysis of quartz CPO by EBSD reveals that the slip systems active during quartz recrystallization included basal ⟨a⟩, rhomb ⟨a⟩, and/or prism ⟨a⟩ slip (Figure 8, Schmid and Casey, 1986). Sample CM16-04 show c-axis girdle with a maxima indicating dominant rhomb ⟨a⟩ and prism ⟨a⟩ slip, with minor basal ⟨a⟩ slip. The c-axis girdle is broad and symmetrical, and the a-axis pole figure show strong peripheral maxima, suggesting that this fabric developed under dominantly coaxial deformation conditions. Samples CM14-01 and CM14-03 show similar c-axis girdles, also dominated by rhomb ⟨a⟩ and prism ⟨a⟩ slip, and minor basal ⟨a⟩ slip. In these cases, however, the c-axis girdle is narrower, and shows a dextral asymmetry, suggesting that these fabrics developed under non-coaxial deformation, with a component of top-to-the north shear (Schmid and Casey, 1986; Barth et al., 2010). Sample CM16-10A shows a c-axis girdle with a prism ⟨a⟩ slip maxima, and a stronger contribution of basal ⟨a⟩ slip than the previous samples. The c-axis girdle is broad, with a central bullseye; the basal ⟨a⟩ maxima give a dextral asymmetry to the girdle. The a-axis pole figure shows strong peripheral maxima with a dextral rotation. Samples CM16-11 and CM14-07 c-axis girdles are both characterized by a strong rhomb- and basal ⟨a⟩ maxima, with minor prism ⟨a⟩. The c-axis girdles have narrow central branch, but wider arms. Quartz a-axis fabrics form a central girdle, with peripheral maxima, indicative of strong basal ⟨a⟩ slip (Barth et al., 2010). For these two samples, both c- and a-axis girdles show dextral asymmetry, strongly expressed in CM14-07.

The quartz c- and a-axis fabrics change with structural position in the detachment shear zone and associated degree of mylonitization: samples located closest to the top of the DSZ (high strain) show deformation by basal ⟨a⟩ slip, while samples located in deeper structural levels (low strain) express a stronger contribution of prism- and rhomb ⟨a⟩ slip (Figure 8). In addition, with the exception of sample CM16-04, all the quartz c-axis pole figures show a strong dextral asymmetry compatible with a top-to-the-north sense of shear, suggesting that the detachment shear zone experience a non-coaxial component of deformation (Passchier and Trouw, 2005; Barth et al., 2010).

Quartz lattice preferred orientation change as a function of temperature, due to the change in the activity of the dominant slip systems (e.g. Passchier and Trouw, 2005). Basal ⟨a⟩ slip is prevailing at low temperature, imparting a strong cluster of c-axes in the periphery of the girdle, associated with ⟨a⟩-axes maxima. Samples CM16-11 and CM14-07, located close to the top of the shear zone, exhibit c-axis girdles with strong rhomb- and basal ⟨a⟩ maxima, and ⟨a⟩-axes, with peripheral maxima, suggesting low- to medium deformation temperature.

With increasing temperature, prism ⟨a⟩ slip becomes more important and the girdle develops a maximum around the center of the pole figure, normal to the flow plane, while ⟨a⟩-axes maxima are replaced by a single ⟨a⟩-axes maximum parallel to the movement direction (e.g. Passchier and Trouw, 2005). At deeper structural levels, samples CM16-04 and CM14-01 exhibit a central c-axes girdle dominated by rhomb- and prism ⟨a⟩ slip, and a single ⟨a⟩-axes maxima, suggesting deformation lo- to medium deformation temperature. Altogether, the quartz fabrics are indicative of relatively moderate temperatures of deformation, between 400 and 550°C, consistent with our optical observations of quartz and feldspar deformation textures (e.g. Schmid and Casey, 1986; Stipp et al., 2002; Passchier and Trouw, 2005).

4.3. Recrystallized Grain-Size Paleo-Piezometry

Recrystallized grain size paleopiezometers are based on the relationship between the size of dynamically recrystallized grains and applied differential flow stress, derived from deformation experiments (see Tokle et al., 2019 and references therein). Here we use the Cross et al. (2017) quartz recrystallized grain sized piezometer. This piezometer does not include stereological correction; therefore, our grainsize estimates are not corrected for consistency (Table 1).

Grain size analysis was conducted by EBSD on areas covering ~6 mm^2, using a 2 μm step size. Recrystallized grains were extracted from the total grain population based on internal misorientation, following the methodology described in Cross et al. (2017). The measured grain size ranges from 13 μm to 46 μm, with 5 out of 8 measurement around ~24 ± 3 μm (Table 1). This recrystallized grain size determined yields a flow stress ranging from 39 to 96 MPa (Table 1).

5. GEOCHRONOLOGY

5.1. Methodology

5.1.1. U-Th-Pb Dating

Zircon mineral separation for a garnet-two-mica granite sample CM14-04 (~0.5 kg) was performed at the Laboratorio de Caracterización Mineral (CarMINLab) at Centro de Geociencias, Universidad Nacional Autónoma de México (UNAM), using conventional methods (crushing, sieving, magnetic separation, and heavy liquids). Zircons for U-Pb geochronology were mounted in epoxy resin and grounded to nearly half their thickness using abrasives. Transmitted and reflected-light photos (not shown) were taken of all mounted zircon grains to aid in the spot selection to perform the laser ablation ICP-MS studies. In addition, scanning electron microscope-cathodoluminescence images (SEM-CL) of all zircons were obtained at the CarMINLab and used to reveal internal zoning and aide in analytical spot placement.

U-Th-Pb zircon geochronology of the granite sample was conducted in the Laboratorio de Estudios Isotópicos (LEI) at Centro de Geociencias, UNAM, using a Resonetics Workstation model M050 equipped with a LPX220 excimer laser coupled with a Thermo ICap Qc quadrupole ICP-MS (inductively coupled plasma–mass spectrometer) following analytical techniques similar to those reported in previous publications by Solari et al. (2010) and González-León et al. (2016).

Sample spot beam locations are ~23 μm in diameter. To account for down-hole fractionation observed in the primary standard zircon, the data reduction was performed using the commercial software "Iolite 2.5" by Paton et al. (2010, 2011), employing the VisualAge data reduction scheme presented in Petrus and Kamber (2012). The primary zircon-bracketing standard used was 91500 (Wiedenbeck et al., 1995; TIMS age of 1065.4 ± 0.6 Ma) whereas PLE standard (Plešovice; Sláma et al., 2008; TIMS age of 337.13 ± 0.37 Ma) was used as secondary standard control. All uncertainties were propagated using Iolite protocols and are reported at 2-sigma level of precision (Table 2). The data were exported from Iolite and plotted with computational software "Isoplot 3.0" (Ludwig, 2012) and shown in a concordia diagram and a weighted mean age plot (Figure 9A, B). No common Pb correction was applied to the geochronology data because the ^{204}Pb signal is insignificant in comparison to the overwhelming ^{204}Hg signal present in the system. Zircon trace-element data are presented in Table 3.

5.1.2. $^{40}Ar/^{39}Ar$ Dating

Biotite and muscovite mineral separate pairs were prepared for 11 of the 20 Pan Tak Granite (Tg) samples examined petrographically. These minerals were selected for dating because their nominal closure temperatures for Ar diffusion span the greenschist facies, which, based on microstructural study (see below) is the grade of deformation in Coyote Mountain shear zone. We selected samples that span the range of deformation intensity, from protomylonite (CM16-02) to mylonite (CM16-14). Samples were crushed and milled down to a millimeter grain size, then sieved. Coarse-grained (>250 µm) muscovite and biotite mineral separates were prepared by iteration between paper shaking and magnetic separation with a Frantz L1 magnetic separator. A final stage of hand picking was done on a binocular microscope to remove remaining impurities and visibly altered biotite grains (but see Discussion). All mineral separates were washed sequentially in acetone, alcohol, and deionized water (3x) prior to irradiation.

Single and multi-grain aliquots of the mineral separates were loaded in high purity copper foil and irradiated in the central thimble of the USGS TRIGA reactor in Denver, Colorado, for 20 megawatt hours in a geometry similar to that described in McAleer et al. (2017). Cadmium shielding was not used. All isotopic analyses were completed at the USGS-Reston $^{40}Ar/^{39}Ar$ Geochronology Laboratory. Fish Canyon Tuff sanidine, with an astronomically tuned age of 28.201 ± 0.046 Ma (Kuiper et al., 2008) was used as the neutron fluence monitor. Values for interfering isotopes of $(^{40}Ar/^{39}Ar)_K$ = 9.1E-3 ± 9.3E-4; $(^{38}Ar/^{39}Ar)_K$ = 1.278E-2 ± 3.6E-5; $(^{37}Ar/^{39}Ar)_K$ = 4.2E-4 ± 3.4E-4; $(^{39}Ar/^{37}Ar)_{Ca}$ = 7.5E-5 ± 1.8E-5; $(^{38}Ar/^{37}Ar)_{Ca}$ = 6.80E-4 ± 2.7E-6; $(^{36}Ar/^{37}Ar)_{Ca}$ = 2.490E-4 ± 7.7E-7; were determined on co-irradiated CaF_2 and zero-age K-glass.

Following irradiation, unknown samples were heated in low-blank furnaces similar to that described by Staudacher et al. (1978). The evolved gasses were then purified in two-stage ultra-high vacuum extraction lines, and analyzed on a VG Micromass 1200 noble gas mass spectrometer, operating in static mode (McAleer et al., 2017). The argon isotopes were measured by peak hopping using a SEV217 electron multiplier. Isotopes were measured in 6 cycles and the time-zero intercepts were determined by linear regressions of the data.

Data from the VG1200 were reduced using a modified version of ArAr* (Haugerud and Kunk, 1988) and Isoplot (Ludwig, 2012). A plateau age was defined as a set of contiguous steps containing > 50% of the $^{39}Ar_{K}$ where the probability of fit of the weighted mean age of the steps is > 5% (Figures 10 and 11, Table 4). In cases where the MSWD exceeded 2.5 the uncertainty was expanded by the square root of the MSWD (Ludwig, 2012). To maintain consistency with Kuiper et al. (2008) the decay constants of Min et al. (2000), and the argon isotopic composition of Lee et al. (2006) were used in data reduction. Constants and complete isotopic data can be found in the data tables in Supplementary Table S1.

5.1.3. Apatite Fission track Dating and Thermal History Modelling

Apatite fission-track analyses were performed on two Pan Tak Granite samples using the external detector method (Tagami, 1987). Apatite grains were mounted in epoxy and polished, and spontaneous fission tracks were revealed by etching with 5.5-M nitric acid for 20 s at 21°C before irradiation. The neutron fluence was monitored using CN5 U-doped glass (Bellemans et al., 1995). The irradiation was performed at Oregon State University. After irradiation, mica external detectors were etched in 40% hydrofluoric acid for 45 min at 21°C. Analyses were conducted for optical identification of fission-tracks using an Olympus microscope at 1,600X magnification with a drawing tube located above a digitizing tablet and a Kinetek computer-controlled stage driven by the FT Stage program provided by Trevor Dumitru of Stanford University. The fission-track analyses were performed at the Arizona Fission Track Laboratory in the University of Arizona (Table 5 and Supplementary Table S2 & S3).

Confined tracks were also measured to enable thermal history modelling (e.g. Gleadow et al. 1986, Donelick & Miller 1991). Confined tracks do not intersect the surface and are revealed within the apatite where the etchant has gained access to the grain sub-surface via other tracks and fractures (Gleadow et al. 2002). The distribution of measured confined track lengths provides information on the time spent in the

120-60°C apatite partial annealing zone (APAZ), with longer mean confined track lengths defining rapid cooling through (>13.5µm) the APAZ and shorter mean confined track lengths demonstrating prolonged residence in the APAZ (e.g. Laslett et al. 1982, Tagami & O'Sullivan 2005).

5.1.4. Thermal History Modelling

A single, combined thermal history model was produced for samples CP-01 and CP-02 using their AFT ages, confined track length distributions, D_{par} (Donelick et al. 2005) as the kinetic parameter and zircon U-Th-Pb, muscovite Ar-Ar, and biotite Ar-Ar ages as high temperature constraints (Figure 12; Supplementary Table S4). The QTQt software (version 5.7.0) was used, which applies Bayesian trans-dimensional Markov Chain Monte Carlo statistics to determine models for the cooling pathway of the sample (Gallagher, 2012). An initial unconstrained run is performed to explore the statistical space, followed by adjustments to the search parameters or the addition of geological constraints where necessary. This approach follows the Bayesian philosophy of the software, which seeks to minimize the complexity of the model by statistical means. Many iterations (>> 10,000) are run to generate a range of models that create a probability distribution, from which individual models can be selected, including the maximum likelihood and "expected" (weighted mean) paths. The range of the general prior was set as t = AFT central age ± AFT central age, temperature = 70 ± 70°C. Acceptance rates for models were between 0.2 and 0.6 and birth-death ratio was ~1. The annealing model from Ketcham et al. (2007) was used for fission track data with D_{par} (the average etch-pit diameter) as the kinetic parameter as it can be used as a proxy for apatite chemistry. More details on the modelling approach can be found in Gallagher (2012) and Supplementary Table S4.

5.2. Results

5.2.1. U-Th-Pb Data

Approximately 150 zircons, mostly euhedral crystals of ~70–200 µm in size, were mounted and characterized using transmitted and reflected-light microscopy images in addition to SEM-CL (Figure 11). Based on these zircon images 40 grains were selected for U-Pb zircon geochronology using the laser ablation ICP-MS technique (see Table 2). The collected U-Th-Pb zircon data were plotted in a Terra-Wasserburg concordia diagram (Figure 11A) and 39 of 40 analyses overlapped concordia at 2 sigma. A group of 15 concordant zircon analyses were selected to calculate a $^{206}Pb/^{238}U$ weighted mean age of 58.1 ± 0.5 Ma (Figure 11B; Mean Squares of Weighted Deviates (MSWD = 2.3; n = 15) that we interpret as the age of crystallization of the Pan Tak garnet-two-mica Granite sample CM14-04. Nine analyses with high uranium content (5800 – 22000 ppm) yielded slightly younger ages and were excluded from the weighted mean age calculation (Figure 11B). Eight older concordant ages of Cretaceous, Jurassic, and Mesoproterozoic are interpreted to be inherited cores (Figure 11A, D).

5.2.2. $^{40}Ar/^{39}Ar$ Data

Muscovite - Ten of the 11 step-heating experiments on muscovite yield plateau ages, and sample CM16-12 also has a flat age spectrum. In most samples there is a small (<1 Ma) increase in age over the last ~10% of the $^{39}Ar_K$ released, and so the total gas age is slightly higher than the plateau age in all samples (Table 4). This is true for single grain and multi-grain aliquots. Steps included in plateau ages yield Cl/K ratios that are < 0.01 and typically < 0.001, and Ca/K ratios of < 0.01, consistent with the degassing of muscovite. Elevated Cl/K and Ca/K ratios are observed in the first and last ~5% of the $^{39}Ar_K$ release in some samples. Eight of the 11 sample define a narrow age range and yield plateau ages between 29.12 and 29.39 Ma. The other three samples yield plateau ages of 30.50, 30.15, and 30.73 Ma (Figures 9 & 10, Table 4).

Biotite - In contrast to the muscovite data, no biotite step-heating experiments yield plateau ages. All biotite age spectra climb steeply in age over the first ~15% of the $^{39}Ar_K$ release, and then gently climb in age up to ~70% of the $^{39}Ar_K$ release. At 70–80% release there is a steep climb (CM16-04, CM16-06) or drop (all other samples) in age, and this is followed by a climb in age for the remainder of the age spectrum. The age spectrum shape is commonly mirrored by the Ca/K and Cl/K data (Figure 9), indicating significant compositional changes are associated with age changes. Biotite total gas ages vary widely, with 10 of 11 ages falling between 19–28 Ma, and these ages show no systematic trend with elevation. Sample CM16-10A is anomalous and yields a total gas age of 62 Ma (Figure 9, Table 4).

5.2.3. Apatite Fission Track Data

Two samples of Pan Tak Granite were obtained for AFT analysis. Samples CP-01 and CP-02 yielded AFT ages of 24.1 ± 2.4 Ma and 24.8 ± 3.1 Ma, respectively. Both samples satisfy the chi-squared test (> 5%) with $P(\chi^2)$ of 1.0 and 0.13, respectively, implying that both single-grain age distributions represent a single population (Table 5 and Supplementary Tables S1 & S2). Both samples yielded long mean track lengths (MTLs) of 13.7 ± 0.9 μm and 13.6 ± 0.9 μm, respectively (Table 5).

5.2.4. Thermal History Modelling

Thermal history modelling was conducted on samples CP-01 and CP-02. Both samples yielded long, unimodal mean track lengths and AFT ages that were within 2σ of the muscovite and biotite Ar-Ar ages identified in the mylonitized zone. Thus, it was deemed geologically viable to perform thermal history modelling. The combined thermal history model, used the AFT annealing model from Ketcham et al. (2007). Zircon U-Pb, muscovite Ar-Ar, and biotite Ar-Ar data from the mylonitized transect were integrated into thermal history models (Figure 12 and Table 2 & 4). Individual models, confined track distributions, and modelling parameters are available in Supplementary Figure S2.

Samples CP-01 and CP-02 were combined in a single thermal history model due to their close spatial proximity. The thermal history model constrains two phases of cooling; the first protracted cooling postemplacement of the Pan Tak Granite between 58 and 30 Ma. Followed by a single, extremely rapid period of cooling from mid-crustal temperatures (~400°C) to the apatite partial annealing zone (APAZ, 120 − 60°C) from 29 to 25 Ma, constrained through 2σ overlapping Ar-Ar and AFT dates, before experiencing rapid cooling trough the APAZ at 24 Ma as constrained by the long MTLs (Figure 12).

6. DISCUSSION

Combined structural, microstructural, and geochronologic results provide important new insight into the evolution of the Coyote Mountains MCC. Specifically, the conditions and timing of mylonitization and the exhumation history of the detachment shear zone are discussed below.

6.1. Age of the Pan Tak Granite

Wright and Haxel (1982) reported a lower intercept age of 58 ± 2 Ma from multi-grain TIMS analyses of five size fractions of zircon from the Pan Tak granite and an upper intercept age of ~1.1 Ga. The new LA-ICP-MS $^{206}Pb/^{238}U$ age of 58.1 ± 0.5 Ma confirms and improves the precision of an early Paleogene age for the Pan Tak Granite. These data are consistent with the Pan Tak Granite being a late Laramide pluton as previously suggested (Wright and Haxel, 1982). The documentation of inherited cores (Figure 9A, D) also explains the discordant results of Wright and Haxel (1982), though the presence of Cretaceous, Jurassic, and Mesoproterozoic cores suggests the upper intercept age of Wright and Haxel (1982) is unlikely to have geologic meaning.

6.2. Conditions of Mylonitization

The Pan Tak Granite is overprinted by the Coyote Mountains detachment shear zone. Macroscopically, the fabric ranges from protomylonite to mylonite, exhibiting an increase in fabric intensity northward and towards the Ajo Road décollement.

Feldspars microstructures, such as flame perthite, myrmekite, bent twins in plagioclase, abundant microfracturing, and patchy zoning (Figure 6), provide evidence for both ductile and brittle deformation, and are collectively consistent with a top to the north sense of shear. Altogether feldspar microstructures suggest that the Coyote Mountains detachment shear zone developed under greenschist facies conditions (~450 ± 50°C), close to the brittle-ductile transition for feldspar. The presence of mica fish in Pan Tak Granite samples is the most informative strain indicators present providing the sense of shear. Pan Tak Granite mica fish indicate a top-to-the-north shear sense, which correlate to macrostructural shear sense indicators

Qualitatively, deformation conditions recorded in quartz microstructures are consistent with deformation conditions deduced from feldspar microstructures. Quartz dislocation creep dynamic recrystallization is dominated by subgrain rotation and limited grain boundary migration (regime II and III of dislocation creep of Hirth and Tullis, 1992). The presence of elongated quartz ribbons, in conjunction with intracrystalline dislocation glide quartz microstructures, such as deformation lamellae, and patchy extinction, suggest deformation without brittle fracturing under high differential stress and/or high strain rate condition where recovery within the quartz lattice cannot accommodate strain.

EBSD data from quartz provide additional data on deformation conditions. Quartz CPO measured by EBSD reveal that recrystallization occurred by a combination of basal-, rhomb-, and prism ⟨a⟩ slip, indicative of relatively moderate temperatures of deformation, between 400 and 550°C, consistent with our optical observations of quartz and feldspar deformation textures. The quartz c- and a-axis fabrics appear to change with degree of mylonitization: mylonitic samples located at deeper structural levels (low strain) in the detachment shear zone show deformation by prism- and rhomb ⟨a⟩ slip associated with dominant grain boundary migration recrystallization, while ultramylonitic samples near the top of the detachment shear zone (high strain) express a stronger contribution of basal ⟨a⟩ slip associated with recrystallization by subgrain rotation. In addition, a majority of the quartz fabrics show a strong asymmetry compatible with a top-to-the-north sense of shear.

The presence of grain boundary migration recrystallization in quartz, combined with prism- and rhomb ⟨a⟩ slip observed in quartz c-axis pole figures suggests the maximum temperature of deformation in the Coyote Mountains shear zone was 500ºC. However, these microtextures are comparatively rare relative to subgrain rotation recrystallization microstructures associated with basal-, prism-, and rhomb ⟨a⟩ slip quartz c-axis polefigures, more indicative of deformation at 400 – 450ºC (Figure 12). Given that the geometry of these microstructures all display a consistent shear sense (Figure 12) we suggest these microstructures record deformation conditions during extension-driven exhumation along the Coyote Mountains detachment shear zones. Close to the top of the detachment shear zone, the mylonite is locally brecciated (Gardulski, 1980; Wright and Haxel, 1982; Davis et al., 1987), suggesting localization of deformation off the broader Coyote Mountains detachment shear zone and onto the Ajo road décollement as the rocks exhumed into the brittle regime.

6.3. Flow stress and strain rate of the Coyote Mountains detachment shear zone

Our microstructural analysis reveal that in the Pan Tak Granite mylonite the quartz is entirely dynamically recrystallized, dominantly by subgrain rotation, with minor grain boundary migration. Quartz recrystallized grain size measured by EBSD ranges from 13 to 46 μm, with an average of ~25 μm; 5 out of 7 samples displaying an average grain size of ~24 ± 3 μm (Table 1). Using the quartz recrystallized grain size of Cross et al. (2017), this recrystallized grain size suggests that the mylonite recorded a flow stress of ~67 ± 28 MPa (Table 1).

The paleopiezometry results can be used to further constrain the strain rate experienced by the detachment shear zone, by applying a dislocation creep flow law. We use the Hirth et al. (2001) quartzite dislocation creep flow law, for which the stress exponent n is 4, the activation energy Q is 135 kJ/mol, and a temperature of 500 ± 50°C. Water fugacity has a strong effect on strain rate but is difficult to estimate accurately (e.g. Hirth et al. 2001). The Pan Tak Granite mylonite preserves evidence of water during deformation as indicated by the abundance of fluid inclusions in quartz grains. We estimate a maximum value for the water fugacity during deformation by assuming that water was present at a temperature of 500ºC and hydrostatic pressure at 11 – 14 km (108 – 138 MPa). A f_{H2O} of 50 MPa was estimate for these conditions using standard water fugacity coefficients (Töheide, 1972). Using these parameters, we obtain an average strain rate of 5.0 $\times 10^{-12}$ s^{-1}, which is typical for detachment shear zones (Figure 13, Gottardi and Teyssier, 2013). Applying the Rutter and Brodie (2004) flow law to our stress and temperature estimates appear to overestimate the strength of the shear zone, with values beyond the range of geologically reasonable strain rates for actively deforming areas (10^{-12} to 10^{-15} s^{-1}) (Figure 13). Our strain rates results (10^{-11} s^{-1} to 10^{-13} s^{-1}) match early to middle Miocene strain rate estimates in the nearby Colorado River extensional corridor range from 10^{-15} to 10^{-12} s^{-1} (Gans and Bohrson, 1998; Campbell-Stone and John, 2002; Behr and Platt, 2011; Singleton et al., 2018). Using a warm geotherm ranging from 35°C to 45°C/km, as suggested in the CRER during this time period (Foster et al., 1991; Howard and Foster, 1996) we estimate that the detachment shear zone evolved at a depth ranging from 11 to 14 km (Figure 13).

6.4. Timing of mylonitization of the Coyote Mountains detachment shear zone

Critical to the interpretation of the $^{40}Ar/^{39}Ar$ isotopic results is evaluating the relative contributions of thermally activated diffusion and recrystallization in driving the preserved isotopic ratios. Petrographic characterization demonstrates that there are three textural populations of muscovite present in the Pan Tak Granite: (1) coarse-grained porphyroclastic muscovite of presumable igneous origin (Figure 7C-F), (2) ultra-fine aggregates (<20 μm) that form tails on the porphyroclasts and define variably contiguous folia (Figure 6E), and (3) ultra-fine aggregates that partially replace feldspars (Figure 6D). The only population amenable to physical mineral separation was the coarse-grained population, and that was what was analyzed in our step-heating experiments. However, the presence of populations 2 and 3 clearly demonstrate that post-magmatic growth of muscovite occurred in these samples, and the presence of some fine micas at the margins of some coarse micas (Figure 7B, D), as well as their fish geometry, suggests that the dated grains may be partially composed of metamorphic muscovite. Given the microstructural evidence that MCC related deformation occurred at upper greenschist facies conditions, it is at least plausible that partial recrystallization of muscovite fish occurred below the closure temperature for argon diffusion in muscovite.

All step-heating experiments on muscovite yield plateaus ages, regardless of whether on single grain, several grain (<10), or many grain aliquots. In addition, 8 of the 11 analyzed samples yield plateau ages that define a narrow age range of 29.12 – 29.39 Ma despite being from samples that span a range of deformation intensities (proto- and mylonite). The fact that the step-heating experiments result in plateau ages indicate that if there are multiple age/composition populations in the dated coarse muscovite grains, they do not have different degassing behavior in-vacuo, or that one age component contributes so little to the total Ar budget that it makes little difference to the spectrum. Since the neocrystallized muscovite is very fine grained (<20 μm) (Figure 7B, 7D), it should degas first. If these neocrystallized muscovite grains composed a significant proportion of an aliquot, and were significantly younger, then the early degassing steps should yield a young age; however they do not. We therefore conclude that either (1) the fine-grained recrystallized muscovite is not present at the margins of the dated grains, or that it is in such low proportion that it cannot be detected, or (2) that recrystallized muscovite is present, and yields a distinct age that is within error limits of the age of the coarser muscovite. This latter interpretation would be consistent with a detachment shear zone that was exhumed rapidly. Based on these observations we conclude that the footwall of the Coyote Mountains detachment shear zone passed rapidly through closure temperature of muscovite at ~29 Ma.

The biotite age spectra are interpreted to reflect variable alteration of the dated biotite grains rather than strictly the thermal history. Many studies have documented that $^{40}Ar/^{39}Ar$ analysis of biotite can be problematic, especially in metamorphosed rocks where fluid ingress leads to chloritization and typically anomalously young ages (e.g., Gabber, 1991; Ruffet et al., 1991; Roberts et al., 2001; DiVincenzo et al., 2003). Additionally, the relatively high solubility of argon in biotite can lead to the incorporation of excess argon and anomalously old ages (e.g., Kelley, 2002). It appears that both cases are present in the Coyote biotites. Although the biotite grains selected for dating appeared unaltered under the binocular microscope, incipient chloritization of biotite was optically apparent in most thin sections (Figure 7). Additionally, the observed age spectrum shape is similar to that published for chloritized biotite (Lo and Onstott, 1989). Coupled with the fact that the step-heating experiments yield, Ca/K and Cl/K ratios inconsistent with the degassing of only biotite, it seems likely that the isotopic data are compromised by alteration of some sort. Additionally, biotite from sample CM16-10A yields age steps older than crystallization age of the granite and is clearly affected by excess argon. The muscovite from this sample also yields the oldest total gas age (31.24 Ma) consistent with the presence of excess argon as well as the lower solubility of argon in muscovite (Kelley, 2002).

We interpret the flattest biotite age spectrum (CM16-11, Figure 9) to be the least affected by alteration and to best approximate the time of cooling through closure for biotite in the Coyote Mountains. This sample yields a total gas age of 28.25 Ma only slightly younger than the muscovite total gas age of 29.56 Ma (plateau age at 29.39 ± 0.10 Ma).

6.5. Exhumation and Cooling of the Coyote Mountains detachment shear zone

Primary zircon in the Pan Tak Granite crystallized at 58.1 ± 0.5 Ma. The temperature of melt that was extracted to crystallize the Pan Tak Granite is not known, but the relatively common occurrence of inherited cores in Pan Tak zircon grains (Figure 9, see also Wright and Haxel, 1982) suggests that the Pan Tak was a “cold” granite (Miller et al., 2003) and we approximate the melt temperature at 750°C. However, a regional peak metamorphic grade in the lower amphibolite facies (Haxel et al., 1984) indicates that the Pan Tak Granite intruded rocks that were no hotter than 550°C. Our data do not constrain the cooling history of these rocks between 58 and 30 Ma, however the regional geology does not suggest any prograde metamorphism following intrusion (Haxel et al., 1980a, b, 1984), and 29.3 Ma $^{40}Ar/^{39}Ar$ muscovite ages suggests very little net cooling and exhumation over this nearly 30 Myr time interval. The period of tectonic quiescence is in marked contrast to the rapid cooling in the Oligocene indicated by the thermochronometric data. Using our best estimate of 29.3 Ma for the passage through muscovite Ar closure and 28.3 Ma for the passage through biotite closure, we can calculate an approximate cooling rate for the Coyote MCC through greenschist facies. Since the muscovite grains are deformed in all samples (Figure 7) it is likely that the diffusion domain size is smaller than the grain size (~1 mm) and we use a nominal diffusion domain size of 100 μm. Additionally, we use the diffusion coefficients (D_o = 20cm^2/s, E_a = 268KJ/mol) of Harrison et al. (2009) at 5 Kb, as higher pressures are unlikely in an extensional setting. Similarly for biotite, we use a nominal diffusion domain size of 100 μm and the diffusion coefficients from Grove and Harrison (1996) for biotite (D_o = 7.5E-2 cm^2/s, E_a = 197 KJ/mol). Using these parameters, the T_c for muscovite and biotite at cooling rates ranging from 10–100^{o}C/Ma is 405 – 435 and 290 – 320^{o}C, respectively. In other words, the rocks cooled ~100^{o}C over a ~1 Ma time period. This estimate is strongly dependent on our interpretation that the flattest biotite age is the best estimate of the time of cooling through biotite closure. However, two AFT ages of ~24 Ma strongly support that our discarded younger biotite ages were in fact compromised by alteration. We also note that 7 muscovite samples yield the same plateau age despite being from rocks collected over an elevation range of ~400 m and despite significant variation in the deformation intensity of muscovite among those samples (Figures 7 and 8). Based on microtextural evidence it might be expected that these muscovite grains would have significantly different average diffusion domain sizes and therefore closure temperatures and ages, yet they yield the same age. One explanation for these results is that samples cooled so rapidly through the greenschist facies that differences in the relative distance in the shear direction, and in the closure temperature, which might result from differences in diffusion domain size (e.g., ΔTc = 35°C from 200 to 50 μm diffusion domain), yield little change in age at the precision of our measurements.

Microstructural analysis of the mylonitic fabric suggest that the maximum temperature conditions during initiation of the shear zone were 500 ± 50°C. The temperature of this grade of metamorphism is only slightly higher than the closure temperature for argon diffusion in muscovite. Therefore, we suggest that although the argon isotopic system records a cooling age, that age closely approximates the time of development of the microstructures, i.e. the time of mylonitization and deformation along the shear zone (Figure 12). However, with existing data we cannot unequivocally rule out that the mylonitization occurred significantly earlier.

The similar $^{40}Ar/^{39}Ar$ muscovite and biotite ages suggest that by early Oligocene, the northern end of the Baboquivari Mountains was exhuming along the Coyote Mountains detachment shear zone to form the Coyote Mountains MCC. Perhaps most striking is the fact that AFT cooling ages and mean track lengths in conjunction with the $^{40}Ar/^{39}Ar$ data indicate that a rapid cooling rate of ~75°C/Ma, persisted for several million years such that the footwall of this detachment cooled from 400 to 100°C in only ~4 Ma (Figure 12). Similar rapid cooling rate have been estimated for other Cordilleran MCCs (Figure 14). Our results are almost identical to cooling rates of ~75°C/M.y. between 350 and <100°C reported on the nearby Catalina-Rincon MCC by Davy et al. (1989).

6.6. Implications for orogenic collapse in southeastern Arizona

The coalescence of several tectonic ingredients help lead orogenic collapse, these include (1) an increase gravitational potential energy, typically driven by crustal thickening; (2) the presence of properly oriented zones of mechanical weakness that act to localize and accommodate strain; (3) a source of thermal energy that can bring thermal instability to the crust (higher geothermal gradient, shallow brittle-ductile transition, or reduction in lower crustal viscosity); and (4) a change in plate boundary conditions (e.g., Rey et al., 2001; Teyssier et al., 2005). Published work and our new data provide some constraints on each of these ingredients in the Coyote Mountains.

The southern MCCs, of which the Coyote Mountains are a part, are unique compared to the northern ones in the fact that they are located within an area characterized by Laramide shortening of the craton (e.g., Coney, 1980; Coney and Harms, 1984; Spencer and Reynolds, 1990). The exact style of Laramide deformation as well as the timing and magnitude of shortening remains poorly constrained, owing to the subsequent widespread extensional tectonics, including both metamorphic core complex and

Basin and Range extension that overprinted most of these structures (see Favorito and Seedorff, 2018 and references therein). However, recent work examining the geochemistry of continental-arc rocks by Chapman et al. (2020) suggests that the crust of the southern United States Cordillera (western and southern AZ, northern Sonora) was 57 ± 12 km thick during the Laramide orogeny. This crustal thickness could have supported a high-elevation (~3 km paleoelevation), low-relief orogenic plateau (Chapman et al., 2020) resulting in an excess of gravitational potential energy. As mentioned above, the southern MCCs are in an area characterized by Laramide shortening. As a result, contractional structures are widespread (e.g., Favorito and Seedorff, 2018; Spencer et al., 2019), and include the Baboquivari thurst (Wright and Haxel, 1982; Haxel and Wright, 1984). Evidence for reactivation of an earlier structure is not present here (Gardulski, 1980; Haxel et al., 1984; Davis et al, 1987), and as far as we can tell the microstructures of the Coyote detachment shear zone are entirely extensional. However, in the Catalina-Rincon MCC there is evidence that detachment faulting reactivated a Laramide structure (Spencer et al., 2019). Although we cannot confirm this same relationship here, the Catalina-Rincon MCC is also cored by peraluminous granite, and it seems there is a spatial if not genetic relationship between these syn- to post-tectonic intrusions and later extension.

The Laramide orogeny of the southern U.S Cordillera was also accompanied by syntectonic intrusive activity, evidenced by the emplacement of a variety of Late Cretaceous to Paleocene peraluminous granitoids. These plutons have been interpreted to be the products of anatexis driven by Laramide thickening (Haxel et al., 1984; Dickinson, 1989, 1991). The ~58 Ma Pan Tak Granite, which makes up the core of the Coyote Mountains metamorphic core complex is one of these plutons, and in theory intrusion of these rocks into the mid crust could have resulted in a thermal instability accompanying the thickened crust at the end of the Laramide orogeny. However, our themochronologic data clearly indicate that rapid cooling and extensional exhumation post-dated Laramide plutonism by ~30 Ma in the Coyote Mountains, long after any perturbation to the crustal thermal structure would have equilibrated. Therefore if a thermal perturbation helped to drive the onset of MCC extension, we suggest it likely occurred at ~35 – 30 Ma. Evidence for magmatism of this age is common in southeastern

Arizona (e.g. Spencer and Reynolds, 1989). In the Coyote Mountains, the presence of scattered lamprophyric dikes with inferred minimum age of 24 Ma by Haxel and Wright (1982) suggests that exhumation was accompanied by some magmatic activity.

The Laramide orogeny was driven by subduction of the Farallon plate to the east under North America, which continued at a shallowing angle from the Paleocene to the Eocene (e.g., Yonkee and Weil, 2015). This resulted in Laramide orogenesis in southern Arizona at ~60 Ma, after which plutonism and deformation moved eastward (Coney and Reynolds, 1977). It is during this time of eastward migration that our thermochronologic data (and others, see Figure 14) suggest tectonic quiescence. Data from regional MCCs further help to constrain the picture. A regional synthesis of published $^{40}Ar/^{39}Ar$ ages reveals that interestingly, the 29 Ma age for the Coyote Mountains is slightly older than denudation/exhumation age reported in the Colorado River extensional corridor further west (23 – 18.5 Ma, Figures 2 and 14). In fact the ~24 Ma AFT age and the presence of an undeformed lamprophyric dike that crosscuts the brecciated Coyote Mountains detachment shear zone rocks estimated to be ~24 Ma (Wright and Haxel, 1982) suggests that extension was waning here as it was accelerating in the Colorado River extensional corridor (Figure 14). The nearby Catalina-Rincon MCC show a very similar cooling history to the Coyote Mountains (Figure 14). These data, though limited, suggest MCCs further east were exhumed earlier (during the Oligocene, between ~29 and 23 Ma) than the western MCCs (Miocene, between ~22 and 15 Ma). This observation could be explained by the westward propagation of volcanic activity and migration of the Mendocino Triple Junction around that time period. The westward sweeping magmatic activity, expressed by ignimbrites, has also been hypothesized to be associated with the roll-back or foundering of the Farallon plate during late Eocene to Oligocene through Miocene time (e.g. Coney and Reynolds, 1977; Coney, 1980; Armstrong and Ward, 1991; Dickinson, 2002; McQuarrie and Wernicke, 2005; McQuarrie and Oskin, 2010; Putiika and Platt, 2012). In southern Arizona and the Mojave region, the magmatic centers sweep westward starting at 36 Ma (McQuarrie and Oskin, 2010 and references therein). In addition, the northward migration of the Mendocino Triple Junction and the initial interaction of the ridge with the trench is estimated to have occurred around 28.5 Ma (e.g., McQuarrie and

Oskin, 2010; Putirka and Platt, 2012). The Laramide orogeny may have provided a crustal thickness and a structural architecture susceptible to orogenic collapse. However, the additional activation energy to trigger collapse might have been supplied 30 Myr later, both by heat flow to the lower crust and changes in far-field stresses driven by foundering of the Farallon plate. In as much as the effects of the foundering of the Farallon plate should be widespread, it is clear that the pre-existing structure was critical in defining where MCCs formed in the Cordillera (Coney, 1980; Coney and Harms, 1984). More geochronological datasets are required to better constrain the timing of denudation and exhumation of MCCs in southern Arizona and northern Mexico, and this would provide crucial information about the collapse of the southern Cordillera after the Laramide orogeny.

7. CONCLUSIONS

In this study we investigate the tectonics of the Coyote Mountains through its microstructural and thermochronologic record. The most significant contributions of our work are summarized as follow.

- The Pan Tak Granite, where the Coyote Mountains detachment shear zone is localized, was emplaced in Paleocene (~58 Ma zircon crystallization age) during the Laramide orogeny.
- $^{40}Ar/^{39}Ar$ geochronology of muscovite suggest that Oligocene mylonitization associated with the formation of the Coyote Mountains MCC occurred at ~29 Ma (early Oligocene).
- Apatite fission track ages indicate that the footwall of the Coyote Mountains MCC cooled below 110°C by ~24 Ma and, in conjunction with the $^{40}Ar/^{39}Ar$ data, confirm rapid cooling from the greenschist facies to < 110°C in the Oligocene.
- Mylonitization is recorded by a suite of microstructures that indicate that the detachment shear zone evolved under a strong component of non-coaxial (simple shear) deformation, at deformation conditions of ~450 ± 50°C, under a stress of ~65 MPa, and a strain rate of 5×10^{-12} s^{-1}, at depth of ~11 – 14 km.

- The 30My gap between Laramide shortening and rapid extension suggests that Laramide shortening/thickening may have provided the potential energy to help drive collapse, but an additional driving force, perhaps slab rollback and/or a change in plate boundary dynamics were necessary to trigger orogenic collapse and rapid extension.

Acknowledgements

This work was funded by the Louisiana Board of Regent Support Grant LEQSF(2015-18)-RD-A-28 (Gottardi). We would like to thank Irene Pérez-Casillas and Concepción Arredondo-de La Rosa from the CarMINLab (CGEO-UNAM) for their help with zircon mineral separation and SEM-CL characterization. In addition, we are very grateful to Carlos Ortega-Obregón (LEI) for his assistance calibrating LA-ICP-MS equipment and for supervising data reduction procedures for the U-Pb zircon geochronology. Andy Calvert is thanked for providing the zero age K-glass. Any use of trade, product, or firm names is for descriptive purposes only and does not imply endorsement by the U.S. Government. The data presented in this publication will be available on ScienceBase https://www.sciencebase.gov/about/. Archiving is underway and the data are temporarily available as Supporting Information for review purposes. Finally, we gratefully acknowledge Tectonics editor John Geissman, associate editor, and detailed and constructive reviews by Jay Chapman, John Singleton, Peter Valley and an anonymous reviewer that greatly improved this manuscript.

REFERENCES

Anderson, J. L., Barth, A. P., & Young, E. D. (1988). Mid-crustal Cretaceous roots of Cordilleran metamorphic core complexes. Geology, 16(4), 366–369. doi:10.1130/0091-7613(1988)016<0366:MCCROC>2.3.CO;2

Armstrong, R. L. (1982). Cordilleran metamorphic core complexes - From Arizona to southern Canada: Annual Review of Earth and Planetary Sciences, v. 10, p. 129–154.

Armstrong, R. L., & Ward, P. (1991). Evolving geographic patterns of Cenozoic magmatism in the North American Cordillera: The temporal and spatial association of magmatism and metamorphic core complexes: Journal of Geophysical Research, v. 96, p. 13,201–13,224. doi:10.1029/91JB00412

Barbarin, B. (1996). Genesis of the two main types of peraluminous granitoids. Geology, 24(4), 295-298. doi:10.1130/0091-7613(1996)024<0295:GOTTMT>2.3.CO;2

Barth, N. C., Hacker, B. R., Seward, G. G., Walsh, E. O., Young, D., & Johnston, S. (2010). Strain within the ultrahigh-pressure Western Gneiss region of Norway recorded by quartz CPOs. Geological Society, London, Special Publications, 335(1), 663–685.doi:10.1144/SP335.27

Behr, W. M., & Platt, J. P. (2011). A naturally constrained stress profile through the middle crust in an extensional terrane. Earth and Planetary Science Letters, 303(3–4), 181–192. doi:10.1016/j.epsl.2010.11.044

Bellemans, F., De Corte, F. & Van den haute, P. (1995). ‘Composition of SRM and CN U-doped glasses: Significance for their use as thermal neutron fluence monitors in fission track dating’, Radiation Measurements 24(2), 153–160. http://www.sciencedirect.com/science/article/pii/135044879400100F

Bryant, B., & Wooden, J. L. (1989). Lower-plate rocks of the Buckskin Mountains, Arizona: a progress report. Geology and mineral resources of the Buckskin and Rawhide Mountains, west-central Arizona: Arizona Geological Survey Bulletin, 198, 47–50. https://repository.arizona.edu/bitstream/handle/10150/630643/b-198-textreduced_buckskinrawhidemtns.pdf

Campbell-Stone, E., & John, B. E. (2002). Temporal changes in deformation mode: from failure to flow in the Colorado River extensional corridor. International Geology Review, 44(6), 512–527. doi:10.2747/0020-6814.44.6.512

Ceccato, A., Menegon, L., Pennacchioni, G., & Morales, L. F. G. (2018). Myrmekite and strain weakening in granitoid mylonites, Solid Earth, 9, 1399–1419. doi:10.5194/se-9-1399-2018

Chapman, J. B., Greig, R., & Haxel, G. B. (2020). Geochemical evidence for an orogenic plateau in the southern US and northern Mexican Cordillera during the Laramide orogeny. Geology, v. 48. doi.org/10.1130/G47117.1

Clarke, D. B (1981). The mineralogy of peraluminous granites; a review. The Canadian Mineralogist 19.1: 3–17. https://pubs.geoscienceworld.org/canmin/article-abstract/19/1/3/11498

Coney, P. J. (1974). Structural analysis of the Snake Range “décollement,” east-central Nevada: Geological Society of America Bulletin, v. 88, 1237–1250. doi:10.1130/0016-7606(1974)85<973:SAOTSR>2.0.CO;2

Coney, P. J., & Reynolds, S. J. (1977). Cordilleran benioff zones. Nature, 270(5636), 403. doi.org/10.1038/270403a0

Coney, P. J. (1980). Cordilleran metamorphic core complexes: An overview. Geological Society of America Memoirs, 153, 7–31. doi:10.1130/MEM153

Coney, P. J., & Harms, T. A. (1984). Cordilleran metamorphic core complexes: Cenozoic extensional relics of Mesozoic compression. Geology, 12, 550-554. doi:10.1130/0091-7613(1984)12<550:CMCCCE>2.0.CO;2

Crittenden, M. D., Coney, P. J., & Davis, G. H., editors (1980). Cordilleran metamorphic core complexes: Geological Society of America Memoir 153, 490 p.

Cross, A. J., Prior, D. J., Stipp, M., & Kidder, S. (2017). The recrystallized grain size piezometer for quartz: An EBSD-based calibration. Geophysical Research Letters, 44(13), 6667–6674. doi:10.1002/2017GL073836

Davis, G. H. (1980). Structural characteristics of metamorphic core complexes, southern Arizona. Geological Society of America Memoirs, 153, 35–78. doi:10.1130/MEM153

Davis, G. H., Gardulski, A. F., & Lister, G. S. (1987). Shear zone origin of quartzite mylonite and mylonitic pegmatite in the Coyote Mountains metamorphic core complex, Arizona. Journal of structural geology, 9(3), 289–297. doi:10.1016/0191-8141(87)90053-8

Davy, P., Guérin, G., & Brun, J. P. (1989). Thermal constraints on the tectonic evolution of a metamorphic core complex (Santa Catalina Mountains, Arizona). Earth and Planetary Science Letters, 94(3–4), 425–440. doi.org/10.1016/0012-821X(89)90159-3

Dickinson, W. R. (1989). Tectonic setting of Arizona through geologic time. In J. P. Jenney, S. J. Reynolds (Eds.), Geologic evolution of Arizona, Digest (Vol. 17, 1–16). Tucson, AZ: Arizona Geological Society. https://www.arizonageologicalsoc.org/resources/Documents/Publications/Digests/Digest_17/01_AGS_DIG17_Title_Table_of_Contents-S.pdf

Dickinson, W. R. (1991). Tectonic setting of faulted Tertiary strata associated with the Catalina core complex in southern Arizona. Special Papers (Vol. 264). Boulder, CO: Geological Society of America. doi:10.1130/SPE264

Dickinson, W. R. (2002). The Basin and Range Province as a composite extensional domain. International Geology Review, 44(1), 1-38, https://doi.org/10.2747/0020-6814.44.1.1

Di Vincenzo, G., Viti, C. & Rocchi, S. (2003). The effect of chlorite interlayering on 40 Ar–39 Ar biotite dating: an 40Ar–39Ar laser-probe and TEM investigations of variably chloritised biotites. Contributions to Mineralogy and Petrology, 145(6), 643–658. doi:10.1007/s00410-003-0472-z

Donelick, R. A., & Miller, D. S. (1991). Enhanced TINT fission track densities in low spontaneous track density apatites using 252Cf-derived fission fragment tracks: A model and experimental observations. International Journal of Radiation Applications and Instrumentation. Part D. Nuclear Tracks and Radiation Measurements, 18(3), 301–307. https://doi.org/10.1016/1359-0189(91)90022-A

Donelick, R. A., O'Sullivan, P. B., & Ketcham, R. A. (2005). Apatite fission-track analysis. Reviews in Mineralogy and Geochemistry, 58(1), 49–94. https://doi.org/10.2138/rmg.2005.58.3

Favorito, D. A., & Seedorff, E. (2018). Discovery of Major Basement-Cored Uplifts in the Northern Galiuro Mountains, Southeastern Arizona: Implications for Regional Laramide Deformation Style and Structural Evolution. Tectonics, 37(10), 3916–3940. doi.org/10.1029/2018TC005180

Fayon, A. K., Peacock, S. M., Stump, E., & Reynolds, S. J. (2000). Fission track analysis of the footwall of the Catalina detachment fault, Arizona: Tectonic denudation, magmatism, and erosion. Journal of Geophysical Research: Solid Earth, 105(B5), 11047–11062. doi:10.1029/1999JB900421

Fitz-Díaz, E., Lawton, T. F., Juárez-Arriaga, E., & Chávez-Cabello, G. (2018). The Cretaceous-Paleogene Mexican orogen: Structure, basin development, magmatism and tectonics. Earth-Science Reviews, 183, 56–84. doi.org/10.1016/j.earscirev.2017.03.002

Fitzgerald, P. G., Reynolds, S. J., Stump, E., Foster, D. A., & Gleadow, A. J. W. (1993). Thermochronologic evidence for timing of denudation and rate of crustal extension of the South Mountains metamorphic core complex and Sierra Estrella, Arizona. Nuclear Tracks and Radiation Measurements, 21(4), 555–563.

Fitz Gerald, J. D., & Stünitz, H. (1993). Deformation of granitoids at low metamorphic grade. I: Reactions and grain size reduction. Tectonophysics, 221(3–4), 269–297. doi:10.1016/0040-1951(93)90163-E

Fornash, K. F., Patchett, P. J., Gehrels, G. E., & Spencer, J. E., (2013), Evolution of granitoids in the Catalina metamorphic core complex, southeastern Arizona: U–Pb, Nd, and Hf isotopic constraints: Contributions to Mineral Petrology, 165, 1295–1310. doi: 10.1007/s00410-013-0859-4

Foster, D. A., Harrison, T. M., Miller, C. F., & Howard, K. A. (1990). The 40Ar/39Ar thermochronology of the eastern Mojave Desert, California, and adjacent western Arizona with implications for the evolution of metamorphic core complexes. Journal of Geophysical Research: Solid Earth, 95(B12), 20005–20024. doi:10.1029/JB095iB12p20005

Foster, D. A., Howard K. A., and John, B. E. (1991). Thermochronological constraints on the development of metamorphic core complexes in the lower Colorado River area, in Eighth International Conference on Geochronology, Cosmochronology, and Isotope Geology, edited by M. A. Lanphere, G. B. Dalrymple, and B. D. Turrin, U.S. Geol. Surv. Circ., 1107, 103 pp., 1994. https://pubs.usgs.gov/circ/1994/1107/report.pdf

Foster, D. A., & Spencer, J. E. (1992). Apatite and Zircon Fission, Track Dates from the Northern Plomosa Mountains, La Paz County, West-central Arizona. Arizona Geological Survey. http://repository.azgs.az.gov/uri_gin/azgs/dlio/311

Foster, D. A., & John, B. E. (1999). Quantifying tectonic exhumation in an extensional orogen with thermochronology: examples from the southern Basin and Range Province. Geological Society, London, Special Publications, 154(1), 343–364. https://doi.org/10.1144/GSL.SP.1999.154.01.16

Foster, D. A., Schafer, C., Fanning, C. M., & Hyndman, D. W. (2001). Relationships between crustal partial melting, plutonism, orogeny, and exhumation: Idaho-Bitterroot batholith: Tectonophysics, v. 342, 313–350. doi:10.1016/S0040-1951(01)00169-X

Gabber, L.J. (1991). On the Significance of Argon 40/Argon 39 Incremental Heating Of Biotite, Muscovite, And Amphibiole, The Ohio State University, PhD Thesis.

Gallagher, K. (2012). Transdimensional inverse thermal history modeling for quantitative thermochronology. Journal of Geophysical Research: Solid Earth, 117(B2). https://doi.org/10.1029/2011JB008825

Gans, P. B., & Bohrson, W. A. (1998). Suppression of volcanism during rapid extension in the Basin and Range Province, United States. Science, 279(5347), 66–68. doi:10.1126/science.279.5347.66

Gans, P. B., Mahood, G. A., & Schermer, E. (1989). Synextensional Magmatism in the Basin and Range Province: A Case Study from the Eastern Great Basin: Geological Society of America Special Paper 233, 53 p. doi:10.1130/SPE233

Gardulski, A. F. (1980). A structural and petrologic analysis of a quartzite--pegmatite tectonite, Coyote Mountains, southern Arizona.

https://repository.arizona.edu/bitstream/handle/10150/557464/AZU_TD_BOX297_E9791_1980_255.pdf?sequence=1

Gleadow, A. J. W., Duddy, I. R., Green, P. F., & Lovering, J. F. (1986). Confined fission track lengths in apatite: a diagnostic tool for thermal history analysis. Contributions to Mineralogy and Petrology, 94(4), 405–415. https://doi.org/10.1007/BF00376334

Gleadow, A. J., Belton, D. X., Kohn, B. P., & Brown, R. W. (2002). Fission track dating of phosphate minerals and the thermochronology of apatite. Reviews in mineralogy and geochemistry, 48(1), 579–630. https://doi.org/10.2138/rmg.2002.48.16

González-León, C. M., Solari, L., Valencia-Moreno, M., Rascon-Heimplel, M. A., Solé, J., González-Becuar, E., Lozano-Santacruz, R., & Pérez-Arvizu, O. (2016). Late Cretaceous to early Eocene magmatic evolution of the Laramide arc in the Nacozari quadrangle, northeastern Sonora, Mexico and its regional implications: Ore Geology Reviews, doi:10.1016/j.oregeorev.2016.07.020

Gottardi, R., & Teyssier, C., (2013). Thermomechanics of an extensional shear zone, Raft River metamorphic core complex, NW Utah. Journal of Structural Geology, 53, 54–69. doi.org/10.1016/j.jsg.2013.05.012

Gottardi, R., Schaper, M. C., Barnes, J. D., & Heizler, M. T. (2018). Fluid–Rock Interaction and Strain Localization in the Picacho Mountains Detachment Shear Zone, Arizona, USA. Tectonics, 37(9), 3244–3260. doi:10.1029/2017TC004835

Goodwin, L. B., & Haxel, G. B. (1990). Structural evolution of the Southern Baboquirari Mountains, south-central and north-central Sonora. Tectonics, 9(5), 1077–1095. doi:10.1029/TC009i005p01077

ten Grotenhuis, S. M., Trouw, R. A. J., & Passchier, C. W. (2003). Evolution of mica fish in mylonitic rocks. Tectonophysics, 372, 1–21. doi:10.1016/S0040-1951(03)00231-2

Grove, M. & Harrison, T. M. (1996). 40Ar* diffusion in Fe-rich biotite. American Mineralogist, 81(7–8), 940–951.

Hacker, B. R., Yin, A., Christie, J. M., & Davis, G. A. (1992). Stress magnitude, strain rate, and rheology of extended middle continental crust inferred from quartz grain sizes in the Whipple Mountains, California. Tectonics, 11(1), 36–46, https://doi.org/10.1029/91TC01291

Harrison, T. M., Célérier, J., Aikman, A. B., Hermann, J. & Heizler, M. T. (2009). Diffusion of 40Ar in muscovite. Geochimica et Cosmochimica Acta, 73(4), 1039–1051. doi.org/10.1016/j.gca.2008.09.038

Haugerud, R.A., & Kunk, M.J. (1988). ArAr*, a Computer Program for Reduction of 40Ar/39Ar Data: U.S. Geological Survey Open-File Report 88–261, 68 p. doi:10.3133/ofr88261

Haxel, G., May, D. J., Wright, I. E., & Tosdal, R.M. (1980a). Reconnaissance geologic map of the Baboquivari Peak quadrangle, Arizona. U.S. Geological Survey Miscellaneous Field Studies Map MF-1251, scale 1:62,500. doi:10.3133/mf1251

Haxel, G., Wright, I. E., May, D. J., & Tosdal, R. M. (1980b). Reconnaissance geology of the Mesozoic and lower Cenozoic rocks of the southern Papago Indian Reservation, Arizona: A preliminary report. Arizona Geological Society Digest, v. 12, 17–29. https://www.arizonageologicalsoc.org/resources/Documents/Publications/Digests/Digest_12/01_AGS_DIG12_Title%20Page_Table_of_Contents-S.pdf.

Haxel, G., Tosdal, R. M., May, D. J., & Wright, I.E. (1984). Latest Cretaceous and early Tertiary orogenesis in southcentral Arizona: thrust faulting, regional metamorphism, and granitic plutonism. Geological Society of America Bulletin, v. 95, 631–653. doi:10.1130/0016-7606(1984)95<631:LCAETO>2.0.CO;2

Hirth, G. & Tullis, J. (1992). Dislocation creep regimes in quartz aggregates. Journal of Structural Geology, 14(2), 145–159. doi:10.1016/0191-8141(92)90053-Y

Hirth, G., Teyssier, C., & Dunlap, J. W. (2001). An evaluation of quartzite flow laws based on comparisons between experimentally and naturally deformed rocks. International Journal of Earth Sciences 90, no. 1, 77–87. doi:10.1007/s005310000152

Howard, K. A., and Foster, D. A. (1996). Thermal and unroofing history of a thick, tilted Basin-and-Range crustal section in the Tortilla Mountai ns, Arizona, Journal of Geophysical Research, 101, 511–522, 1996. . https://doi.org/10.1029/95JB02909

Jepson, G., and Carrapa, B., (2019), Thermochronological and Geochemical Insights on the transition between the Metamorphic Core Complex and the North American Cordillera, Southern Arizona. GSA Annual Meeting in Phoenix, Arizona, USA. GSA.

John, B. E., & Foster, D. A. (1993). Structural and thermal constraints on the initiation angle of detachment faulting in the southern Basin and Range: The Chemehuevi Mountains case study. Geological Society of America Bulletin, 105(8), 1091–1108. https://doi.org/10.1130/0016-7606(1993)105<1091:SATCOT>2.3.CO;2

Keith, S. B., Reynolds, S. J., Damon, P. E., Shafiqullah, M., Livingston, D. E., & Pushkar, P. D. (1980). Evidence for multiple intrusion and deformation within the Santa Catalina-Rincon-Tortolita crystalline complex, southeastern Arizona. In M. S. Crittenden Jr., P. J. Coney, G. H. Davis, (Eds.), Cordilleran metamorphic core complexes, Memoir (Vol. 153, 217–267). Boulder, CO: Geological Society of America. doi:10.1130/MEM153-p217.

Kelley, S. (2002). Excess argon in K–Ar and Ar–Ar geochronology. Chemical Geology, 188(1–2), 1–22. doi:10.1016/S0009-2541(02)00064-5

Ketcham, R. A., Carter, A., Donelick, R. A., Barbarand, J., & Hurford, A. J. (2007). Improved modeling of fission-track annealing in apatite. American Mineralogist, 92(5–6), 799–810. https://doi.org/10.2138/am.2007.2281

Krantz, R. W., Jenney, J. P., & Reynolds, S. J. (1989). Laramide structures of Arizona. Geologic Evolution of Arizona: Arizona Geological Society Digest, 17, 463–483.

Kuiper, K. F., Deino, A., Hilgen, F. J., Krijgsman, W., Renne, P. R., & Wijbrans, A. J. (2008). Synchronizing rock clocks of Earth history. Science, 320(5875), 500–504. doi: 10.1126/science.1154339.

Laslett, G. M., Kendall, W. S., Gleadow, A. J. W., & Duddy, I. R. (1982). Bias in measurement of fission-track length distributions. Nuclear Tracks and Radiation Measurements (1982), 6(2–3), 79-85. https://doi.org/10.1016/0735-245X(82)90031-X

Lee, J. Y., Marti, K., Severinghaus, J. P., Kawamura, K., Yoo, H. S., Lee, J. B., & Kim, J. S. (2006). A redetermination of the isotopic abundances of atmospheric Ar. Geochimica et Cosmochimica Acta, 70(17), 4507–4512. doi:10.1016/j.gca.2006.06.1563

Lister, G. S. (1977). Discussion: crossed-girdle c-axis fabrics in quartzites plastically deformed by plane strain and progressive simple shear. Tectonophysics, 39(1–3), 51–54. doi10.1016/0040-1951(77)90087-7

Lister, G. S., & Baldwin, S. L. (1993). Plutonism and the origin of metamorphic core complexes: Geology, v. 21, 607–610. doi:10.1130/0091-7613(1993)021<0607:PATOOM>2.3.CO;2

Lister, G. S., & Davis, G. A. (1989). The origin of metamorphic core complexes and detachment faults formed during Tertiary continental extension in the northern Colorado River region, USA. Journal of Structural Geology, 11(1–2), 65–94. doi:10.1016/0191-8141(89)90036-9

Lo, C-H, & Onstott, T. C. (1989). 39Ar recoil artifacts in chloritized biotite. Geochimica et Cosmochimica Acta, 53(10), 2697–2711. doi:10.1016/0016-7037(89)90141-5

Long, S. P., & Soignard, E. (2016). Shallow-crustal metamorphism during Late Cretaceous anatexis in the Sevier hinterland plateau: Peak temperature conditions from the Grant Range, eastern Nevada, USA. Lithosphere, 8(2), 150–164.

Long, K. B., Gehrels, G. E., & Baldwin, S. L. (1995). Tectonothermal evolution of the Pinaleno-Jackson Mountain core complex, southeast Arizona. Geological Society of America Bulletin, 107(10), 1231–1240. doi:10.1130/0016-7606(1995)107<1231:TEOTPO>2.3.CO;2

Long, S. P., Heizler, M. T., Thomson, S. N., Reiners, P. W., & Fryxell, J. E. (2018). Rapid Oligocene to early Miocene extension along the Grant Range detachment system, Nevada, USA: Insights from multipart cooling histories of footwall rocks. Tectonics, 37(12), 4752-4779.

Ludwig, K. R. (2012). User´s Manual for ISOPLOT 3.75: A Geochronological Toolkit for Microsoft Excel. Berkeley, Berkeley Geochronology Center, Special Publication No. 5, 75 p.

McAleer, R. J., Bish, D. L., Kunk, M. J., Sicard, K. R., Valley, P. M., Walsh, G. J., Wathen, B. A., & Wintsch, R. P. (2017). Reaction softening by dissolution–precipitation creep in a retrograde greenschist facies ductile shear zone, New Hampshire, USA. Journal of Metamorphic Geology, 35(1), 95–119. doi:10.1111/jmg.12222

McQuarrie, N., & Wernicke, B. P. (2005). An animated tectonic reconstruction of southwestern north America since 36 Ma, Geosphere, 1, 147–172, doi:10.1130/GES00016.1.

McQuarrie, N., & Oskin, M. (2010). Palinspastic restoration of NAVDat and implications for the origin of magmatism in southwestern North America. Journal of Geophysical Research: Solid Earth, 115(B10), https://doi.org/10.1029/2009JB006435.

Miller, E. L., & Gans, P. B. (1989). Cretaceous crustal structure and metamorphism in the hinterland of the Sevier thrust belt, western US Cordillera. Geology, 17(1), 59–62.

Miller, C. F., McDowell, S. M., & Mapes, R. W. (2003). Hot and cold granites? Implications of zircon saturation temperatures and preservation of inheritance. Geology, 31(6), 529-532. https://doi.org/10.1130/0091-7613(2003)031%3C0529:HACGIO%3E2.0.CO;2

Min, K., Mundil, R., Renne, P. R., & Ludwig, K. R. (2000). A test for systematic errors in 40Ar/39Ar geochronology through comparison with U/Pb analysis of a 1.1-Ga rhyolite. Geochimica et Cosmochimica Acta, 64(1), 73–98. doi:10.1016/S0016-7037(99)00204-5

Passchier, C. W., & Trouw, R. A. J, (2005) Microtectonics, Springer-Verlag Berlin Heidelberg, doi:10.1007/978-3-662-08734-3, ISBN: 978-3-662-08734-3

Paton, C., Woodhead, J. D., Hellstrom, J. C., Hergt, J. M., Greig, A., & Maas, R. (2010). Improved laser ablation U-Pb zircon geochronology through robust downhole fractionation correction. Geochemistry, Geophysics, Geosystems, 11, QOAA06. doi: 10.1029/2009GC002618

Petrus, J. A., & Kamber, B. S. (2012). VizualAge: a novel approach to laser ablation ICP-MS U-Pb geochronology data reduction. Geostand. Geoanal. Res. 36, 247–270. doi:10.1111/j.1751-908X.2012.00158.x

Platt, J. P., Behr, W. M., & Cooper, F. J. (2015). Metamorphic core complexes: windows into the mechanics and rheology of the crust. Journal of the Geological Society, 172(1), 9–27. doi:10.1144/jgs2014-036

Putirka, K., & Platt, B. (2012). Basin and Range volcanism as a passive response to extensional tectonics. Geosphere, 8(6), 1274–1285, https://doi.org/10.1130/GES00803.1

Pryer, L. L. (1993). Microstructures in feldspars from a major crustal thrust zone: the Grenville Front, Ontario, Canada. Journal of structural Geology, 15(1), 21–36. doi:10.1016/0191-8141(93)90076-M.

Rehrig, W. A., & Reynolds, S. J. (1980). Geologic and geochronologic reconnaissance of a northwest-trending zone of metamorphic core complexes in southern and western Arizona. Memoir of the Geological Society of America, 153, 131–157. doi:10.1130/MEM153-p131

Rey, P., Vanderhaeghe, O., & Teyssier, C. (2001). Gravitational collapse of the continental crust: definition, regimes and modes. Tectonophysics, 342(3–4), 435–449. doi:10.1016/S0040-1951(01)00174-3

Reynolds, S. J. (1985). Geology of the South Mountains, central Arizona, Bulletin (Vol. 195). Tucson, AZ: Arizona Bureau of Geology and Mineral Technology, http://repository.azgs.az.gov/uri_gin/azgs/dlio/1655.

Richard, S. M., Fryxell, J. E., & Sutter, J. F. (1990). Tertiary structure and thermal history of the Harquahala and Buckskin Mountains, west central Arizona: Implications for denudation by a major detachment fault system. Journal of Geophysical Research: Solid Earth, 95(B12), 19973–19987. doi:10.1029/JB095iB12p19973

Roberts, H. J., Kelley, S. P., & Dahl, P. S. (2001). Obtaining geologically meaningful 40Ar–39Ar ages from altered biotite. Chemical Geology, 172(3–4), 277–290. doi:10.1016/S0009-2541(00)00255-2

Rutter, E. H., & Brodie, K. H. (2004). Experimental grain size-sensitive flow of hot-pressed Brazilian quartz aggregates. Journal of Structural Geology, 26(11), 2011–2023, doi:10.1016/j.jsg.2004.04.006

Ruffet, G., Féraud, G., & Amouric, M. (1991). Comparison of 40Ar-39Ar conventional and laser dating of biotites from the North Trégor Batholith. Geochimica et Cosmochimica Acta, 55(6), 1675–1688. doi:10.1016/0016-7037(91)90138-U

Schmid, S. M., & Casey, M. (1986). Complete fabric analysis of some commonly observed quartz c-axis patterns. Geophysical Monograph, 36, 263–286.

Scott, R. J., Foster, D. A., and Lister, G., S. (1998). "Tectonic implications of rapid cooling of lower plate rocks from the Buckskin-Rawhide metamorphic core complex, west-central Arizona." Geological Society of America Bulletin 110.5 (1998): 588–614. https://doi.org/10.1130/0016-7606(1998)110<0588:TIORCO>2.3.CO;2

Simpson, C., & Wintsch, R. P. (1989). Evidence for deformation-induced K-feldspar replacement by myrmekite. Journal of Metamorphic Geology, 7(2), 261–275. doi:10.1111/j.1525-1314.1989.tb00588.x

Singleton, J. S., & Mosher, S. (2012). Mylonitization in the lower plate of the Buckskin-Rawhide detachment fault, west-central Arizona: Implications for the geometric evolution of metamorphic core complexes. Journal of Structural Geology, 39, 180–198. doi:10.1016/j.jsg.2012.02.013

Singleton, J. S., & Wong, M. S. (2016). Polyphase mylonitization in the Harcuvar and Buckskin-Rawhide metamorphic core complexes, west-central Arizona. In Geological Society of America Abstracts with Programs (Vol. 48, No. 4). doi: 10.1130/abs/2016CD-274076

Singleton, J. S., Stockli, D. F., Gans, P. B., & Prior, M. G. (2014). Timing, rate, and magnitude of slip on the Buckskin-Rawhide detachment fault, west central Arizona. Tectonics, 33(8), 1596–1615. doi:10.1002/2013TC003517

Singleton, J. S., Wong, M. S., & Johnston, S. M. (2018). The role of calcite-rich metasedimentary mylonites in localizing detachment fault strain and influencing the structural evolution of the Buckskin-Rawhide metamorphic core complex, west-central Arizona. Lithosphere, 10(2), 172–193. doi:10.1130/L699.1

Sláma, J., Koŝler, J., Condon, D. J., Crowley, J. L., Gerdes, A., Hanchar, J. M., Horstwood, M. S. A., Morris, G. A., Nasdala, L., Norberg, N., Schaltegger, U., Schoene, B., Tubrett, M. N., & Whitehouse, M. J. (2008). Pleŝovice zircon — A new natural reference material for U–Pb and Hf isotopic microanalysis: Chemical Geology 249, 1−35. doi.org/10.1016/j.chemgeo.2007.11.005

Sloss, L. L. (1988). Tectonic evolution of the craton in Phanerozoic time. The Geology of North America, 2, 25–51. doi:10.1130/DNAG-GNA-D2.25

Solari, L.A., Gómez-Tuena, A., Bernal, J.P., Pérez-Arvizu, O., & Tanner, M. (2010). U-Pb zircon geochronology by an integrated LA-ICPMS microanalytical workstation: achievements in precision and accuracy: Geostandards and Geoanalytical Research, 34(1), 5−18.

Spencer, J. E., & Reynolds, S. J. (1989). Middle Tertiary tectonics of Arizona and adjacent areas. Geologic evolution of Arizona: Arizona Geological Society Digest, 17, 539-574.

Spencer, J. E., & Reynolds, S. J. (1990). Relationship between Mesozoic and Cenozoic tectonic features in west central Arizona and adjacent southeastern California. Journal of Geophysical Research: Solid Earth, 95(B1), 539–555. https://doi.org/10.1029/JB095iB01p00539

Spencer, J.E., Richard, S.M., Reynolds, S.J., Miller, R.J., Shafiqullah, M., Gilbert, W.G., & Grubensky, M.J. (1995). Spatial and temporal relationships between mid- Tertiary magmatism and extension in southwestern Arizona: Journal of Geophysical Research, 100, 10,321–10,351. doi:10.1029/94JB02817

Spencer, J. E., Richard, S. M., Lingrey, S. H., Johnson, B. J., Johnson, R. A., & Gehrels, G. E. (2019). Reconstruction of mid-Cenozoic extension in the Rincon Mountains area, southeastern Arizona, USA, and geodynamic implications. Tectonics, 38, 2338– 2357. doi:10.1029/2019TC005565

Staudacher, T., Jessberger, E., Dorflinger, D., Kiko, J. (1978). A refined ultrahigh-vacuum 103 furnace for rare gas analysis. Journal of Physics E: Scientific Instruments 11, 781. doi:10.1088/0022-3735/11/8/019

Stipp, M., Stunitz, H., Heilbronner, R., & Schmid, S. M. (2002a). The eastern Tonale fault zone: a ‘natural laboratory’ for crystal plastic deformation of quartz over a temperature range from 250 to 700 C. Journal of structural geology, 24(12), 1861–1884. doi:10.1016/S0191-8141(02)00035-4.

Stipp, M., Stünitz, H., Heilbronner, R., & Schmid, S. M. (2002b). Dynamic recrystallization of quartz: correlation between natural and experimental conditions. Geological Society, London, Special Publications, 200(1), 171–190. doi:10.1144/GSL.SP.2001.200.01.11

Stünitz, H., & Fitz Gerald, J. D. (1993). Deformation of granitoids at low metamorphic grade. II: Granular flow in albite-rich mylonites. Tectonophysics, 221(3–4), 299–324. doi:10.1016/0040-1951(93)90164-F

Sylvester, P. J. (1998). Post-collisional strongly peraluminous granites. Lithos, 45(1–4), 29–44. doi:10.1016/S0024-4937(98)00024-3

Tagami, T. (1987). Determination of zeta calibration constant for fission track dating, International Journal of Radiation Applications and Instrumentation. Part D. Nuclear Tracks and Radiation Measurements 13(2), 127–130. doi.org/10.1016/1359-0189(87)90023-9

Tagami, T., & O'Sullivan, P. B. (2005). Fundamentals of fission-track thermochronology. Reviews in Mineralogy and Geochemistry, 58(1), 19–47. https://doi.org/10.2138/rmg.2005.58.2

Teyssier, C., & Whitney, D. L. (2002). Gneiss domes and orogeny. Geology, 30, 1139–1142. doi:10.1130/0091-7613(2002)030<1139:GDAO>2.0.CO;2

Teyssier, C., Ferre, E., Whitney, D. L., Norlander, B., Vanderhaeghe, O., & Parkinson, D. (2005). Flow of partially molten crust and origin of detachments during collapse of the Cordilleran orogen, Geol. Soc. Spec. Publ., 245, 39–64. doi:10.1144/GSL.SP.2005.245.01.03

Töheide, K (1972). Water at high temperature and pressure. In: Franks, F. (Ed), Water: a comprehensive treatise. Pp 463–514.

Tokle, L., Hirth, G., & Behr, W. M. (2019). Flow laws and fabric transitions in wet quartzite. Earth and Planetary Science Letters, 505, 152–161. doi:10.1016/j.epsl.2018.10.017

Turpin, L., Cuney, M., Friedrich, M., Bouchez, J. L., & Aubertin, M. (1990). Meta-igneous origin of Hercynian peraluminous granites in NW French Massif Central: implications for crustal history reconstructions. Contributions to Mineralogy and Petrology, 104(2), 163–172. doi:10.1007/BF00306440

Tuttle, O. F., & Bowen, N. L. (1958). Origin of Granite in the Light of Experimental Studies in the System: NaAlSi3O8 (No. 74). Geological Society of America.

Vanderhaeghe, O., Teyssier, C., McDougall, I., & Dunlap, W. J. (2003). Cooling and exhumation of the Shuswap Metamorphic Core Complex constrained by ^{40}Ar/^{39}Ar thermochronology. Geological Society of America Bulletin, 115(2), 200–216. doi:10.1130/0016-7606(2003)115<0200:CAEOTS>2.0.CO;2

Vernon, R. H. (1999). Review of Microstructural Evidence of Magmatic and Solid-State Flow, Visual Geosciences, 5, 1–23. doi:10.1007/s10069-000-0002-3

Vernon, R. H. (2018). A practical guide to rock microstructure. Cambridge university press, ISBN:1108684769, 9781108684767.

Whitney, D., Teyssier, C., Rey, P., & Buck, W. R. (2013). Oceanic and continental core complexes. Geological Society of America Bulletin. 125(3–4); 273–298. doi:10.1130/B30754.1

Wiedenbeck, M., Allé, P., Corfu, F., Griffin, W.L., Meier, M., Oberli, F., Von Quadt, A., Roddick, J.C., & Speigel, W. (1995). Three natural zircon standards for U–Th–Pb, Lu–Hf, trace-element and REE analyses. Geostandards Newsletter 19, 1–23.

Wong, M. S., & Gans, P. B. (2008). Geologic, structural, and thermochronologic constraints on the tectonic evolution of the Sierra Mazatán core complex, Sonora, Mexico: New insights into metamorphic core complex formation. Tectonics, 27(4). doi:10.1029/2007TC002173

Wong, M. S., Gans, P. B., & Scheier, J. (2010). The 40Ar/39Ar thermochronology of core complexes and other basement rocks in Sonora, Mexico: Implications for Cenozoic tectonic evolution of northwestern Mexico. Journal of Geophysical Research: Solid Earth, 115(B7). https://doi.org/10.1029/2009JB007032

Wright, J. E., Haxel, Gordon, & May, D. J. (1981). Early Jurassic uranium-lead isotopic ages for Mesozoic supracrustal sequences, Papago Indian Reservation, southern Arizona [abs.]: Geological Society of America Abstracts with Programs, 13, 115.

Wright, J. E., & Haxel, G. (1982). A garnet-two-mica granite, Coyote Mountains, southern Arizona: Geologic setting, uranium-lead isotopic systematics of zircon, and nature of the granite source region. Geological Society of America Bulletin, 93(11), 1176–1188. doi:10.1130/0016-7606(1982)93<1176:AGGCMS>2.0.CO;2

FIGURE CAPTIONS

Figure 1: Schematic map of the three belts of metamorphic core complex in the North American Cordillera, and the location of the Baboquivari Mountains (red) (adapted from Coney, 1980; Whitney et al., 2013).

Figure 2: Schematic map of the southern belt of metamorphic core complexes that extends from the Colorado extensional corridor down to Mexico (modified from Spencer et al., 2019). Direction of displacement of the hanging wall indicated by green arrows; ages of mylonitization, estimated from argon $^{40}Ar/^{39}Ar$ (green boxes) or potassium argon (K/Ar) (brown boxes), on hornblende (Hb), biotite (Bt), or muscovite (Ms) reported next to the metamorphic core complexes. Source for the geochronological data include the following: (1) Foster et al. (1990); (2) Hacker et al. (1992); (3) Scott et al. (1998) and Singleton and Wong (2016); (4) Richard et al. (1990); (5) Rehrig and Reynolds (1980); (6) Fitzgerald et al. (1993); (7) Gottardi et al. (2018); (8) Long et al. (1995); (9) Fayon et al. (2000); (10) Wong et al. (2010); (11) Wong and Gans (2008).

Figure 3: (Left) Geologic map of the Baboquivari Mountains, showing the location of the Laramide Baboquivari thrust and Coyote Mountain Metamorphic core complex (adapted from Haxel et al., 1984). (Right) Geologic map of the Coyote Mountain metamorphic core complex; modified from Gardulski (1980) and Wright and Haxel (1982). Cross section AA' indicate the location of the collected samples (modified from Davis et al., 1987).

Figure 4: Cross-polarized thin section photomicrographs of representative microstructures of the Coyote Mountain detachment shear zone (A) protomylonite, (B-D) mylonite. Thin sections cut perpendicular to foliation and parallel to lineation, the photomicrographs are taken oriented top to the North.

Figure 5: Cross-polarized thin section photomicrographs of representative quartz microstructures. Bands of fine quartz grains recrystallized dominantly by subgrain rotation (A-B) and and grain boundary migration (C-D). Quartz forms stretched and deformed ribbons commonly wrapped around rigid feldspar porphyroclasts (A-B). (E) Larger quartz grains and ribbons commonly display banded undulose extinction. (F) Quartz grains are often cross-cut by fluid inclusions bands that cross multiple grains (white arrows). Thin sections cut perpendicular to foliation and parallel to lineation, the photomicrographs are taken oriented top to the North (North to the right).

Figure 6: Cross-polarized thin section photomicrographs of representative feldspar microstructures. (A-B) fracturing of feldspar grains along cleavage planes at high angle to foliation, recording top-to-the-north kinematic shear sense. (C) Flame perthite oriented subparallel to the mylonitic foliation. (D) Bent twins in plagioclase. (F) Tartan twinning. (E) Myrmekites oriented subparallel to the mylonitic foliation. (F) Subordinate subgrain rotation recrystallization of feldspar grains (white arrows). Thin sections cut perpendicular to foliation and parallel to lineation, the photomicrographs are taken oriented top to the North (North to the right).

Figure 7: Cross-polarized thin section photomicrographs of representative biotite and muscovite microstructures. (A) Biotite grains preserve a rhombohedral shape. (B-F) Coarse-grained muscovite shows evidence of intracrystalline deformation such as kink folding (B-C), micro-boudinage (D), and bent folia (E-F). Thin sections cut perpendicular to foliation and parallel to lineation, the photomicrographs are taken oriented top to the North (North to the right).

Figure 8: Quartz crystallographic preferred orientation measured by Electron Backscattered Diffraction. Quartz c- and a-axis pole figures show that slip systems active during quartz recrystallization included basal ⟨a⟩, rhomb ⟨a⟩, and/or prism ⟨a⟩ slip. C-axis pole figures show dextral asymmetry compatible with a

top-to-the-north sense of shear, suggesting that the detachment shear zone experience a non-coaxial constrictional component of deformation.

Figure 9: Tera–Wasserburg concordia diagram (A) and weighted mean age plot (B) for two-mica granite sample CM14-04. The most concordant U-Pb zircon analyses, used for the $^{206}Pb/^{238}U$ age calculation (n = 15), are shown as black-line error ellipses with black squares in the concordia diagram (A) and as gray bars in weighted mean age plot (B). C) SEM-Cathodoluminiscence images of representative dated zircons from the granite sample; yellow semicircles and the adjacent numbers represent the spot size (~23μm) and the spot number, respectively. The $^{206}Pb/^{238}U$ ages are reported in Ma at the 2-sigma level of precision. Zircon spots marked as “bad data” in the cathodoluminescence image represent laser ablation analyses that sampled different proportions of zircon material combined with other unintended mineral phases (e.g., inclusions of apatite, oxides, etc.) that make the U-Pb geochronology effort ineffective due to large uncertainties in the isotopic ratios.

Figure 10: $^{40}Ar/^{39}Ar$ Ms-Bt age spectra pairs for 11 samples from the Coyote Mountains. Replicate analyses from samples CM16-06 and CM16-10A are also plotted. See Figure 3 for sample locations. *M = mylonite, P = protomylonite.

Figure 11: Geochronological total gas ages plotted on the AA’ transect across the Coyote Mountain detachment shear zone (see Figure 3 for AA’ location). There is little variance in muscovite age across the transect. Biotite ages vary widely but show no correlation with elevation.

Figure 12: Combined thermal history model for samples CP-01 and CP-02. The blue and red lines are the expected models, grey envelopes are the 95% confidence interval for the expected model. APAZ is the apatite partial annealing zone. The model predicts monotonic cooling between the zircon U-Pb age (58 Ma) and the muscovite Ar-Ar age (29 Ma), followed be extremely rapid cooling between 29 and 24 Ma.

Figure 13: Strength profile using the Hirth et al. (2001) and Rutter and Brodie (2004) quartzite dislocation creep flow law for the lower crust. Vertical axis is temperature; hot geotherms of 35°C/km and 45°C/km are used to convert temperature to depth, suggesting that the detachment shear zone evolved at a depth ranging from 11 to 14 km.

Figure 14: Cooling history of 8 metamorphic core complexes (see Figure 2 for location). Given the uncertainties in closure temperature, we plot a closure temperature of 750 ± 50ºC for zircon U-Pb, 500 ± 25ºC for hornblende $^{40}Ar/^{39}Ar$, 425 ± 25ºC for muscovite Rb-Sr, 400 ± 50ºC for muscovite $^{40}Ar/^{39}Ar$ and K-Ar, 300 ± 50ºC for biotite $^{40}Ar/^{39}Ar$ and K-Ar, 275 ± 40ºC for biotite K-Ar, 240 ± 10ºC for zircon fission track, 180 ± 10ºC for zircon U-Th/He, 100 ± 10ºC for apatite fission track, 60 ± 10ºC for apatite U-Th/He. Data extracted from John and Foster (1993), and Foster and John (1999) (Chemehuevi); Foster and Spencer (1992) (Plomosa); Hacker et al. (1992) and reference therein (Whipple), Scott et al. (1998) and Singleton et al. (2014) (Buckskin); Fitzgerald et al. (1993) (South Mountain); Gottardi et al. (2018) (Picacho); Davy et al. (1989), Fayon et al. (2000), Fornash at al. (2013), Jepson and Carrapa (2019) for the Catalina; Wong and Gans (2008) for the Sierra Mazatan. The cooling curves suggests that eastern MCCs were denuded/exhumed earlier (during the Oligocene, between ~29 and 23 Ma) than the western MCCs of the Colorado River Extensional Corridor (Miocene, between ~22 and 15 Ma).

Figure 15: (A) Tectonic setting of the Baboquivari Mountains during the Laramide orogeny (~60 Ma), which provided (1) increased potential energy by uplift and thickening, (2) mechanical weakening by thrusting leading to the development of weak zones and assimilation of metasediments, and (3) thermal weakening associated with intrusive activity (adapted from Haxel et al., 1984). Combined with change in boundary conditions, these processes likely triggered orogenic collapse by Oligocene time (B) and lead to the development of the Coyote Mountains detachment shear zone and exhumation of the Baboquivari Mountains.

Figure 1.

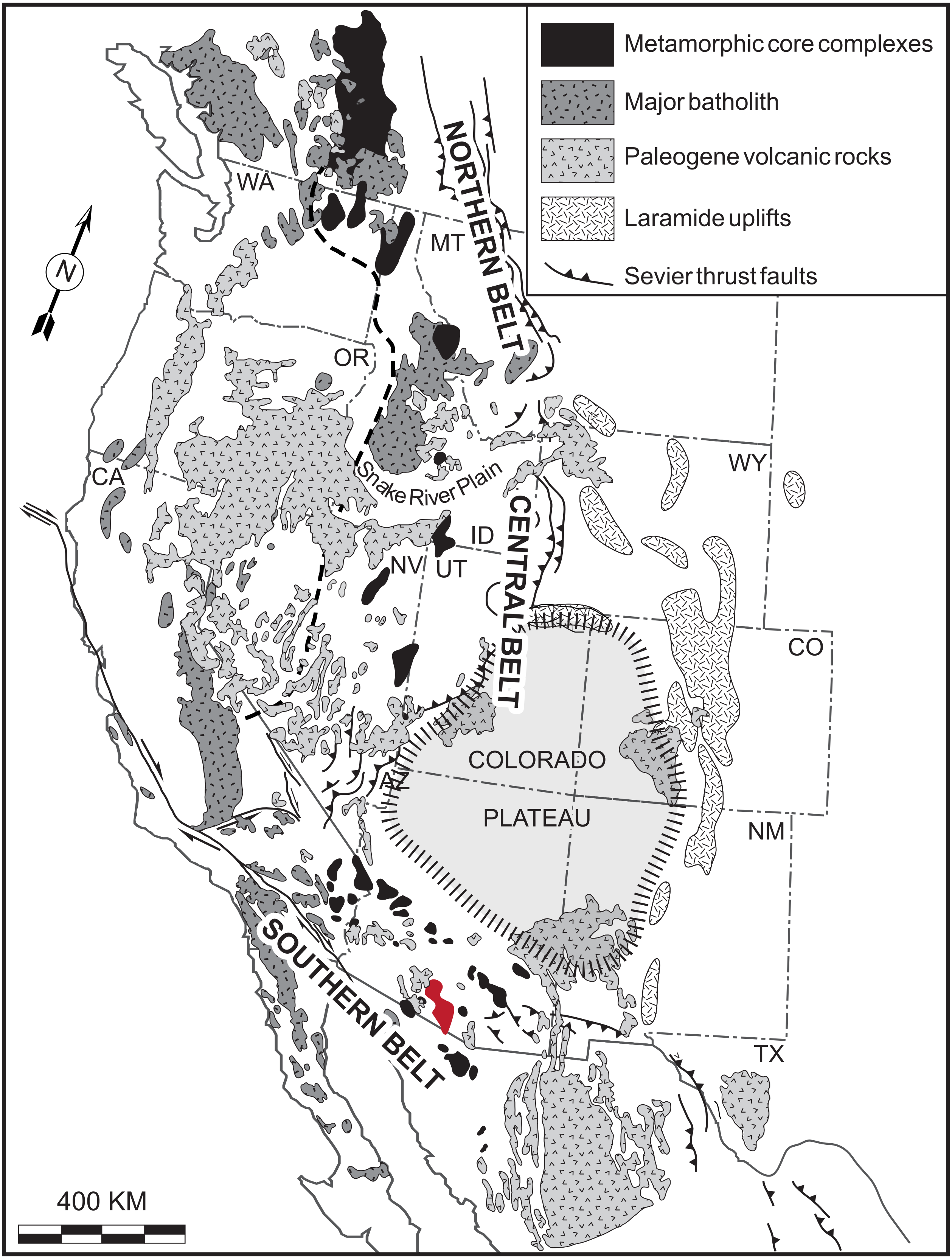

Metamorphic core complexes
Major batholith
Paleogene volcanic rocks
Laramide uplifts
Sevier thrust faults
NORTHERN BELT
CENTRAL BELT
SOUTHERN BELT
WA
MT
OR
ID
CA
NV
UT
WY
CO
AZ
NM
TX
Snake River Plain
COLORADO
PLATEAU
N
400 KM

Figure 2.

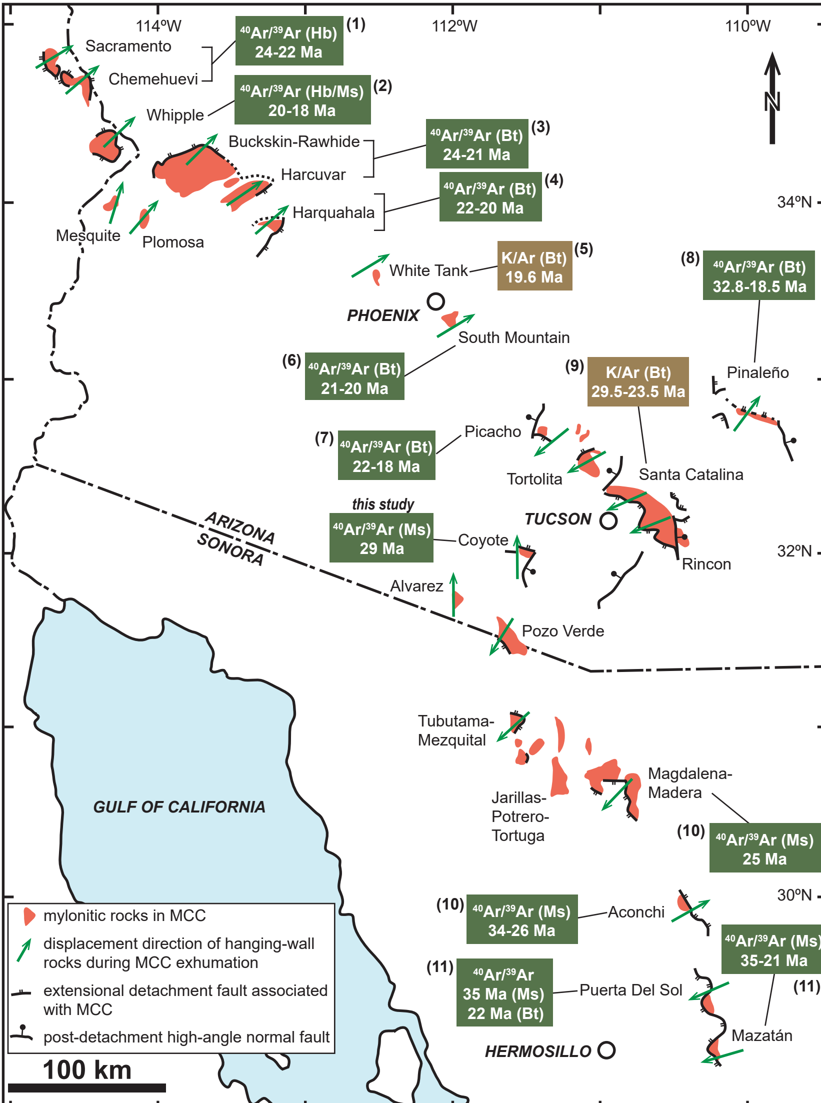

114ºW
112ºW
110ºW
34ºN
32ºN
30ºN
N
Sacramento
Chemehuevi
(1)
^{40}Ar/^{39}Ar (Hb)
24-22 Ma
Whipple
(2)
^{40}Ar/^{39}Ar (Hb/Ms)
20-18 Ma
Buckskin-Rawhide
Harcuvar
(3)
^{40}Ar/^{39}Ar (Bt)
24-21 Ma
(4)
^{40}Ar/^{39}Ar (Bt)
22-20 Ma
Harquahala
Mesquite
Plomosa
White Tank
(5)
K/Ar (Bt)
19.6 Ma
(8)
^{40}Ar/^{39}Ar (Bt)
32.8-18.5 Ma
PHOENIX
South Mountain
(6)
^{40}Ar/^{39}Ar (Bt)
21-20 Ma
(9)
K/Ar (Bt)
29.5-23.5 Ma
Pinaleño
Picacho
(7)
^{40}Ar/^{39}Ar (Bt)
22-18 Ma
Tortolita
Santa Catalina
this study
^{40}Ar/^{39}Ar (Ms)
29 Ma
Coyote
TUCSON
Rincon
ARIZONA
SONORA
Alvarez
Pozo Verde
Tubutama-
Mezquital
Jarillas-
Potrero-
Tortuga
Magdalena-
Madera
(10)
^{40}Ar/^{39}Ar (Ms)
25 Ma
GULF OF CALIFORNIA
(10)
^{40}Ar/^{39}Ar (Ms)
34-26 Ma
Aconchi
^{40}Ar/^{39}Ar (Ms)
35-21 Ma
(11)
^{40}Ar/^{39}Ar
35 Ma (Ms)
22 Ma (Bt)
Puerta Del Sol
(11)
Mazatán
HERMOSILLO
mylonitic rocks in MCC
displacement direction of hanging-wall rocks during MCC exhumation
extensional detachment fault associated with MCC
post-detachment high-angle normal fault
100 km

Figure 3.

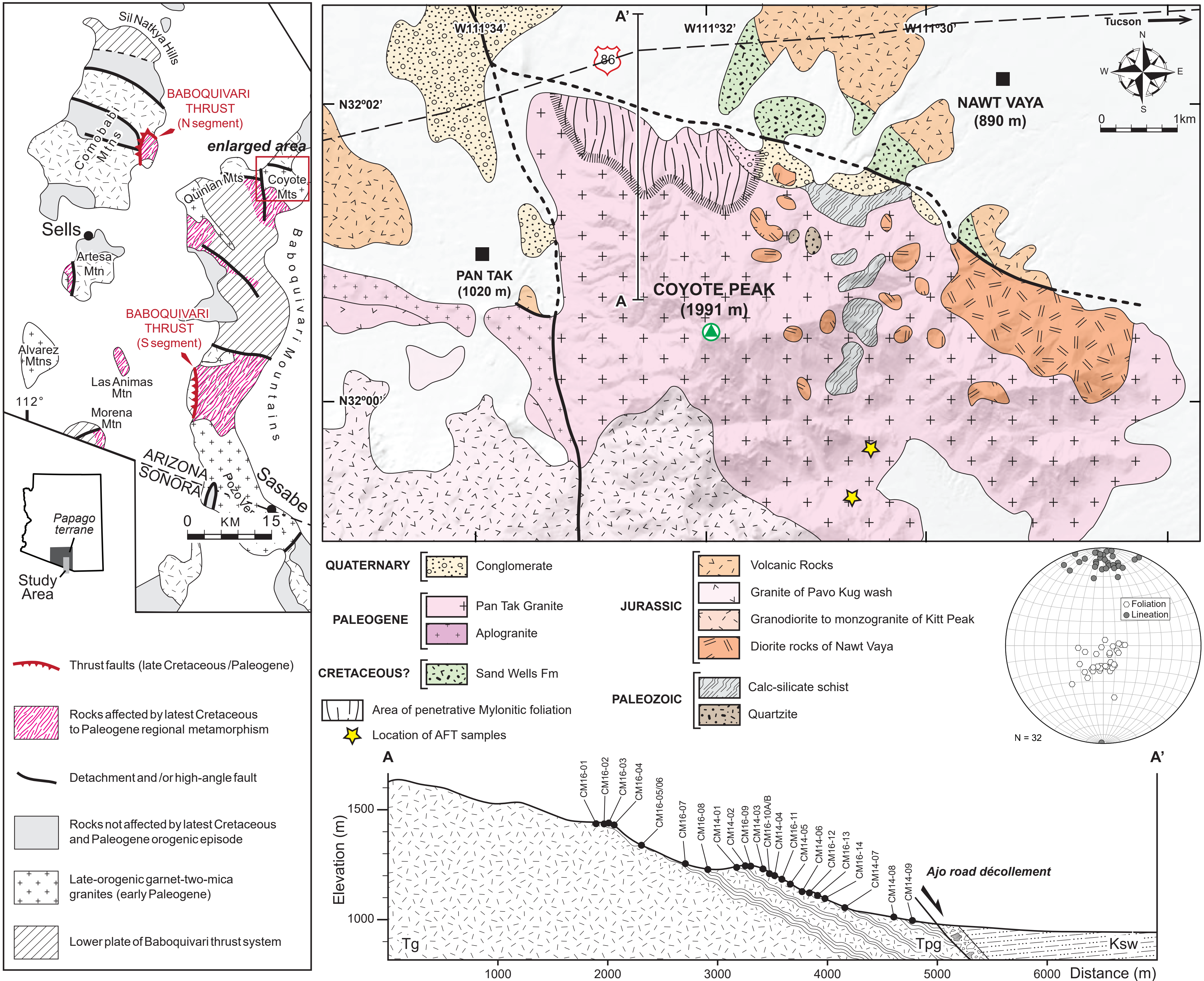

Sil Natkya Hills
BABOQUIVARI THRUST (N segment)
Comobabi Mtns
enlarged area
Quinlan Mts
Coyote Mts
Sells
Artesa Mtn
Baboquivari Mountains
BABOQUIVARI THRUST (S segment)
Alvarez Mtns
Las Animas Mtn
112°
Morena Mtn
ARIZONA
SONORA
Pozo Verde
Sasabe
0 KM 15
Papago terrane
Study Area
Thrust faults (late Cretaceous/Paleogene)
Rocks affected by latest Cretaceous to Paleogene regional metamorphism
Detachment and/or high-angle fault
Rocks not affected by latest Cretaceous and Paleogene orogenic episode
Late-orogenic garnet-two-mica granites (early Paleogene)
Lower plate of Baboquivari thrust system
A'
W111°34'
W111°32'
W111°30'
Tucson
86
N32°02'
N32°00'
N
W
E
S
0 1km
NAWT VAYA (890 m)
PAN TAK (1020 m)
A
COYOTE PEAK (1991 m)
QUATERNARY
Conglomerate
PALEOGENE
Pan Tak Granite
Aplogranite
CRETACEOUS?
Sand Wells Fm
Area of penetrative Mylonitic foliation
Location of AFT samples
JURASSIC
Volcanic Rocks
Granite of Pavo Kug wash
Granodiorite to monzogranite of Kitt Peak
Diorite rocks of Nawt Vaya
PALEOZOIC
Calc-silicate schist
Quartzite
Foliation
Lineation
N = 32
A
A'
CM16-01
CM16-02
CM16-03
CM16-04
CM16-05/06
CM16-07
CM16-08
CM14-01
CM14-02
CM16-09
CM14-03
CM16-10A/B
CM14-04
CM16-11
CM14-05
CM14-06
CM16-12
CM16-13
CM16-14
CM14-07
CM14-08
CM14-09
Ajo road décollement
Elevation (m)
1500
1000
Tg
Tpg
Ksw
1000
2000
3000
4000
5000
6000
Distance (m)

Figure 4.

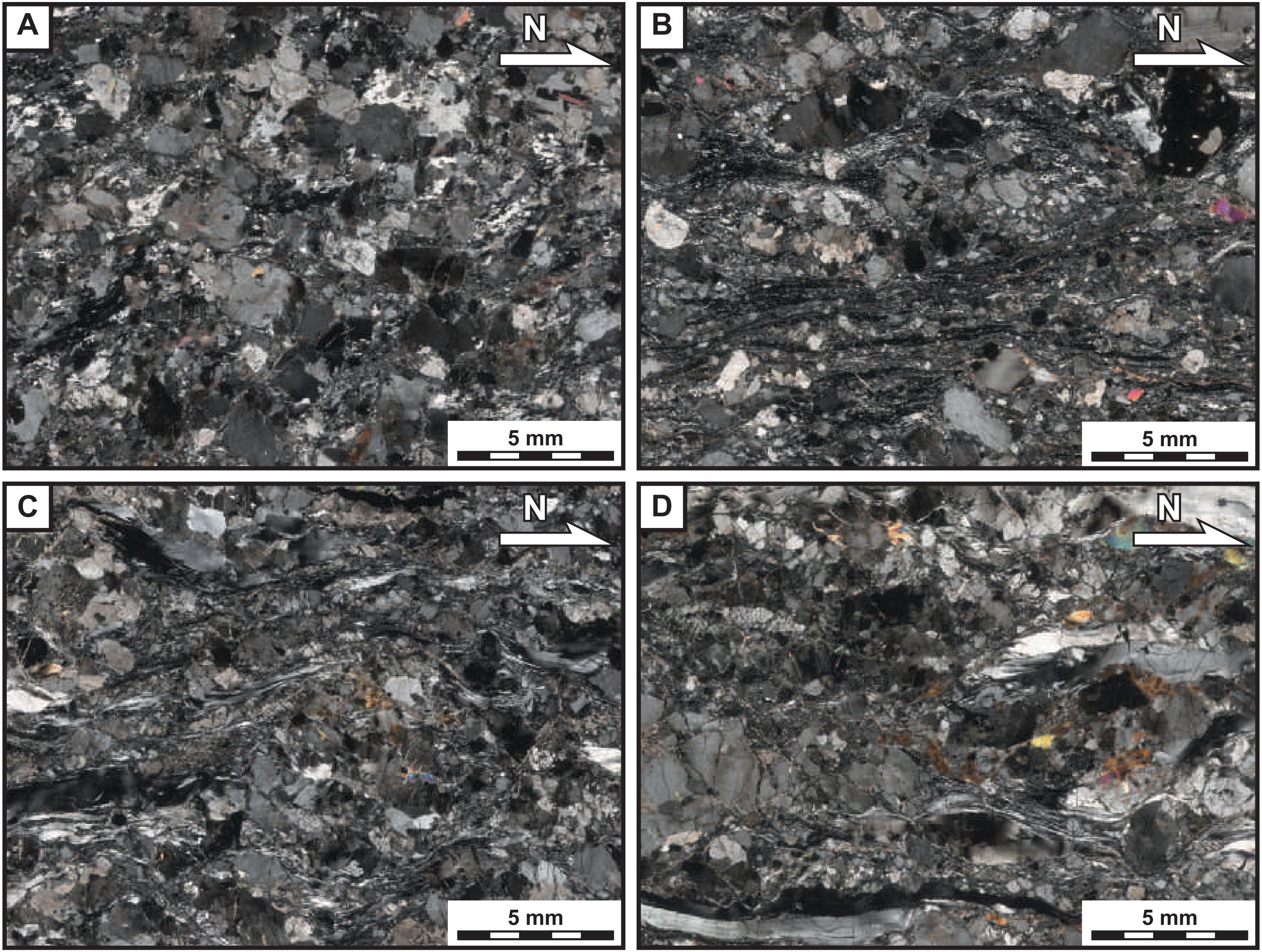
A
N
5 mm
B
N
5 mm
C
N
5 mm
D
N
5 mm

Figure 5.

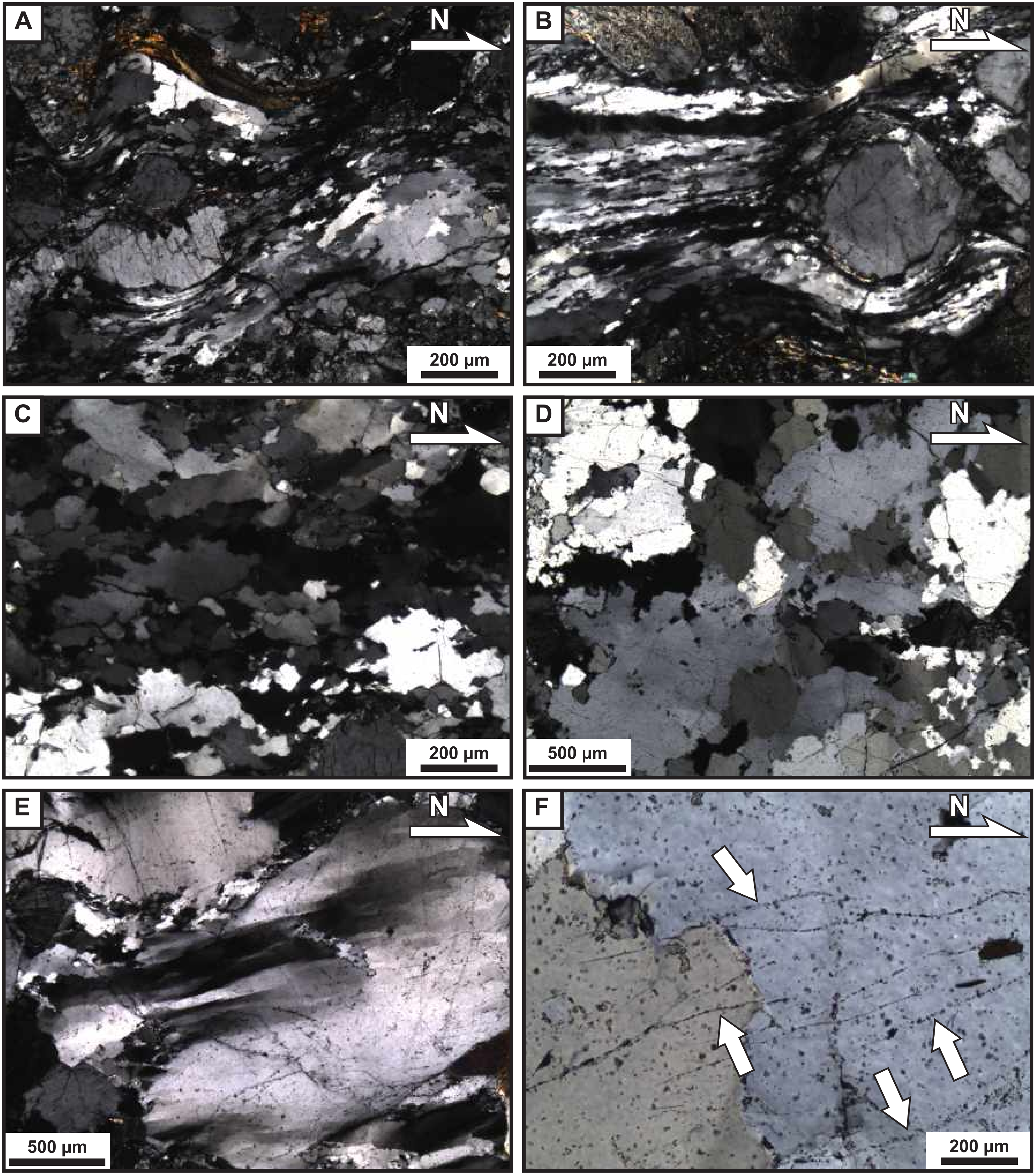
A
N
200 µm
B
N
200 µm
C
N
200 µm
D
N
500 µm
E
N
500 µm
F
N
200 µm

Figure 6.

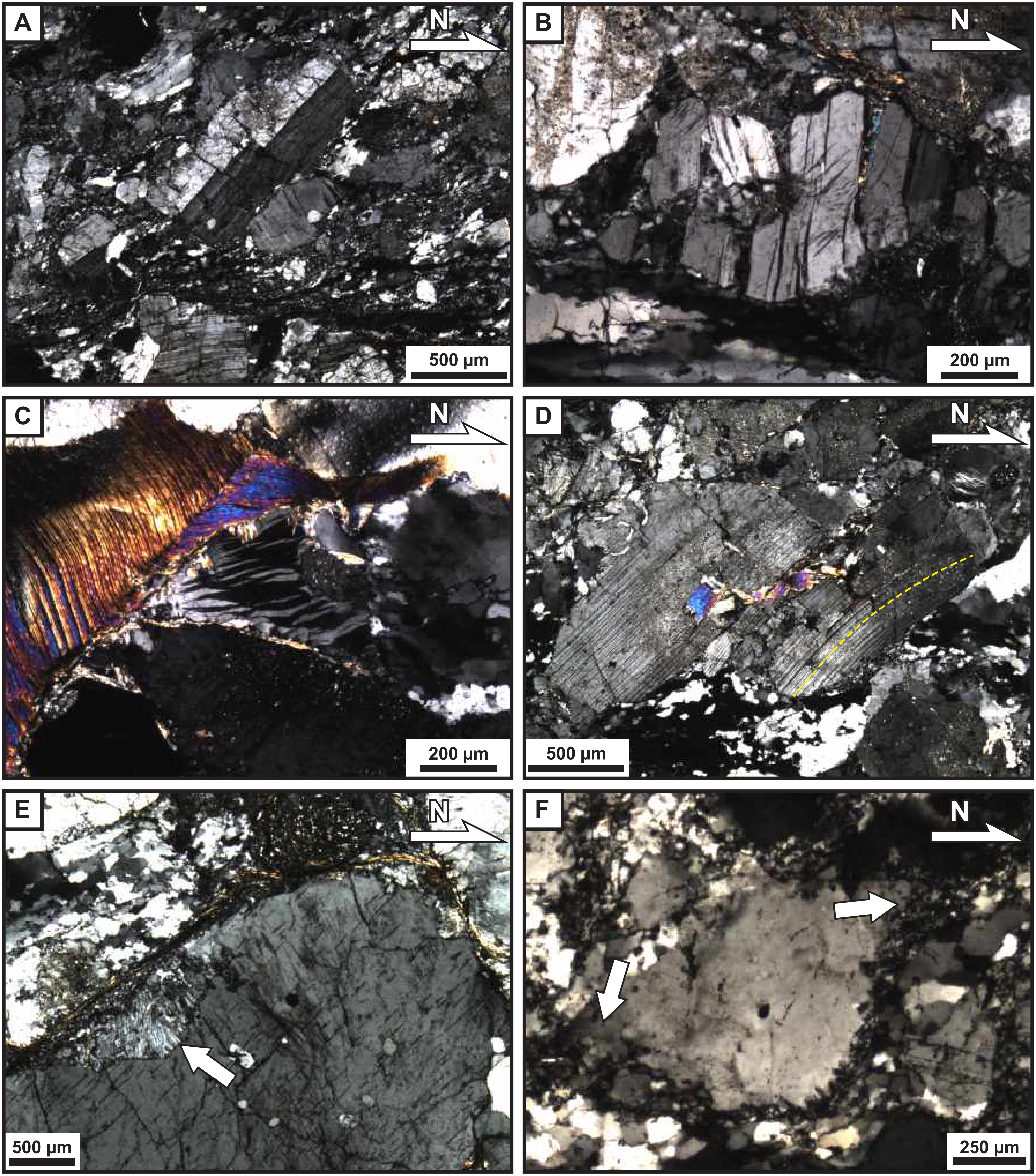
A
N
500 µm
B
N
200 µm
C
N
200 µm
D
N
500 µm
E
N
500 µm
F
N
250 µm

Figure 7.

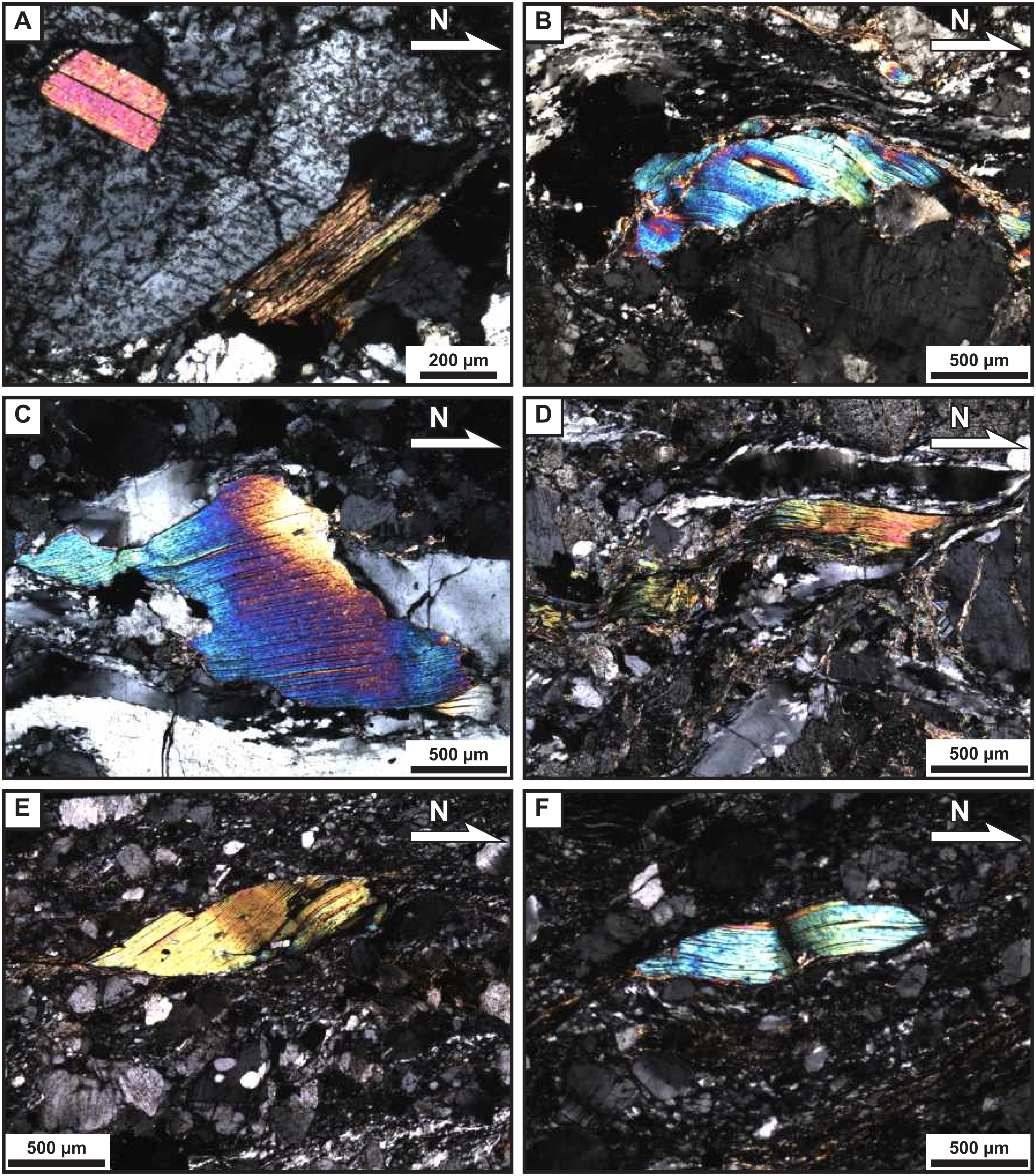
A
N
200 µm
B
N
500 µm
C
N
500 µm
D
N
500 µm
E
N
500 µm
F
N
500 µm

Figure 8.

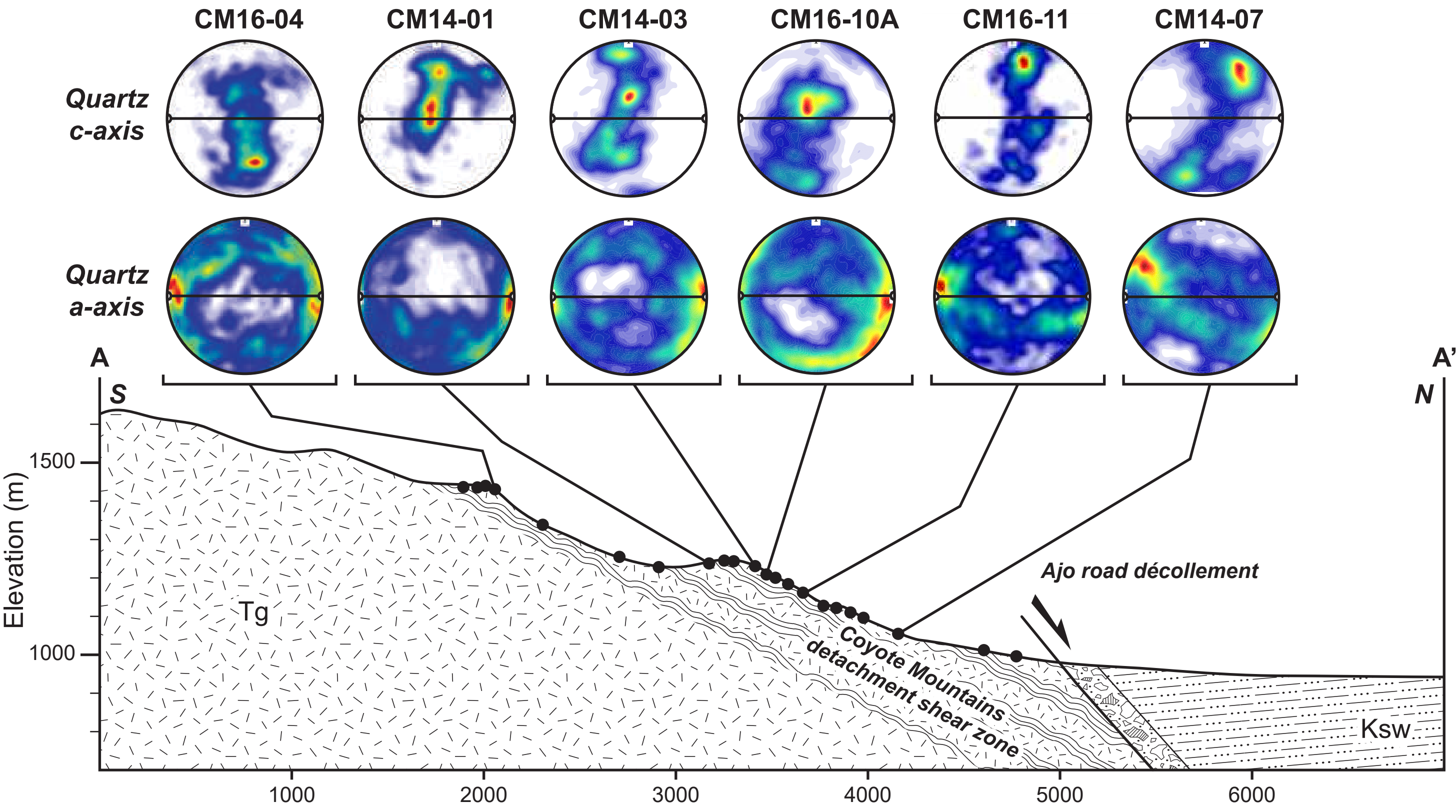
CM16-04
CM14-01
CM14-03
CM16-10A
CM16-11
CM14-07
Quartz c-axis
Quartz a-axis
A
A'
S
N
1500
1000
Elevation (m)
Tg
Ajo road décollement
Coyote Mountains detachment shear zone
Ksw
1000
2000
3000
4000
5000
6000

Figure 9.

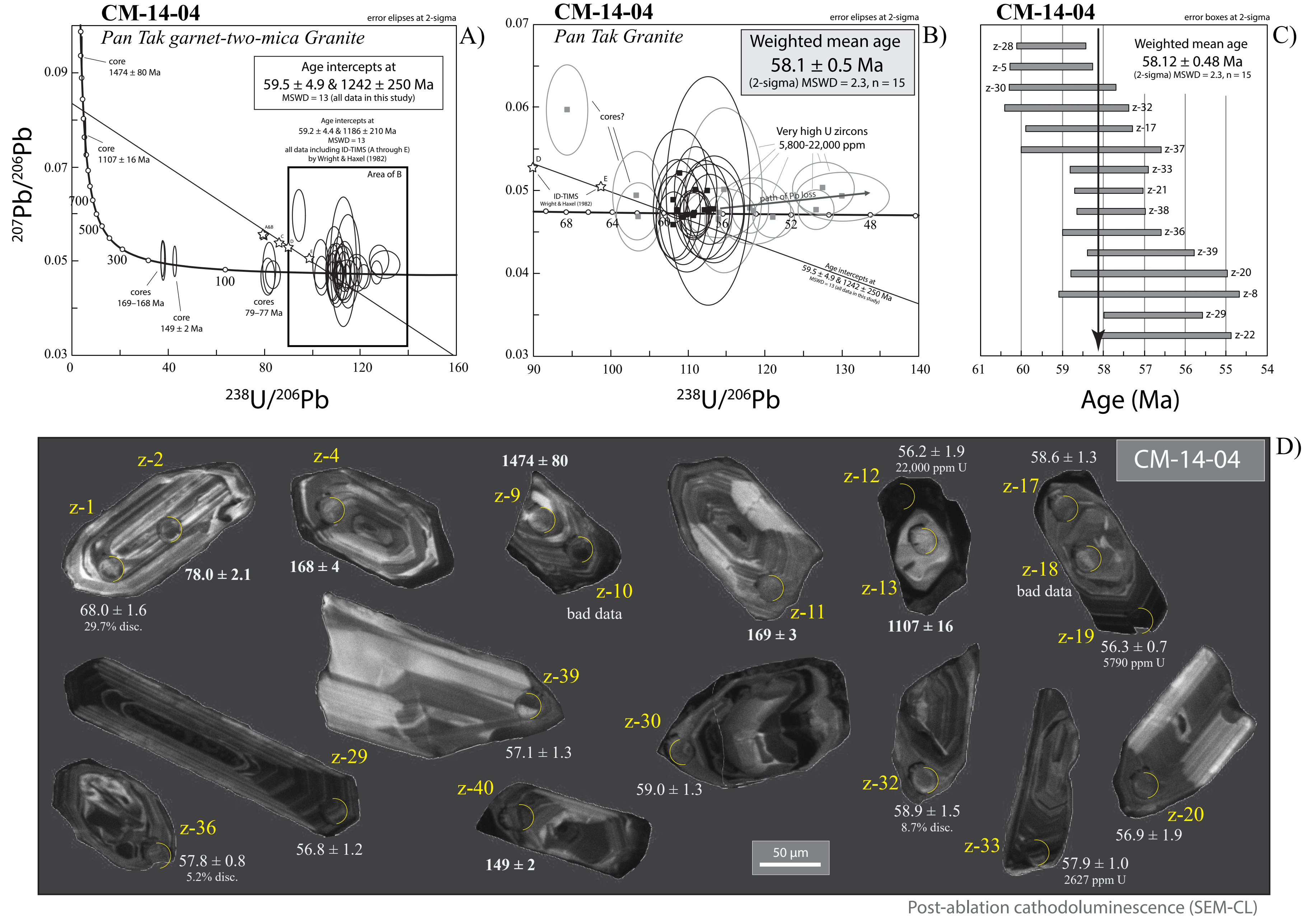

CM-14-04
error elipses at 2-sigma
A)
Pan Tak garnet-two-mica Granite
Age intercepts at
59.5 ± 4.9 & 1242 ± 250 Ma
MSWD = 13 (all data in this study)
Age intercepts at
59.2 ± 4.4 & 1186 ± 210 Ma
MSWD = 13
all data including ID-TIMS (A through E)
by Wright & Haxel (1982)
Area of B
core
1474 ± 80 Ma
core
1107 ± 16 Ma
cores
169–168 Ma
core
149 ± 2 Ma
cores
79–77 Ma
207Pb/206Pb
238U/206Pb
CM-14-04
error elipses at 2-sigma
B)
Pan Tak Granite
Weighted mean age
58.1 ± 0.5 Ma
(2-sigma) MSWD = 2.3, n = 15
cores?
Very high U zircons
5,800-22,000 ppm
path of Pb loss
ID-TIMS
Wright & Haxel (1982)
Age intercepts at
59.5 ± 4.9 & 1242 ± 250 Ma
MSWD = 13 (all data in this study)
238U/206Pb
CM-14-04
error boxes at 2-sigma
C)
Weighted mean age
58.12 ± 0.48 Ma
(2-sigma) MSWD = 2.3, n = 15
Age (Ma)
D)
CM-14-04
z-1
z-2
78.0 ± 2.1
68.0 ± 1.6
29.7% disc.
z-4
168 ± 4
1474 ± 80
z-9
z-10
bad data
169 ± 3
z-11
56.2 ± 1.9
22,000 ppm U
z-12
z-13
1107 ± 16
58.6 ± 1.3
z-17
z-18
bad data
z-19
56.3 ± 0.7
5790 ppm U
z-39
57.1 ± 1.3
z-29
56.8 ± 1.2
z-36
57.8 ± 0.8
5.2% disc.
z-40
149 ± 2
z-30
59.0 ± 1.3
50 μm
z-32
58.9 ± 1.5
8.7% disc.
z-33
57.9 ± 1.0
2627 ppm U
z-20
56.9 ± 1.9
Post-ablation cathodoluminescence (SEM-CL)

Figure 10.

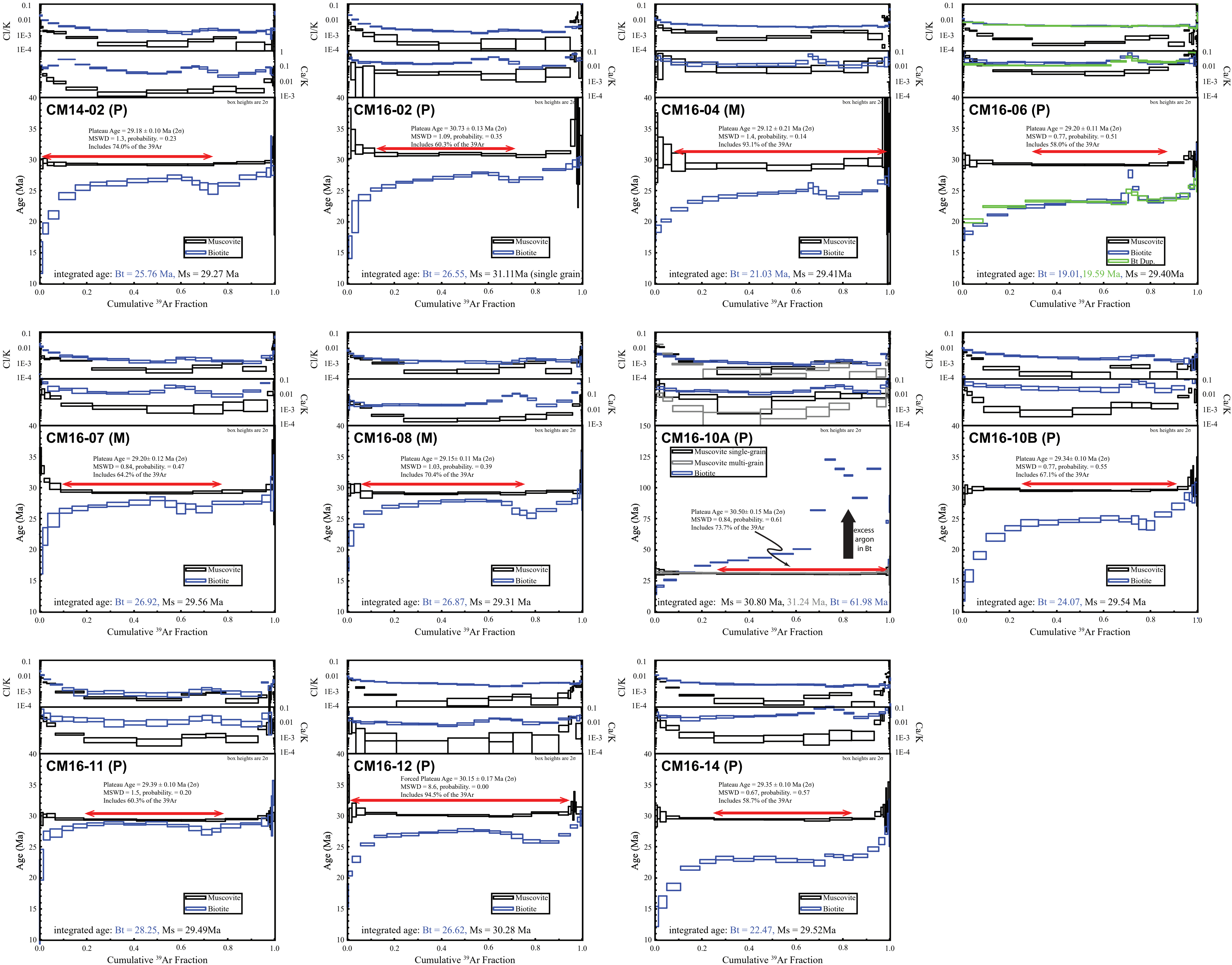
CM14-02 (P)
Plateau Age = 29.18 ± 0.10 Ma (2σ)
MSWD = 1.3, probability. = 0.23
Includes 74.0% of the 39Ar
integrated age: Bt = 25.76 Ma, Ms = 29.27 Ma
CM16-02 (P)
Plateau Age = 30.73 ± 0.13 Ma (2σ)
MSWD = 1.09, probability. = 0.35
Includes 60.3% of the 39Ar
integrated age: Bt = 26.55, Ms = 31.11Ma (single grain)
CM16-04 (M)
Plateau Age = 29.12 ± 0.21 Ma (2σ)
MSWD = 1.4, probability. = 0.14
Includes 93.1% of the 39Ar
integrated age: Bt = 21.03 Ma, Ms = 29.41Ma
CM16-06 (P)
Plateau Age = 29.20 ± 0.11 Ma (2σ)
MSWD = 0.77, probability. = 0.51
Includes 58.0% of the 39Ar
Bt Dup.
integrated age: Bt = 19.01,19.59 Ma, Ms = 29.40Ma
CM16-07 (M)
Plateau Age = 29.20± 0.12 Ma (2σ)
MSWD = 0.84, probability. = 0.47
Includes 64.2% of the 39Ar
integrated age: Bt = 26.92, Ms = 29.56 Ma
CM16-08 (M)
Plateau Age = 29.15± 0.11 Ma (2σ)
MSWD = 1.03, probability. = 0.39
Includes 70.4% of the 39Ar
integrated age: Bt = 26.87, Ms = 29.31 Ma
CM16-10A (P)
Muscovite single-grain
Muscovite multi-grain
Plateau Age = 30.50± 0.15 Ma (2σ)
MSWD = 0.84, probability. = 0.61
Includes 73.7% of the 39Ar
excess argon in Bt
integrated age: Ms = 30.80 Ma, 31.24 Ma, Bt = 61.98 Ma
CM16-10B (P)
Plateau Age = 29.34± 0.10 Ma (2σ)
MSWD = 0.77, probability. = 0.55
Includes 67.1% of the 39Ar
integrated age: Bt = 24.07, Ms = 29.54 Ma
CM16-11 (P)
Plateau Age = 29.39 ± 0.10 Ma (2σ)
MSWD = 1.5, probability. = 0.20
Includes 60.3% of the 39Ar
integrated age: Bt = 28.25, Ms = 29.49Ma
CM16-12 (P)
Forced Plateau Age = 30.15 ± 0.17 Ma (2σ)
MSWD = 8.6, probability. = 0.00
Includes 94.5% of the 39Ar
integrated age: Bt = 26.62, Ms = 30.28 Ma
CM16-14 (P)
Plateau Age = 29.35 ± 0.10 Ma (2σ)
MSWD = 0.67, probability. = 0.57
Includes 58.7% of the 39Ar
integrated age: Bt = 22.47, Ms = 29.52Ma
Muscovite
Biotite
box heights are 2σ
Cl/K
Ca/K
Age (Ma)
Cumulative 39Ar Fraction

Figure 11.

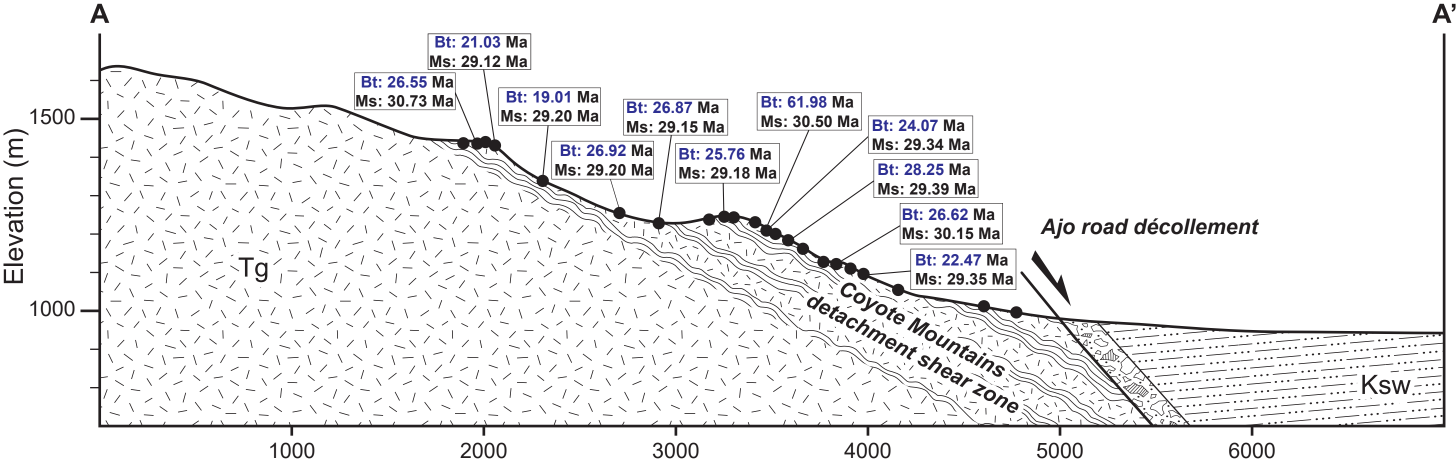
A
A’
Elevation (m)
1500
1000
Bt: 21.03 Ma
Ms: 29.12 Ma
Bt: 26.55 Ma
Ms: 30.73 Ma
Bt: 19.01 Ma
Ms: 29.20 Ma
Bt: 26.87 Ma
Ms: 29.15 Ma
Bt: 61.98 Ma
Ms: 30.50 Ma
Bt: 24.07 Ma
Ms: 29.34 Ma
Bt: 26.92 Ma
Ms: 29.20 Ma
Bt: 25.76 Ma
Ms: 29.18 Ma
Bt: 28.25 Ma
Ms: 29.39 Ma
Bt: 26.62 Ma
Ms: 30.15 Ma
Bt: 22.47 Ma
Ms: 29.35 Ma
Ajo road décollement
Tg
Coyote Mountains
detachment shear zone
Ksw
1000
2000
3000
4000
5000
6000

Figure 12.

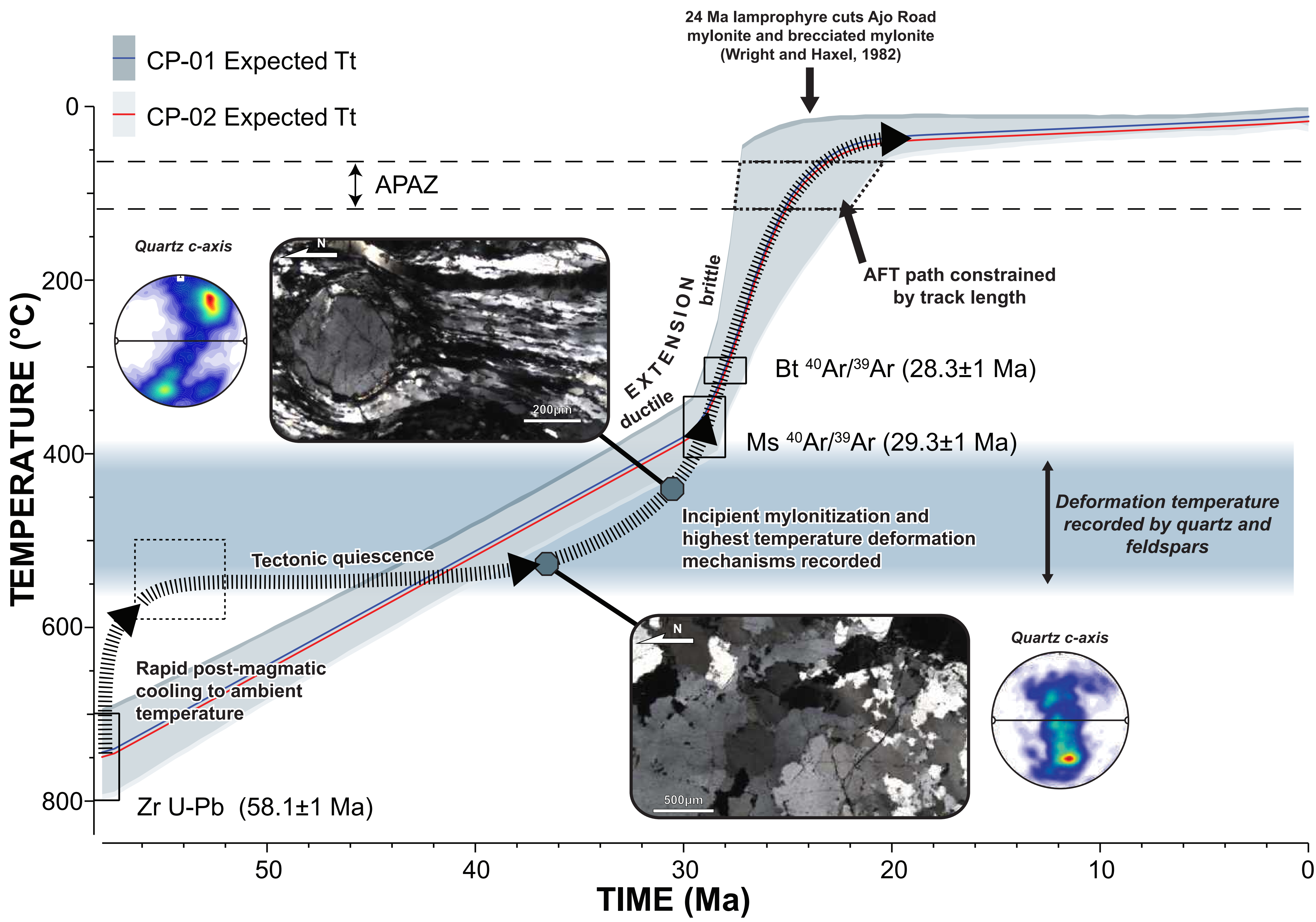

CP-01 Expected Tt
CP-02 Expected Tt
24 Ma lamprophyre cuts Ajo Road mylonite and brecciated mylonite (Wright and Haxel, 1982)
APAZ
AFT path constrained by track length
Quartz c-axis
N
200µm
EXTENSION
ductile
brittle
Bt $^{40}Ar/^{39}Ar$ (28.3±1 Ma)
Ms $^{40}Ar/^{39}Ar$ (29.3±1 Ma)
Deformation temperature recorded by quartz and feldspars
Incipient mylonitization and highest temperature deformation mechanisms recorded
Tectonic quiescence
Rapid post-magmatic cooling to ambient temperature
N
500µm
Quartz c-axis
Zr U-Pb (58.1±1 Ma)
TEMPERATURE (°C)
0
200
400
600
800
TIME (Ma)
50
40
30
20
10
0

Figure 13.

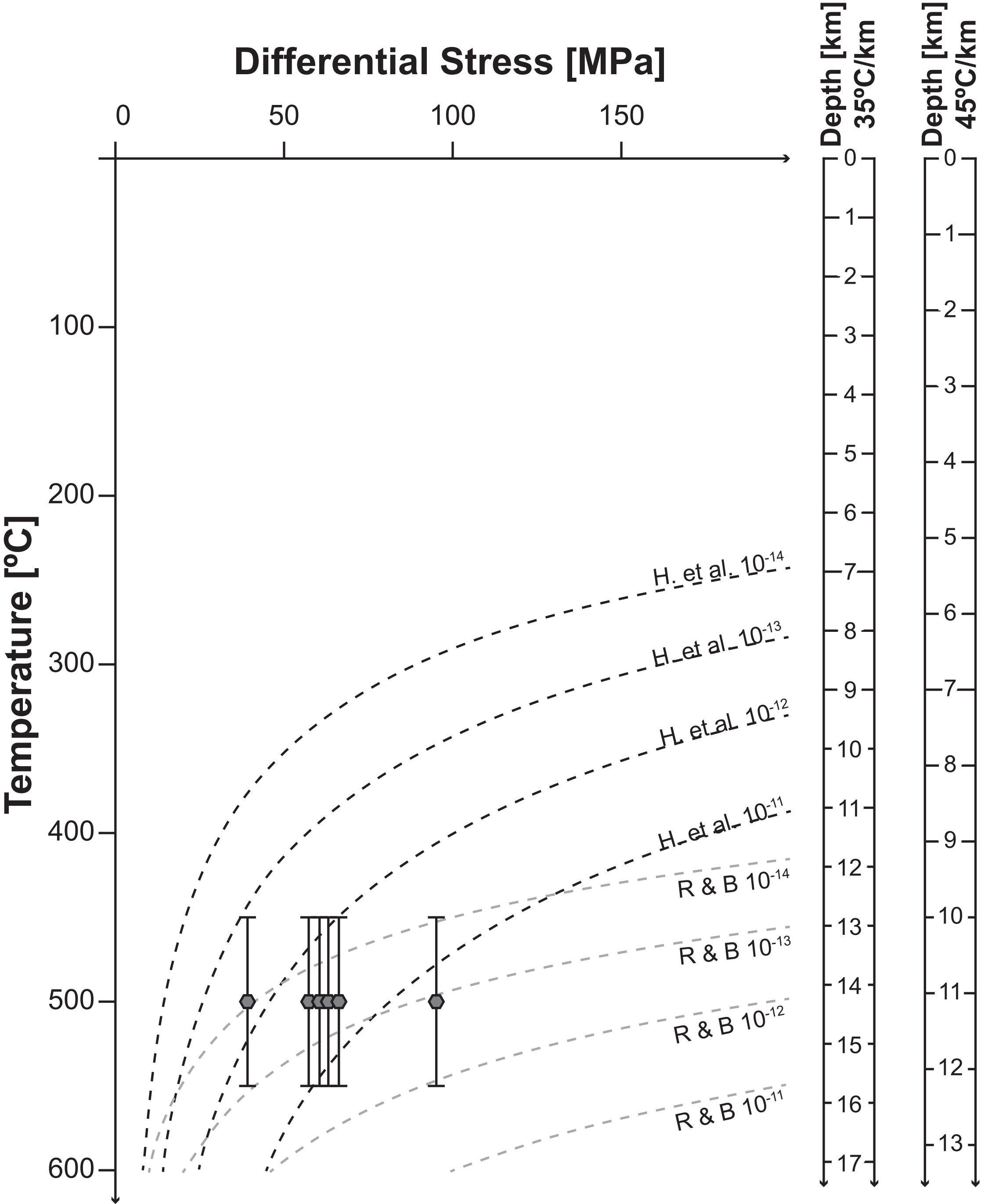

Differential Stress [MPa]
0
50
100
150
Temperature [ºC]
100
200
300
400
500
600
Depth [km] 35ºC/km
Depth [km] 45ºC/km
H. et al. 10-14
H. et al. 10-13
H. et al. 10-12
H. et al. 10-11
R & B 10-14
R & B 10-13
R & B 10-12
R & B 10-11

Figure 14.

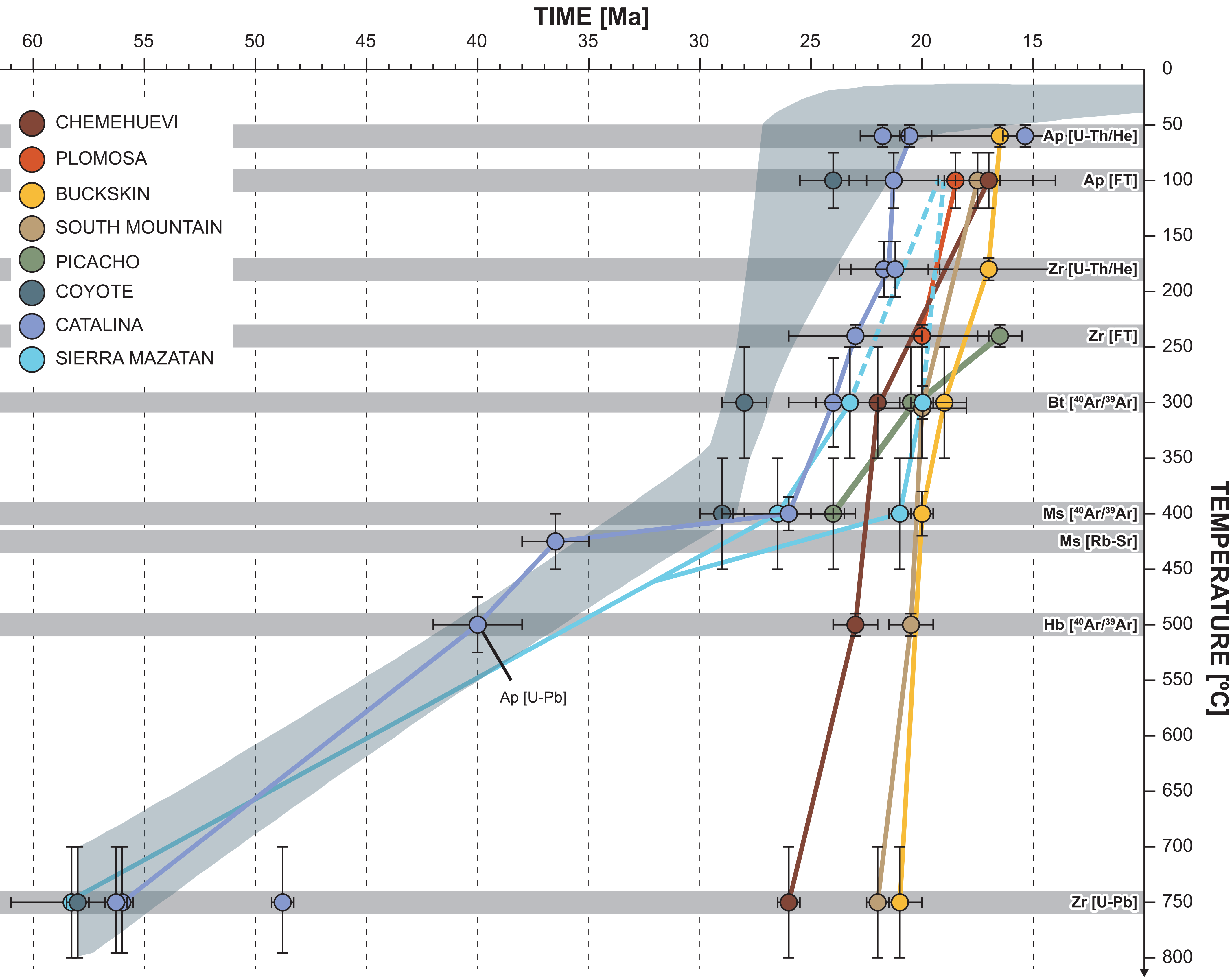

TIME [Ma]
60
55
50
45
40
35
30
25
20
15
CHEMEHUEVI
PLOMOSA
BUCKSKIN
SOUTH MOUNTAIN
PICACHO
COYOTE
CATALINA
SIERRA MAZATAN
Ap [U-Th/He]
Ap [FT]
Zr [U-Th/He]
Zr [FT]
Bt [40Ar/39Ar]
Ms [40Ar/39Ar]
Ms [Rb-Sr]
Hb [40Ar/39Ar]
Ap [U-Pb]
Zr [U-Pb]
0
50
100
150
200
250
300
350
400
450
500
550
600
650
700
750
800
TEMPERATURE [°C]

Figure 15.

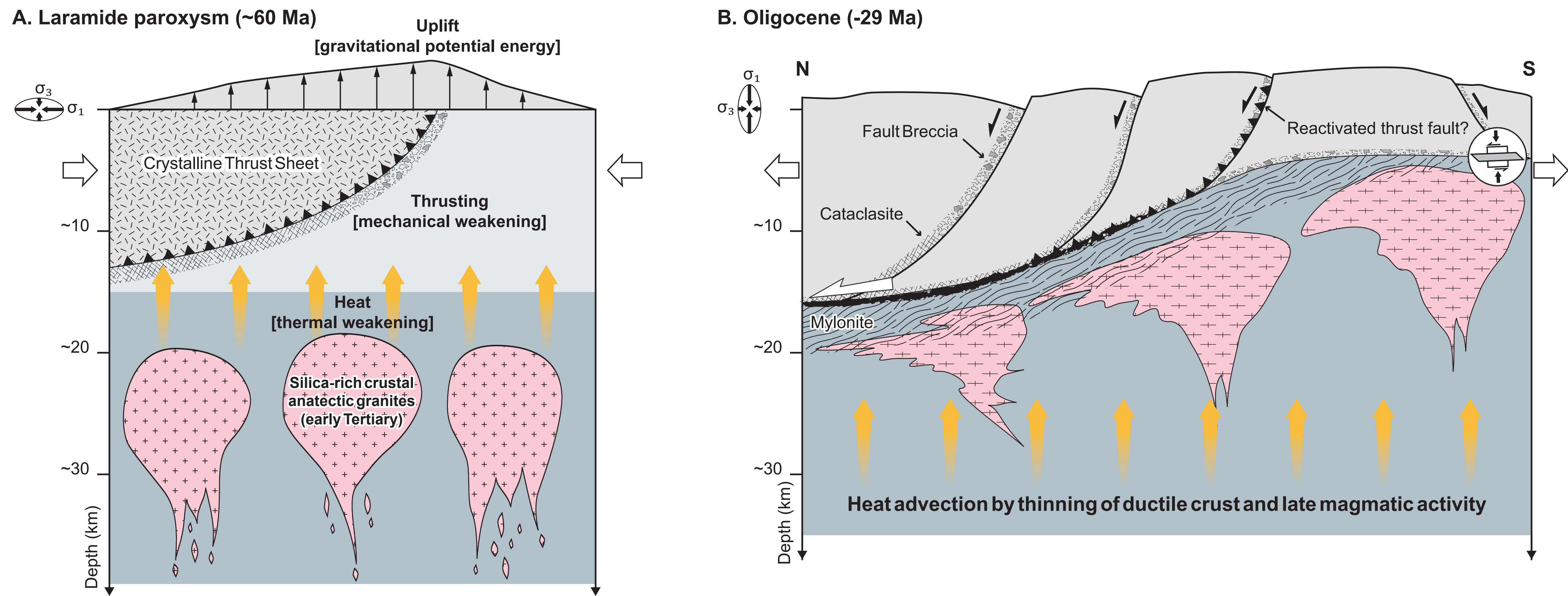

A. Laramide paroxysm (~60 Ma)
Uplift
[gravitational potential energy]
σ3
σ1
Crystalline Thrust Sheet
Thrusting
[mechanical weakening]
Heat
[thermal weakening]
Silica-rich crustal
anatectic granites
(early Tertiary)
~10
~20
~30
Depth (km)
B. Oligocene (-29 Ma)
N
S
σ1
σ3
Fault Breccia
Reactivated thrust fault?
Cataclasite
Mylonite
~10
~20
~30
Depth (km)
Heat advection by thinning of ductile crust and late magmatic activity

Figure S1.

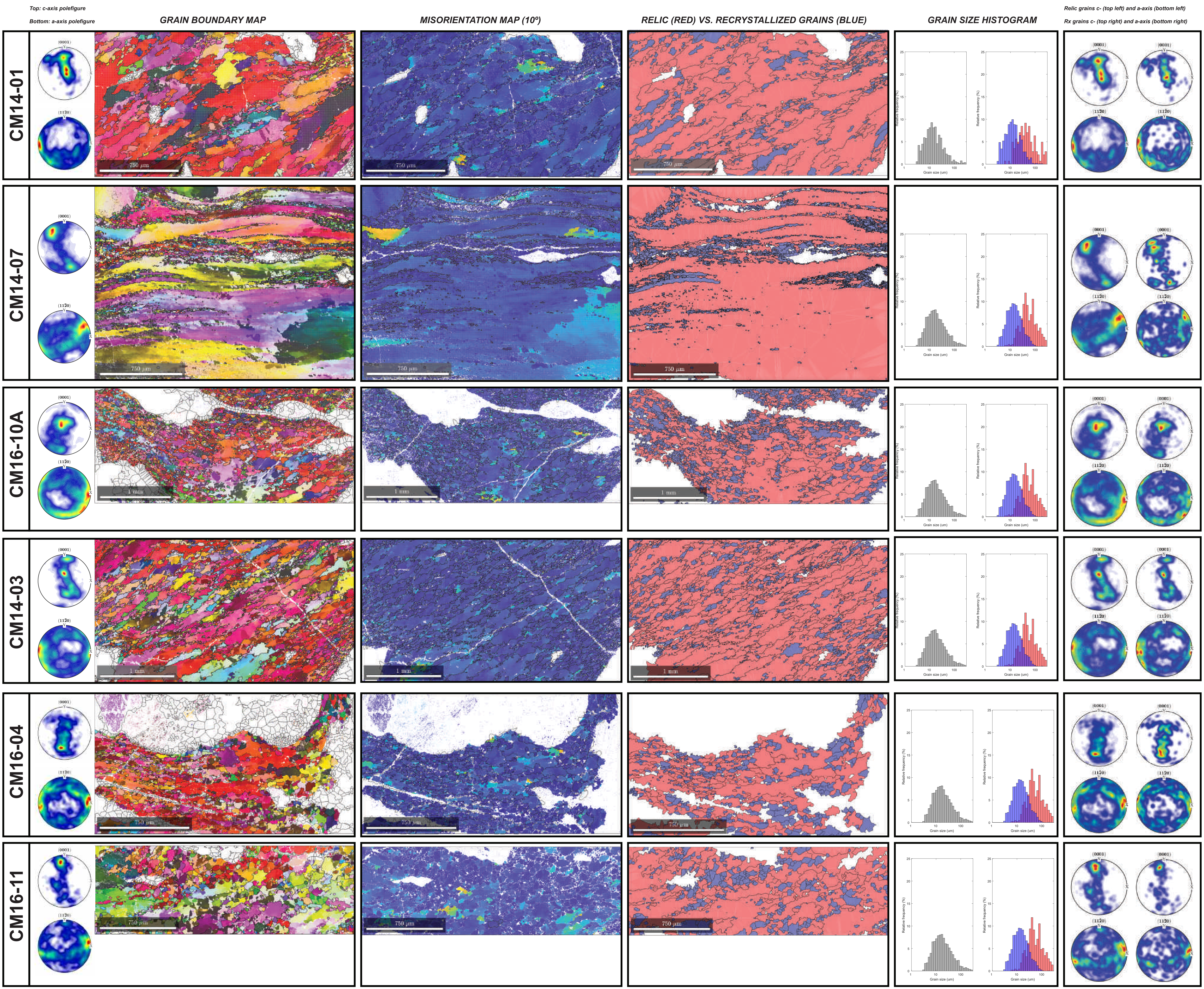

Top: c-axis polefigure
Bottom: a-axis polefigure
GRAIN BOUNDARY MAP
MISORIENTATION MAP (10º)
RELIC (RED) VS. RECRYSTALLIZED GRAINS (BLUE)
GRAIN SIZE HISTOGRAM
Relic grains c- (top left) and a-axis (bottom left)
Rx grains c- (top right) and a-axis (bottom right)
CM14-01
CM14-07
CM16-10A
CM14-03
CM16-04
CM16-11
750 μm
1 mm
(0001)
(11$\bar{2}$0)
Relative frequency (%)
Grain size (um)

Figure S2.

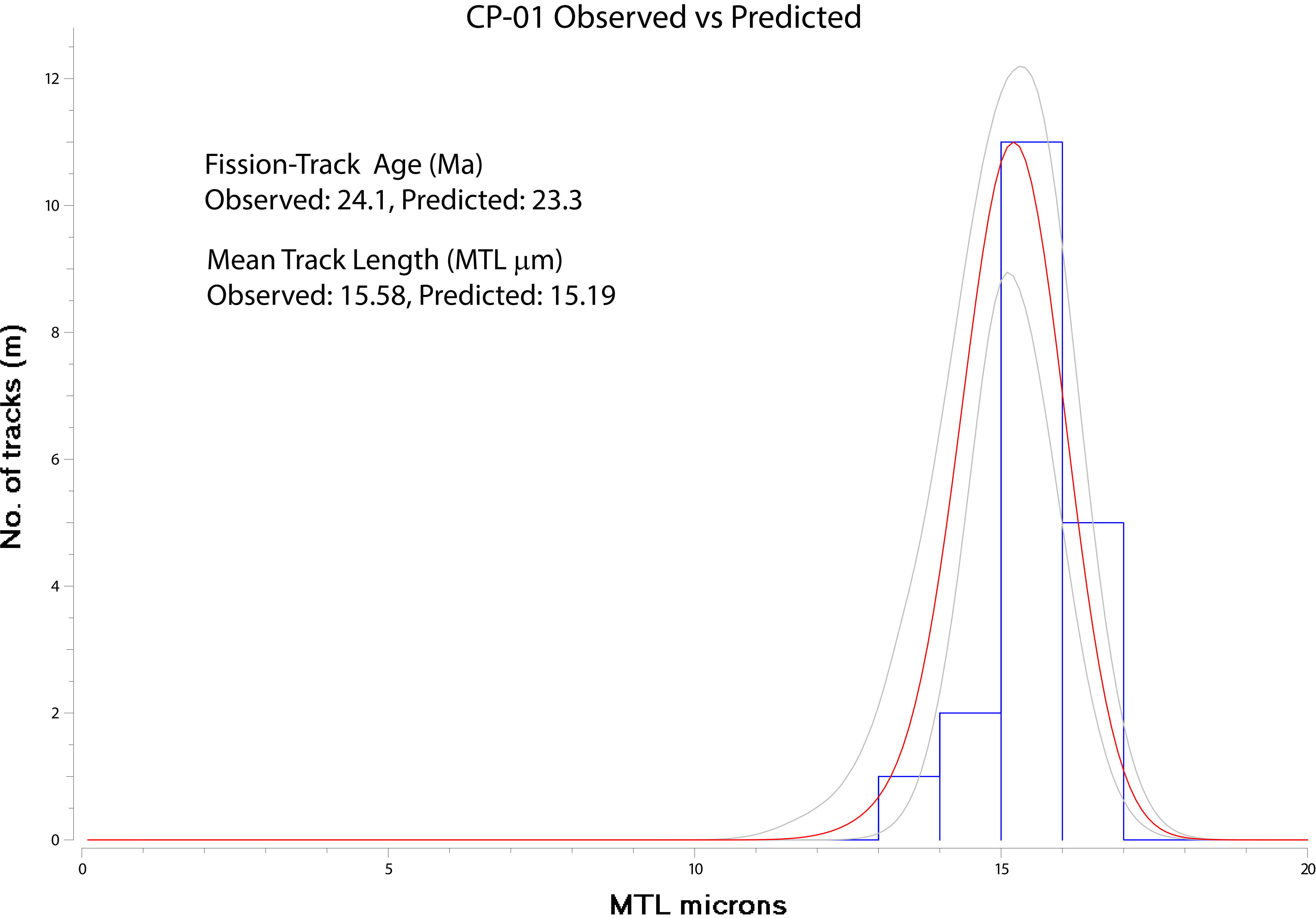
CP-01 Observed vs Predicted
Fission-Track Age (Ma)
Observed: 24.1, Predicted: 23.3
Mean Track Length (MTL µm)
Observed: 15.58, Predicted: 15.19
No. of tracks (m)
MTL microns
0
2
4
6
8
10
12
5
15
20

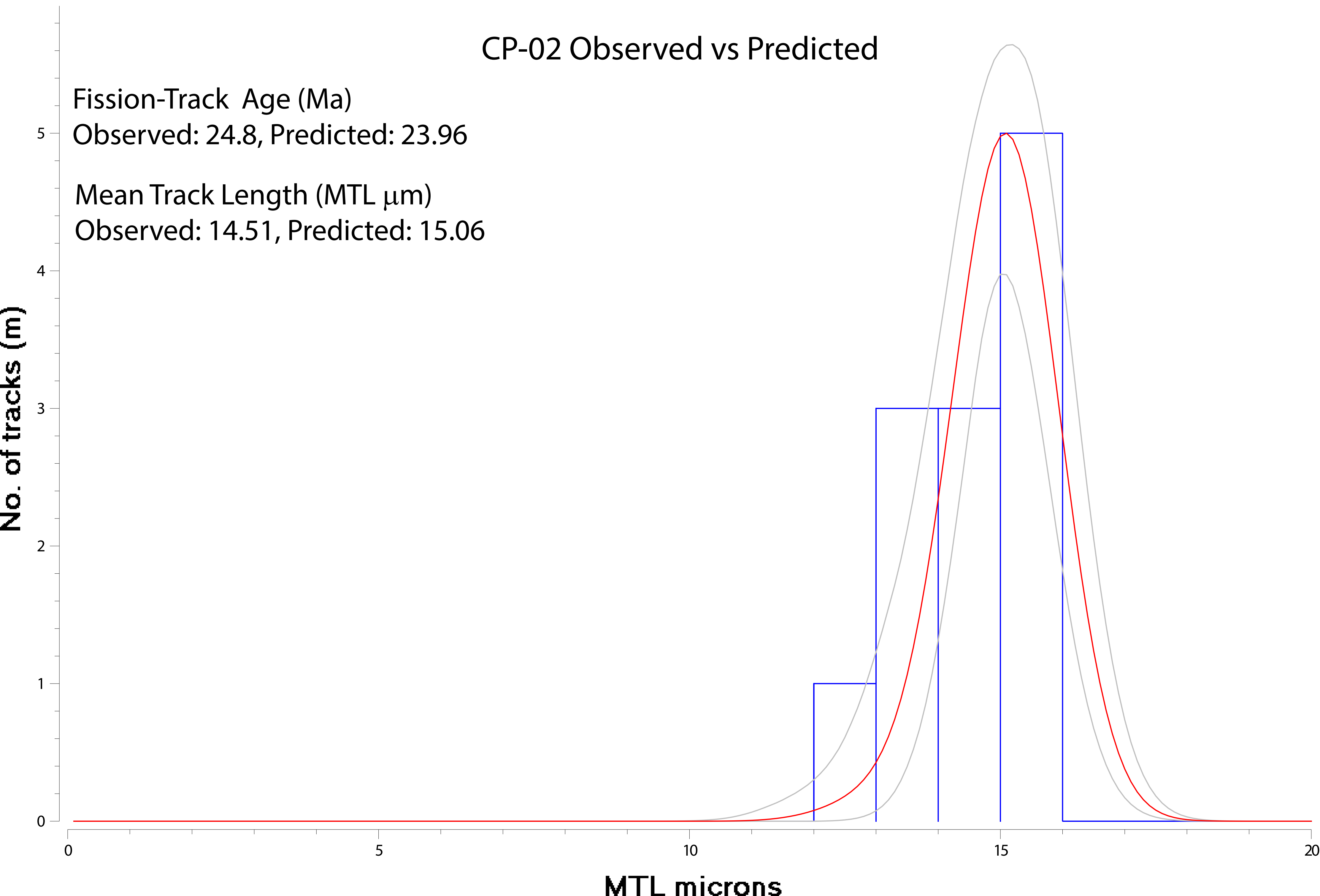
CP-02 Observed vs Predicted
Fission-Track Age (Ma)
Observed: 24.8, Predicted: 23.96
Mean Track Length (MTL µm)
Observed: 14.51, Predicted: 15.06
No. of tracks (m)
MTL microns
0
1
2
3
4
5
10
15
20

Table 1: Microstructural analysis summary, including quartz recrystallized grain size measured by EBSD, Flow stress calculation using the Cross et al. (2017) paleo-piezometer, and strain rate estimation based on the Hirth et al. (2001) quartzite flow law at a temperature of 500°C.

Sample	Diameter (μm)			Flow Stress (MPa)	Strain Rate (s^{-1})
CM14-01	23.6	±	16.6	63.0	3.7×10^{-12}
CM14-03	23.9	±	15.1	62.4	3.6×10^{-12}
CM14-07	13.1	±	7.6	95.6	2.0×10^{-11}
CM16-04	24.9	±	14.6	60.7	3.2×10^{-12}
CM16-10A	26.8	±	15.7	57.6	2.6×10^{-12}
CM16-11	46.1	±	43.8	39.2	5.6×10^{-13}
CM16-12	21.9	±	15.2	66.4	4.6×10^{-12}

Table 2: Summary table of $^{40}Ar/^{39}Ar$ ages of biotite (Bt) and muscovite (Ms). Aliquots were 10–50 grains unless otherwise indicated. *indicates uncertainty expanded due to high MSWD. TG = Total Gas.

Sample	Mineral	Mass (mg)	Age		Notes
			TG age	Plateau age	
CM14-02	Bt	2.731	25.76		
	Ms	5.370	29.27	29.18 ± 0.10	
CM-16-02	Bt	6.086	26.55		
	Ms	1.013	31.11	31.73 ± 0.11	Single grain
CM16-04	Bt	5.366	21.03		
	Ms	0.727	29.41	29.12 ± 0.21	
CM16-06	Bt	4.696	19.01		
	Bt	6.847	19.59		
	Ms	4.011	29.40	29.20 ± 0.10	
CM16-07	Bt	1.588	26.92		
	Ms	3.220	29.56	29.20 ± 0.12	Kinked grain
CM16-08	Bt	4.052	26.87		
	Ms	2.969	29.31	29.15 ± 0.11	
CM16-10A	Bt	3.536	61.98		Excess argon?
	Ms	0.979	30.80	30.5 ± 0.12	Single grain
	Ms	6.37	31.24		4 grains
CM16-10B	Bt	2.387	28.25		
	Ms	6.051	29.49	29.39 ± 0.10	Oldest Bt
CM16-12	Bt	1.008	26.62		> 50 grains
	Ms	4.500	30.28	30.15 ± 0.17*	Forced plateau
CM16-14	Bt	4.693	22.47		
	Ms	4.440	29.52	29.35 ± 0.10	6 grains

Table 3: Apatite fission track ages.

Sample number	No. of crystals	Track density (× 10^5 tracks.cm^{-2}) (Number of tracks)			Mean Dpar µm	Age Dispersion ($P\chi^2$)	Central Age ± 1σ (Ma)	MTL (µm)	SD	N_L
		$\rho_s(N_s)$	$\rho_i(N_i)$	$\rho_d(N_d)$						
CP-01	20	1.545 (122)	1.296 (1023)	11.86 (5533)	1.9	<0.01% (99.84%)	24.1 ± 2.4	13.7	0.9	19
CP-02	20	2.276 (123)	18.84 (1018)	11.86 (5533)	2.3	31.58% (7.36%)	24.0 ± 3.1	13.6	0.9	12
Analyses by external detector method using 0.5 for the 4π/2π geometry correction factor. Ages calculated using dosimeter glass: CN5 with ζCN5 = 341.6 ± 8.5 (apatite). $P\chi^2$ is the probability of obtaining a χ^2 value for v degrees of freedom where v = no. of crystals – 1σ - standard error of the mean.										

Table 4. U-Th-Pb analytical data for LA-ICPMS spot analyses on zircon grains for the Pan Tak garnet-two-mica granite, Coyote Mountains, southerm Arizona, USA

Analisys/Zircon		U# (ppm)	Th# (ppm)	Th/U	CORRECTED ISOTOPIC RATIOS $^{207}Pb/^{206}Pb$	err %*	$^{207}Pb/^{235}U$†	err %*	$^{206}Pb/^{238}U$†	err %*	$^{208}Pb/^{232}Th$	err %*	Rho**	% disc.***	CORRECTED $^{206}Pb/^{238}U$	±2s*	$^{207}Pb/^{235}U$
Sample **CM-14-04**	**Pan Tak garnet-two-mica granite** (Coyote Mountains, southern Arizona)							Mount **ICGEO-262** (November 2019)									
CM14-**25**	R	5930	1540	0.26	0.04890	4.9	0.05210	6.1	0.00768	3.8	0.00255	4.7	0.615	4	49.3	1.9	51.6
CM14-**23**	R	15100	3770	0.25	0.05050	5.1	0.05420	5.7	0.00783	2.6	0.00257	5.8	0.447	6	50.3	1.3	53.6
CM14-**14**	R	18900	6260	0.33	0.04820	3.9	0.05178	4.4	0.00789	1.5	0.00248	3.0	0.342	1	50.7	0.8	51.3
CM14-**31**	inner R	7600	1110	0.15	0.04670	4.3	0.05310	4.7	0.00825	1.8	0.00228	5.7	0.386	-1	53.0	1.0	52.5
CM14-**12**	R	22000	5410	0.25	0.04782	4.8	0.05520	7.6	0.00843	3.3	0.00218	6.0	0.437	1	54.1	1.8	54.5
CM14-**35**	R	7050	640	0.09	0.04920	4.5	0.05570	5.4	0.00846	1.7	0.00258	7.4	0.307	1	54.3	0.9	55.0
CM14-**34**	C	158	152	0.96	0.05040	17.9	0.06000	16.7	0.00871	3.6	0.00259	8.1	0.214	5	55.9	2.0	59.0
CM14-**3**	R	5080	871	0.17	0.04680	4.3	0.05700	6.1	0.00875	3.3	0.00264	5.3	0.540	0	56.2	1.9	56.3
CM14-**19**	outer C	5790	3407	0.59	0.04660	4.7	0.05610	5.2	0.00876	1.3	0.00265	2.6	0.243	-2	56.3	0.7	55.4
CM14-**22**	R	517	85	0.16	0.04790	12.5	0.05790	11.4	0.00881	2.8	0.00298	13.4	0.249	1	56.5	1.6	57.0
CM14-**29**	R	794	599	0.75	0.04830	7.7	0.05820	7.6	0.00885	2.1	0.00291	4.5	0.284	1	56.8	1.2	57.3
CM14-**8**	R	134	98	0.73	0.05500	21.8	0.06100	23.0	0.00887	3.9	0.00268	14.6	0.172	4	56.9	2.2	59.0
CM14-**20**	R	348	710	2.04	0.04870	10.9	0.05790	10.4	0.00886	3.3	0.00270	4.4	0.316	0	56.9	1.9	57.0
CM14-**39**	R	434	397	0.91	0.04820	11.2	0.05840	10.4	0.00890	2.4	0.00279	5.7	0.226	2	57.1	1.3	58.3
CM14-**36**	R	762	57	0.08	0.05030	8.7	0.06210	8.7	0.00900	2.0	0.00363	14.0	0.230	5	57.8	1.2	61.0
CM14-**38**	R	4820	3750	0.78	0.04720	4.7	0.05860	4.9	0.00901	1.4	0.00276	2.4	0.292	0	57.8	0.8	57.8
CM14-**21**	R	3129	1291	0.41	0.04720	5.1	0.05830	5.1	0.00902	1.4	0.00270	3.3	0.280	-1	57.9	0.8	57.5
CM14-**33**	R	2627	793	0.30	0.04750	4.8	0.05860	5.3	0.00902	1.7	0.00288	4.9	0.314	0	57.9	1.0	57.8
CM14-**37**	R	361	385	1.07	0.04650	13.3	0.05890	12.2	0.00909	3.0	0.00293	6.5	0.243	-1	58.3	1.7	57.9
CM14-**17**	inner R	613	70	0.11	0.04730	10.4	0.05870	10.1	0.00913	2.3	0.00315	14.0	0.229	-1	58.6	1.3	57.8
CM14-**32**	R	463	67	0.14	0.05290	9.3	0.06570	8.8	0.00917	2.6	0.00327	14.7	0.296	9	58.9	1.5	64.5
CM14-**30**	R	710	74	0.10	0.04770	10.1	0.06040	10.6	0.00920	2.3	0.00332	12.0	0.215	1	59.0	1.3	59.4
CM14-**5**	R	897	96	0.11	0.04610	7.4	0.05830	7.4	0.00924	1.7	0.00296	12.5	0.235	-3	59.3	1.0	57.5
CM14-**28**	R	3027	1078	0.36	0.04940	4.9	0.06220	5.0	0.00924	1.4	0.00299	3.3	0.282	4	59.3	0.8	61.9
CM14-**15**	inner R	1807	786	0.43	0.04740	6.5	0.06230	7.5	0.00965	2.3	0.00315	6.0	0.302	-1	61.9	1.4	61.4
CM14-**6**	R?	687	141	0.21	0.04800	10.4	0.06580	9.1	0.00967	2.5	0.00348	19.8	0.272	4	62.0	1.5	64.6
CM14-**1**	R?	638	1230	1.93	0.06110	7.5	0.08720	7.8	0.01060	2.4	0.00323	6.2	0.302	20	68.0	1.6	84.7
CM14-**24**	C	642	159	0.25	0.04810	5.8	0.07770	6.0	0.01197	3.2	0.00496	8.3	0.525	-1	76.7	2.4	75.9
CM14-**2**	C	338	349	1.03	0.04880	9.0	0.08160	9.4	0.01218	2.6	0.00380	6.1	0.278	2	78.0	2.1	79.4
CM14-**26**	C or X	1109	214	0.19	0.04690	6.0	0.07910	7.6	0.01229	2.9	0.00739	5.4	0.386	-2	78.7	2.3	77.3
CM14-**40**	inner R	1002	792	0.79	0.05030	5.2	0.16160	5.4	0.02347	1.6	0.00811	3.0	0.289	2	149.5	2.3	151.9
CM14-**4**	C	496	238	0.48	0.05010	6.8	0.18200	7.1	0.02641	2.2	0.00842	3.9	0.302	1	168.1	3.6	169.6
CM14-**11**	C or X	352	313	0.89	0.05030	7.2	0.18520	6.5	0.02658	1.9	0.00752	4.5	0.290	2	169.1	3.1	172.1
CM14-**13**	C	155	31	0.20	0.07670	4.2	1.97000	4.6	0.18740	1.6	0.05550	5.2	0.347	0	1107.0	16.0	1106.0
CM14-**9**	C	277	146	0.53	0.09260	4.0	3.16700	5.4	0.24820	2.8	0.07760	4.8	0.525	1	1429.0	37.0	1448.0

n = 35

R-rim, C-core, X-xenocryst

#U and Th concentrations (ppm) are calculated relative to analyses of trace-element glass standard NIST 610

†Isotopic ratios are corrected relative to 91500 standard zircon for mass bias and down-hole fractionation (91500 with an age ~1065 Ma; Wiedenbec *et al.* , 1995). Isotopic $^{207}Pb/^{206}Pb$ ratios, ages a

*All errors in isotopic ratios are in percentage whereas ages are reported in absolute and given at the 2-sigma level. The weighted mean $^{206}Pb/^{238}U$ age is also reported in absolute values at the 2-sign the methodology discussed by Paton *et al.* (2010).

**Rho is the error correlation value for the isotopic ratios $^{206}Pb/^{238}U$ and $^{207}Pb/^{235}U$ calculated by dividing these two percentage errors. The Rho value is required for plotting concordia diagrams

***Percentage discordance values are obtained using the following equation (100*[(edad $^{207}Pb/^{235}U$)-(edad $^{206}Pb/^{238}U$)]/edad $^{207}Pb/^{235}U$). Positive and negative values indicate normal and inverse d

Individual zircon ages in bold were used to calculate the weighted mean $^{206}Pb/^{238}U$ age and MSWD (Mean Square of Weigthed Deviates) using the computacional program Isoplot (Ludwig , 2003)

AGES (Ma)				
±2s*	^{207}Pb/^{206}Pb	±2s*	Best Age (Ma)	± 2s
3.1	135	110	49.3	± 1.9
3.0	206	110	50.3	± 1.3
2.2	107	90	50.7	± 0.8
2.4	49	92	53.0	± 1.0
4.0	88	110	54.1	± 1.8
2.8	152	100	54.3	± 0.9
9.9	90	340	55.9	± 2.0
3.3	42	95	56.2	± 1.9
2.7	30	100	56.3	± 0.7
6.1	130	220	**56.5**	**± 1.6**
4.2	110	160	**56.8**	**± 1.2**
13.0	140	360	**56.9**	**± 2.2**
5.7	90	220	**56.9**	**± 1.9**
6.0	120	210	**57.1**	**± 1.3**
5.3	190	180	**57.8**	**± 1.2**
2.7	59	98	**57.8**	**± 0.8**
2.9	56	110	**57.9**	**± 0.8**
3.0	88	110	**57.9**	**± 1.0**
6.9	10	240	**58.3**	**± 1.7**
5.7	80	210	**58.6**	**± 1.3**
5.5	290	200	**58.9**	**± 1.5**
6.1	40	200	**59.0**	**± 1.3**
4.1	50	150	**59.3**	**± 1.0**
3.0	150	110	**59.3**	**± 0.8**
4.5	90	130	61.9	± 1.4
5.7	130	190	62.0	± 1.5
6.3	650	160	68.0	± 1.6
4.4	100	120	76.7	± 2.4
7.2	160	170	78.0	± 2.1
5.6	40	120	78.7	± 2.3
7.7	207	110	149.5	± 2.3
11.0	170	140	168.1	± 3.6
11.0	170	150	169.1	± 3.1
31.0	1107	83	1107.0	± 16.0
45.0	1474	80	1474.0	± 80.0
Mean ^{206}Pb/^{238}U Age =			**58.12**	**± 0.48**
			(2 sigma, MSWD = 2.3; n = 15)	

nd errors are calculated following Paton *et al.* (2010
na level. The uncertenties have been propagated foll

iscordance, respectively

Table 5. Age and trace element data for LA-ICPMS spot analyses on zircon grains for the Pan Tak garnet-two-mica granite, Coyote Mountains, southern Arizona, USA.

	Age (Ma)	± 2s	P	Sc	Ti	Y	Nb	La	Ce	Pr	Nd	Sm	Eu	Gd	Tb	Dy	Ho
Sample **CM-14-04**	**Pan Tak garnet-two-mica granite** (Coyote Mountains, southern Arizona)								Mount **ICGEO-262** (November 2019)								
CM14-**25**	49.3	± 1.9	-750	312	12.5	5200	126.00	0.146	46.5	0.420	4.20	9.40	2.05	69.0	31.40	431	177.0
CM14-**23**	50.3	± 1.3	-2160	406	203.0	11900	290.00	11.100	32.6	5.900	48.00	67.00	6.10	255.0	88.00	1040	380.0
CM14-**14**	50.7	± 0.8	7500	301	15.9	10200	386.00	1.190	57.0	1.900	16.60	27.00	3.36	143.0	65.00	820	338.0
CM14-**31**	53.0	± 1.0	-200	358	8.5	4560	105.00	15.600	14.0	4.600	25.80	25.50	3.80	82.0	30.80	354	125.0
CM14-**12**	54.1	± 1.8	4500	310	13.8	11100	347.00	32.000	44.0	6.700	37.00	31.10	3.34	134.0	59.00	830	347.0
CM14-**35**	54.3	± 0.9	-350	378	11.7	3160	79.00	0.660	10.2	0.680	6.80	9.80	1.03	38.5	16.30	212	88.0
CM14-**34**	55.9	± 2.0	-90	262	11.7	2900	6.10	0.004	43.5	0.073	2.40	5.70	2.34	44.7	18.00	241	99.0
CM14-**3**	56.2	± 1.9	80	141	5.8	4400	47.00	0.260	16.9	0.470	5.40	9.20	1.16	48.0	20.00	290	131.0
CM14-**19**	56.3	± 0.7	-1600	370	9.3	7000	107.00	3.600	105.0	1.870	12.10	20.70	5.20	117.0	46.00	580	231.0
CM14-**22**	**56.5**	**± 1.6**	-80	124	4.8	850	3.90	1.230	14.8	1.160	4.50	5.30	1.29	15.4	6.70	60	24.0
CM14-**29**	**56.8**	**± 1.2**	-180	205	6.2	2140	20.10	0.000	48.0	0.068	1.15	4.20	1.37	33.8	13.40	175	72.0
CM14-**8**	**56.9**	**± 2.2**	-240	163	2.2	1140	2.38	0.000	20.6	0.047	0.88	2.13	0.85	16.3	6.70	82	35.9
CM14-**20**	**56.9**	**± 1.9**	-1600	201	6.8	1920	11.00	0.230	76.0	0.178	2.43	5.75	2.18	39.0	14.40	173	67.0
CM14-**39**	**57.1**	**± 1.3**	-230	260	8.8	2530	12.60	0.000	72.0	0.118	1.92	6.80	2.33	41.8	15.90	214	88.0
CM14-**36**	**57.8**	**± 1.2**	90	114	4.3	510	6.30	0.200	7.6	0.250	1.84	1.40	0.40	5.8	2.19	32	15.2
CM14-**38**	**57.8**	**± 0.8**	-130	254	5.8	4570	58.00	0.009	102.0	0.106	2.85	11.50	4.19	89.0	33.40	417	163.0
CM14-**21**	**57.9**	**± 0.8**	-360	258	4.4	3120	51.20	0.000	45.2	0.058	0.95	4.10	1.14	36.2	17.50	238	104.0
CM14-**33**	**57.9**	**± 1.0**	-40	194	4.4	3250	61.40	0.000	55.5	0.078	1.19	6.50	1.99	51.5	21.50	287	114.0
CM14-**37**	**58.3**	**± 1.7**	-90	330	6.9	2640	18.20	0.003	76.0	0.065	1.83	5.60	1.97	41.5	17.40	221	91.0
CM14-**17**	**58.6**	**± 1.3**	3800	93	1.8	488	4.65	0.000	9.4	0.030	0.00	0.67	0.15	3.8	2.09	31	14.7
CM14-**32**	**58.9**	**± 1.5**	70	111	1.7	256	2.21	0.000	4.6	0.013	0.02	0.13	0.02	1.6	0.84	12	6.2
CM14-**30**	**59.0**	**± 1.3**	-190	150	1.9	340	2.80	0.013	4.8	0.022	0.03	0.13	0.14	3.1	1.41	24	10.9
CM14-**5**	**59.3**	**± 1.0**	50	82	1.3	330	1.71	0.004	4.1	0.014	0.04	0.15	0.12	2.5	1.21	20	9.7
CM14-**28**	**59.3**	**± 0.8**	-250	107	2.5	1710	20.30	0.000	23.9	0.011	0.27	2.63	0.93	22.5	9.30	121	53.3
Average			41	176	4.3	1720	18.45	0.113	37.6	0.148	1.33	3.80	1.27	26.9	10.93	140	57.9
CM14-**15**	61.9	± 1.4	9700	192	2.5	3100	28.00	0.000	73.0	0.042	0.53	3.20	1.31	34.5	16.30	236	103.0
CM14-**6**	62.0	± 1.5	80	58	1.2	270	2.50	0.000	9.7	0.027	0.04	0.29	0.19	2.4	1.02	16	7.4
CM14-**24**	76.7	± 2.4	-170	145	5.6	800	8.00	0.000	41.0	0.051	0.91	2.11	0.48	16.5	6.20	75	27.5
CM14-**2**	78.0	± 2.1	240	89	0.4	1250	1.03	0.041	46.0	0.390	5.90	11.60	5.30	41.0	11.90	130	53.0
CM14-**26**	78.7	± 2.3	-70	215	1.7	1590	11.00	0.000	32.9	0.036	0.63	2.71	0.54	16.3	7.30	110	50.0
CM14-**40**	150	± 2	-110	90	3.5	1590	9.70	0.003	63.6	0.082	2.04	3.29	0.83	25.7	10.10	127	54.5
CM14-**4**	168	± 4	90	86	1.0	780	2.70	0.002	14.1	0.023	0.85	1.55	0.40	11.9	4.50	60	26.0
CM14-**11**	169	± 3	1800	93	6.6	1030	3.66	0.179	42.5	0.122	1.46	3.22	1.08	18.8	7.20	88	29.3
CM14-**13**	1107	± 16	-900	70	4.4	413	6.90	0.000	7.9	0.025	0.03	0.43	0.01	4.9	2.18	32	13.5
CM14-**9**	1474	± 80	-400	189	5.0	2140	2.78	0.004	30.0	0.390	7.00	12.10	3.70	59.0	17.40	198	76.0
n = 34																	

Element concentrations (ppm) are calculated relative to analyses of trace-element glass standard NIST 610.

Er	Yb	Lu	Hf	Pb	Th	U
840	1780	353	16500	52.30	1540	5930
1780	3890	760	22000	152.50	3770	15100
1600	3420	680	13700	147.50	6260	18900
620	1760	382	23000	62.00	1110	7600
1730	4000	840	15300	155.00	5410	22000
469	1730	403	25600	64.80	640	7050
457	890	177	9300	1.90	152	158
690	1270	390	6800	45.00	871	5080
1080	2200	425	11300	54.50	3407	5790
134	470	124	16100	5.70	85	517
335	710	144	9200	7.90	599	794
178	410	86	8400	1.20	98	134
301	553	112	7900	2.90	710	348
416	880	179	10300	4.90	397	434
87	268	66	14000	8.60	57	762
701	1260	231	11800	42.30	3750	4820
533	1240	260	10400	25.50	1291	3129
519	960	179	10200	23.00	793	2627
438	880	183	11600	4.20	385	361
83	244	57	12200	5.80	70	613
43	159	46	12500	4.30	67	463
58	179	48	13600	6.60	74	710
56	181	48	5600	3.90	96	897
270	710	154	9800	24.00	1078	3027
277	607	128	10907	11.39	637	1309
510	1110	217	8700	13.80	786	1807
41	135	32	4400	2.40	141	687
126	279	60	12400	8.50	159	642
180	400	78	3900	2.70	349	338
283	830	185	14600	18.00	214	1109
260	590	120	10300	26.50	792	1002
126	280	58	7600	12.00	238	496
155	356	74	9800	9.80	313	352
70	137	28	12700	35.50	31	155
340	640	126	11300	80.00	146	277